



HAL
open science

Droplet breakup- Analyse de la rupture de gouttes

Ignacio Roa Antunez

► **To cite this version:**

Ignacio Roa Antunez. Droplet breakup- Analyse de la rupture de gouttes. Fluid mechanics [physics.class-ph]. Normandie Université, 2024. English. NNT : 2024NORMR051 . tel-04823357

HAL Id: tel-04823357

<https://theses.hal.science/tel-04823357v1>

Submitted on 6 Dec 2024

HAL is a multi-disciplinary open access archive for the deposit and dissemination of scientific research documents, whether they are published or not. The documents may come from teaching and research institutions in France or abroad, or from public or private research centers.

L'archive ouverte pluridisciplinaire **HAL**, est destinée au dépôt et à la diffusion de documents scientifiques de niveau recherche, publiés ou non, émanant des établissements d'enseignement et de recherche français ou étrangers, des laboratoires publics ou privés.



Normandie Université



THÈSE

Pour obtenir le diplôme de doctorat

Spécialité **MECANIQUE DES FLUIDES, ENERGETIQUE, THERMIQUE, COMBUSTION, ACOUSTIQUE**

Préparée au sein de l'**Université de Rouen Normandie**

Deformation and breakup of droplets in turbulence.

Présentée et soutenue par
IGNACIO ROA ANTUNEZ

Thèse soutenue le 01/10/2024
devant le jury composé de :

M. CHRISTOPHE DUMOUCHEL	Directeur de Recherche - Université de Rouen Normandie (URN)	Directeur de thèse
M. NICOLAS RIMBERT	Professeur des Universités - Université de Lorraine	Président du jury
M. JORGE CESAR BRANDLE DE MOTTA	- Université de Rouen Normandie (URN)	Co-encadrant
M. ANDREAS HAKANSSON	Professeur des Universités - Université de Lund (SUEDE)	Membre du jury
M. STEPHANE PERRARD	Chargé de Recherche - Sorbonne Université	Membre du jury
MME MARIE-CHARLOTTE RENOULT	Maître de Conférences - INSA de Rouen Normandie	Membre du jury
M. GUNTER BRENN	Professeur des Universités - Université Technique de Graz (AUT)	Rapporteur du jury
M. FRÉDÉRIC RISSO	Directeur de Recherche - Inp (Toulouse)	Rapporteur du jury

Thèse dirigée par **CHRISTOPHE DUMOUCHEL** (COMPLEXE DE RECHERCHE INTERPROFESSIONNEL EN AEROTHERMOCHIMIE)



Abstract

The atomization process is influenced by the deformation and breakup of droplets, which in turn affects the final distribution of droplet size. Several authors have related the breakup of droplets due to turbulence to their free oscillations and have shown that even, for low turbulence levels, droplets break due to a resonant mechanism. This phenomenon provides the foundation for the present study.

As a baseline of this work, the theoretical linear shape oscillations of droplets are first examined from both theoretical and numerical perspectives. The first-order oscillatory motion of an initially deformed droplet, considering the dynamic effects of the surrounding fluid, is described.

Subsequently, the oscillations and breakup of a single, initially unperturbed, spherical liquid droplet subjected to a homogeneous and isotropic turbulent medium are investigated. A theoretical framework for droplet oscillations is developed using a spherical harmonic decomposition that tracks the deformation of the surface from its initial state to just before its breakup as an expansion of each mode of deformation. This approach links the small perturbation amplitude deformation of the droplet to the parameters and properties of the turbulent medium, allowing us to observe how turbulence excites the different modes, ultimately leading to breakup. We relate this phenomenon to linear stability theory and analyse how the droplet lifetime is associated with the turbulence statistics for the ensemble of characteristic values.

During droplet deformation, perturbations of different origins favour the growth of liquid structures of various sizes and shapes. Notably, regions exhibiting contraction (bottlenecks) and accumulation (swelling) patterns may indicate potential breakup events. To accurately predict breakup events, it is essential to consider the multiscale nature of these systems. The temporal evolution of the scale distribution is used to identify all the dynamics involved in the deformation process at each scale throughout the droplet's lifetime.

The problem is approached by direct numerical simulation of the two-phase Navier-Stokes equations using the in-house code ARCHER.

By combining these three analyses, the lifetime of the droplet is studied in two parts: First, the oscillatory motion and frequency of the different modes present in the deformation through the spherical harmonic framework to shed light on the resonance mechanism. Second, the temporal evolution of the scale distribution through a multiscale analysis at the end of the droplet lifetime.

Résumé

Le processus d'atomisation est influencé par la déformation et la rupture des gouttes, qui à leur tour affectent la distribution finale de taille de gouttes convient. Plusieurs auteurs ont établi un lien entre la rupture des gouttes liée à la turbulence et les oscillations libres de celles-ci en montrant que, même pour de faibles niveaux de turbulence, les gouttes se brisent en raison d'un mécanisme de résonance. Ce phénomène est à la base de la présente étude.

Comme point de départ de ce travail, les oscillations linéaires théoriques des gouttes sont examinées d'un point de vue théorique et numérique. Le mouvement oscillatoire du premier ordre d'une gouttelette initialement déformée, considérant les effets dynamiques du fluide environnant, est décrit.

Ensuite, les oscillations et la rupture d'une gouttelette liquide sphérique unique, initialement non perturbée, soumise à un milieu turbulent homogène et isotrope, sont étudiées. Un cadre théorique pour les oscillations des gouttes est développé à l'aide d'une décomposition en harmoniques sphériques qui suit la déformation de la surface depuis son état initial jusqu'à sa rupture. Cette approche relie l'amplitude de la déformation de la goutte d'eau par petites perturbations aux paramètres et aux propriétés du milieu turbulent, ce qui nous permet d'observer comment la turbulence excite les différents modes, conduisant finalement à la rupture. Nous relierons ce phénomène à la théorie de la stabilité linéaire et analysons comment la durée de vie des gouttes est associée aux statistiques de turbulence pour l'ensemble des valeurs caractéristiques.

Pendant la déformation des gouttes, des perturbations d'origines diverses favorisent la croissance de structures liquides de tailles et de formes variées. En particulier, les régions présentant de la contraction (goulots d'étranglement) et de l'accumulation (zones de gonflement) peuvent indiquer l'avènement d'une rupture. Pour prédire avec précision les événements de rupture, il est essentiel de prendre en compte la nature multi-échelle de ces systèmes. L'évolution temporelle de la distribution des échelles est utilisée pour identifier toutes les dynamiques impliquées dans le processus de déformation à chaque échelle tout au long de la durée de vie de la gouttelette

Le problème est abordé par le biais de la simulation numérique directe des équations de Navier-Stokes à deux phases à l'aide du code interne ARCHER.

En combinant ces trois analyses, la durée de vie de la gouttelette est étudiée en deux parties : Premièrement, le mouvement oscillatoire et la fréquence des différents modes

présents dans la déformation à travers le cadre harmonique sphérique afin de mettre en lumière le mécanisme de résonance. Deuxièmement, l'évolution temporelle de la distribution d'échelle par une analyse multi-échelle à la fin de la durée de vie de la goutte.

Acknowledgments

First, I would like to thank:

- Günter Brenn, University Professor at Technische Universität Graz, ISW.
- Frédéric Risso, Directeur de recherche CNRS, at IMFT, Toulouse.

for agreeing to be reviewers of the manuscript of the PhD thesis, and:

- Andreas Håkansson, Senior Lecturer at Lund University, PLE.
- Stéphane Perrard, Chargé de recherche CNRS at ESPCI Paris, PMMH.
- Nicolas Rimbert, Professeur des universités at Université de Lorraine, LEMTA.
- Christophe Dumouchel, Directeur de recherche CNRS at CORIA.
- Marie-Charlotte Renoult, Maître de Conférences at INSA Rouen Normandie, CORIA
- Jorge César Brändle de Motta, Maître de Conférences at Université de Rouen Normandie, CORIA

for accepting to be part of the jury of this work.

I would like to express my deepest gratitude to my supervisor, Jorge César Brändle de Motta, for his enthusiasm and seemingly endless willingness to discuss science. For his mentorship and support. I would also like to thank him for his immense help with the personal challenges of doing a PhD in another country. I would like to thank Marie-Charlotte Renoult and Christophe Dumouchel, for accompanying me throughout this project, for your advice and guidance. To all three of you, thank you for trusting me to carry out this thesis. Thanks to you, I have learnt a lot and grown not only as a researcher but also as a person.

I would also like to thank François-Xavier Demoulin, Julien Réveillon, Thibaut Menard and Benjamin Duret for their advice and the discussions during the team meetings. I would also like to thank Fabien Thiesset and Alexandre Poux for their help understanding the ARCHER code and the PyARCHER libraries, and for their aid in the development and use of the numerical tools presented in this PhD.

To the team of doctoral students and post-docs of the laboratory for the many conversations and shared laughs during the coffee break. To all my friends. Thank you for receiving me, helping me, motivating me and making me feel at home. Without you I couldn't have done it.

To Plan d'Evacuation, Argan, Olivier and Emeric, for their warm welcome and the opportunity to make music together.

I would like to thank my parents, Marcos and Alejandra, and my brother Agustín, for giving me strength and unconditional support not only during my studies but throughout my life. For being the ones that believe in me when I don't. To my grandparents Julio, Inés, Rubén y María. Without them, I would not be where I am today.

Finally, I would like to thank Lara for her love and support throughout these three years. Thank you for accompanying me, now and always.

Contents

1	Introduction	9
2	Methodology	13
2.1	ARCHER	13
2.1.1	Levelset	14
2.1.2	Volume of fluid	16
2.2	PyARCHER	17
2.3	Spherical harmonic decomposition	18
2.3.1	Spherical harmonics	18
2.3.2	Decomposition framework	20
2.3.3	Validation of the framework	24
2.4	Inertia tensor calculation	27
2.4.1	Validation of the inertia tensor framework	28
2.5	Minkowski functionals	29
2.5.1	Minkowski functionals computation	30
3	Linear oscillations of drops and bubbles	32
3.1	Introduction	32
3.2	Linear theory	34
3.2.1	Formulation	34
3.2.2	Governing equations	35
3.2.3	Solution of the dispersion relation	37
3.3	Numerical approach	42
3.4	Cross-validation	45
3.4.1	Shape oscillations	45
3.4.2	Energetic approach	48
3.5	Beyond linear theory	52
3.5.1	Coupling between modes	52
3.5.2	High amplitude deformations	55
3.6	Conclusion	57

4	Droplets in turbulence	60
4.1	Introduction	60
4.2	Droplet database	61
4.2.1	Generation of the database	61
4.2.2	Physical and numerical parameters	63
4.2.3	Decomposition of droplets immersed in a turbulent background flow	65
4.3	Oscillations of droplets immersed in a turbulent flow	67
4.3.1	Initial-growth and saturation regime	70
4.4	Large deformations and damping factor	72
4.5	Conclusion	79
5	Multiscale analysis	81
5.1	Introduction	81
5.2	The multiscale description	82
5.3	Multiscale analysis of drops in turbulence	85
5.4	Breakup dynamics	89
5.5	Conclusion	93
6	Conclusions and perspectives	96
A	Synthèse générale	102
	Bibliography	115

Chapter 1

Introduction

Atomization transforms bulk liquid into small droplets, forming a spray that enhances rapid evaporation and extensive surface coverage. This process is crucial in various industries, including fuel injection, sprinkler irrigation, spray drying, and fire suppression. Each application requires specific spray characteristics, particularly droplet size control, which is vital for efficiency and effectiveness (Lefebvre & McDonell 2017). For example, in fuel injection, large droplets can impede complete evaporation, reducing combustion efficiency.

Atomization occurs in two stages: primary and secondary atomization. In the primary stage, bulk liquid, typically in a jet or sheet form, breaks into larger structures near the injector due to instabilities such as Kelvin-Helmholtz and Rayleigh-Taylor. In the secondary stage, these larger structures disintegrate into smaller droplets until surface tension effects dominate, achieving the final droplet size distribution. Turbulence significantly impacts secondary atomization, especially in applications like combustion chamber injection, where high turbulence levels in the carrier fluid cause droplets to deform and fragment (Wählin 2007, Sanjosé et al. 2011).

Atomization is inherently multi-scaled. In some applications, final droplets can be as small as a few micrometres, while the total domain can extend to several centimetres. Studying the entire process is challenging, particularly the direct numerical simulation (DNS) of both primary and secondary breakup. Therefore, two strategies are commonly employed: primary atomization simulation and spray simulation (Fiorina et al. 2016).

Turbulent droplet breakup in liquid-liquid dispersed flows is also common in chemical and biochemical industries. This process involves mixing two immiscible liquids in either stirred batch or continuous reactors, typically with one aqueous and one organic phase, as seen in extraction processes using mixer-settlers (Davies 1992). Understanding and controlling these stages is crucial for optimizing atomization across various applications. This study focuses on the physics behind secondary atomization under turbulent conditions to improve predictions of spray characteristics.

Droplet deformation and breakup significantly influence the final droplet size distri-

bution, with turbulence playing a key role in secondary breakup. Several authors have suggested that turbulent breakup of droplets can be attributed to a resonant mechanism achieved through their free oscillations, even at low turbulence levels (Sevik & Park 1973, Risso & Fabre 1998, Lalanne et al. 2019). This phenomenon motivates the present study.

As a baseline, a linear stability analysis of Newtonian droplets in a Newtonian surrounding fluid is conducted. The theoretical linear oscillations of droplets are examined from both theoretical and numerical perspectives, describing the first-order oscillatory motion of an initially deformed droplet considering the dynamic effects of the surrounding fluid. Three limiting cases are considered: a droplet in a vacuum, a liquid-liquid configuration, and a bubble in a liquid.

Subsequently, the oscillations and breakup of a single, initially unperturbed spherical liquid droplet in a homogeneous and isotropic turbulent medium are investigated. A theoretical framework for droplet oscillations is developed for each mode of deformation using a spherical harmonic decomposition that tracks surface deformation from its initial state to just before breakup. This approach links small perturbation amplitude deformation of the droplet to the turbulent medium's parameters, showing how turbulence excites different modes, ultimately leading to breakup. This phenomenon is related to linear stability theory.

During droplet deformation, perturbations of different origins favour the growth of liquid structures of varying sizes and shapes. Regions exhibiting contraction (bottlenecks) and accumulation (swelling) patterns may indicate potential breakup events. To predict these events accurately, it is essential to consider the multiscale nature of these systems. The temporal evolution of the scale distribution is used to identify all the dynamics involved in the deformation process at each scale by the end of the droplet's lifetime.

Experimental studies on droplet evolution, particularly under turbulent conditions, have faced challenges such as obtaining local carrier fluid states and shape evolution simultaneously, reproducing well-controlled isotropic turbulent conditions, and achieving reliable statistics on breakup frequency. Additionally, these studies often rely on 2D projections of the 3D droplet shape, lacking detailed descriptions of local shape deformation at all scales.

These limitations are overcome through direct numerical simulations (DNS) of isolated droplets under turbulent conditions using the in-house code ARCHER (Ménard et al. 2007). ARCHER is chosen for its capabilities to reproduce Lamb theory oscillations (Aniszewski et al. 2014, Cordesse et al. 2020) and the Levelset implicit description that allows accurate computation of the spherical harmonic coefficients (Roa et al. 2023a). By generating turbulent conditions using a linear forcing scheme (Duret et al. 2012) and creating realistic initial conditions for droplets, the project ensures accurate simulations. This methodology enables a detailed parametric study of droplet breakup, providing valuable insights into the physics of secondary breakup and leading to the development of more accurate predictive models for industrial applications.

By combining these two analyses, the droplet's lifetime is studied in two parts: first,

the oscillatory motion and frequency of different modes in the deformation through the spherical harmonic framework, relating the turbulence-driven deformation to the oscillations present in the linear theory; and second, the temporal evolution of the scale distribution through a multiscale analysis at the end of the droplet’s lifetime.

The study combines theoretical and numerical analyses of droplet deformation and breakup. Using a spherical harmonic decomposition framework, droplet deformation in a turbulent medium is tracked, connecting drop oscillations in turbulence to linear theory. A multiscale analysis aids in predicting breakup events by considering multiscale systems, combining oscillatory motion analysis and multiscale evolution to understand droplet breakup.

The work presented analyses droplet deformation and breakup in turbulence across three principal stages of the droplet’s lifetime: an initial phase of deformation due to turbulent flow, oscillatory motions induced by interaction with turbulent eddies, and the final breakup stage. These stages are represented in figure 1.1.

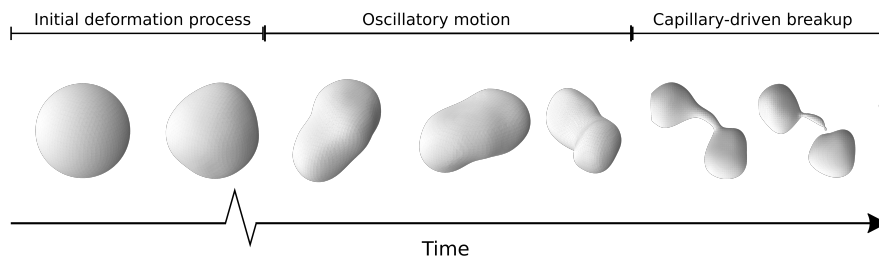


Figure 1.1: A sequence of snapshots of a breaking droplet following the oscillation process, the inertial deformation process and the capillary-driven breakup across the droplet lifetime. Figure inspired by Qi et al. (2024).

The main objective of this PhD thesis is to characterize the deformation and breakup of droplets from their initial state until rupture. The subsequent chapters of this PhD thesis are divided as follows:

Chapter 2 introduces the numerical methods and tools used throughout the manuscript. It begins with a brief overview of the in-house code ARCHER, which was used for all DNS presented in the manuscript.

This chapter includes the development and validation of post-treatment algorithms for tracking droplet interface deformation, and a brief description of the already implemented routines in the post-treatment code PyARCHER.

Chapter 3 presents the linear stability analysis for a Newtonian drop surrounded by a Newtonian fluid. The goal is to develop and numerically validate the linear theory for drop-shape oscillations considering varying viscosities and densities. An energetic approach is also explored, leveraging DNS capabilities. The chapter examines drop-shape oscillations beyond linear theory by studying mode coupling for different Ohnesorge num-

bers and viscosity and density ratios. Three limiting cases are investigated: drop, buoyant drop, and bubble. This analysis provides a foundation for studying droplet oscillations in turbulence, as explored in chapter 4.

In this chapter, the deformation of droplets from a numerical database generated using ARCHER (Roa et al. 2023b, Deberne et al. 2024) is analysed through a spherical harmonic decomposition framework. The analysis of drop-shape oscillations is constrained by the mathematical limits of spherical harmonic expansion, which prevents exploration of droplet morphology just before breakup. Consequently, a new approach is introduced in chapter 5.

The multiscale analysis considers the liquid system and parallel systems obtained through successive erosion operations at various scales until the initial system is fully eroded. This method enables observation of simple situations within complex shapes and characterizes droplet morphology as a cumulative scale distribution. Three principal scales are tracked throughout the droplet’s lifetime, providing insights into drop shape.

Finally, chapter 6 discusses the general conclusions and prospects of this work.

Chapter 2

Methodology

The aim of this thesis is to study the deformation, oscillation, and rupture of bubbles and droplets using Direct Numerical Simulation (DNS). This involves the complex numerical resolution of the Navier-Stokes equations, particularly for two-phase flows, which necessitates accurate boundary conditions at the interfaces between different fluids to ensure the continuity of the calculated fields. The challenge lies in accurately locating these deformable immersed interfaces.

This chapter begins by briefly introducing the principles of various methods for simulating two-phase flow and details the physical equations that need to be solved numerically. A concise description of the DNS code ARCHER is provided, highlighting its capability to solve the Navier-Stokes equations. Key concepts for tracking the interface are presented, which are crucial for the development of the post-processing tools used in this research. These tools and frameworks are essential for characterizing droplet oscillations.

Validation examples for both the developed numerical tools and post-processing methods are also presented.

2.1 ARCHER

The in-house High-Performance-Computing code ARCHER is used to perform all DNS presented in this work. The ARCHER code was one of the first to undertake the simulation of liquid-jet atomization under a realistic diesel injection configuration (Ménard et al. 2007). It solves on a staggered Cartesian mesh the one-fluid formulation of the incompressible Navier-Stokes equations

$$\nabla \cdot \mathbf{V}_i = 0, \quad (2.1)$$

$$\rho_i \left(\frac{\partial \mathbf{V}_i}{\partial t} + \mathbf{V}_i \cdot \nabla \mathbf{V}_i \right) = -\nabla p_i + \nabla \cdot \boldsymbol{\tau}_i + \mathbf{f} + \sigma \kappa \delta_s \mathbf{n}, \quad (2.2)$$

where \mathbf{V}_i is the velocity, p_i the pressure field, ρ_i is the density, μ_i the dynamic viscosity, $\tau_i = \mu_i(\nabla\mathbf{V}_i + \nabla\mathbf{V}_i^T)$ the viscous stress tensor, \mathbf{f} a source term, σ the surface tension, \mathbf{n} the unit normal vector to the interface, κ its mean curvature and δ_s is the Dirac function characterizing the location of the interface. The subscript i is 1 for the dispersed phase and 2 for the continuous phase.

For solving the Navier-Stokes equation, the convective term, $\rho_i(\mathbf{V}_i \cdot \nabla\mathbf{V}_i)$, is written in the conservative form and solved using the improved Rudman's technique (Rudman 1998) presented in Vaudor et al. (2017). The latter allows mass and momentum to be transported consistently, thereby enabling flows with large liquid/gas density ratios to be simulated accurately. The viscosity term is computed following the method presented by Sussman et al. (2007). To ensure the incompressibility of the velocity field, a Poisson equation is solved. The latter accounts for the surface tension force and is solved using a Multi Grid preconditioned Conjugate Gradient algorithm (MGCG) (Zhang 1996) coupled with a Continuous Surface Force (CSF) method (Brackbill et al. 1992).

For transporting the interface, a coupled Levelset and volume-of-fluid (CLSVOF) method is used, in which the Levelset function accurately describes the geometric features of the interface (its normal and curvature) and the volume-of-fluid function ensures mass conservation. The density is calculated from the volume-of-fluid, C , as $\rho = \rho_1 C + \rho_2(1 - C)$ and the dynamic viscosity (μ_1 or μ_2) depends on the sign of the Levelset function. In cells containing both a liquid and gas phase, a specific treatment is performed to evaluate the dynamic viscosity, following the procedure of Sussman et al. (2007). The code has been validated and tested in a variety of atomization conditions, such as high-density ratios and varying Weber and Reynolds numbers (Ménard et al. 2007, Vaudor et al. 2017). The case of an oscillating droplet has been previously validated for the ARCHER code (Aniszewski et al. 2014), finding good agreement with linear theory.

The ARCHER code is continuously under development within the research group, implementing new numerical methods as the need arises. Hence, for a part of the work presented in this manuscript a newer version of the ARCHER code is used. In particular, for the linear oscillations presented in chapter 3.

The work done during this PhD did not involve further developing the ARCHER code. However, post-processing tools were developed to analyse the numerical simulations performed, that employ the properties of the direct numerical simulation solver. For the sake of clarity, these numerical concepts regarding the architecture of the ARCHER code are introduced.

2.1.1 Levelset

The Levelset method was first devised by Osher & Sethian (1988) as numerical method used to describe and track the motion of interfaces or boundaries in two or three dimensions. The idea behind the Levelset method is to define a smooth function $\phi(\mathbf{x}, t)$, where the interface is represented as the set where $\phi(\mathbf{x}, t) = 0$. The Levelset function ϕ is then

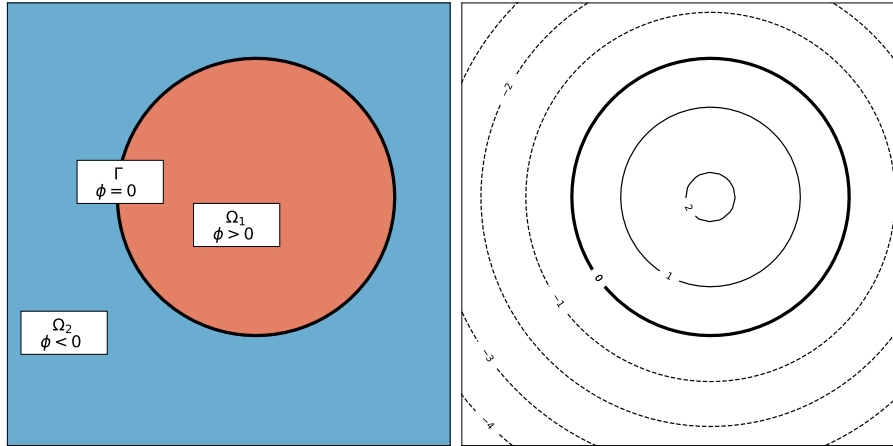


Figure 2.1: Levelset method. On the left, the interface representation. On the right, Levelset contours for a circular interface of radius 2.5 units.

considered as a signed distance equation, which represents the shortest distance from the interface to each point within the domain

$$\begin{cases} \phi(\mathbf{x}, t) > 0 & \text{for } \mathbf{x} \in \Omega_1 \\ \phi(\mathbf{x}, t) = 0 & \text{for } \mathbf{x} \in \Gamma \\ \phi(\mathbf{x}, t) < 0 & \text{for } \mathbf{x} \in \Omega_2 \end{cases} \quad (2.3)$$

where Ω_i is the region within the bound or outside it, with the subscript $i = 1, 2$ for inner or outer fluid respectively and Σ is the interface, and $\mathbf{x} = (x_1, x_2, \dots, x_n) \in R^n$. This is illustrated in figure 2.1.

Thus, to capture the interface at any future time, one simply needs to locate the set $\Gamma(t)$ where ϕ is zero. This gives way to one of the strengths of the Levelset method, which is its ability to handle complex changes in topology, such as coalescence or separation of interfaces, without requiring special treatment. This is possible because the method implicitly represents the interface and can naturally deal with changes in shape.

The motion is analysed by convecting the ϕ values (levels) with the velocity field \mathbf{V}

$$\frac{\partial \phi}{\partial t} + \mathbf{V} \cdot \nabla \phi = 0. \quad (2.4)$$

Nonetheless, the transport of the interface induces loses in the Levelset function signed-distance property $|\nabla \phi| = 1$. To solve this problem, the work of Sussman et al. (1994) proposed a redistanciation step based on the resolution of the partial differential equation (PDE)

$$\frac{\partial D}{\partial \tau} = \text{sign}(\phi) - (1 - |\nabla D|) \quad (2.5)$$

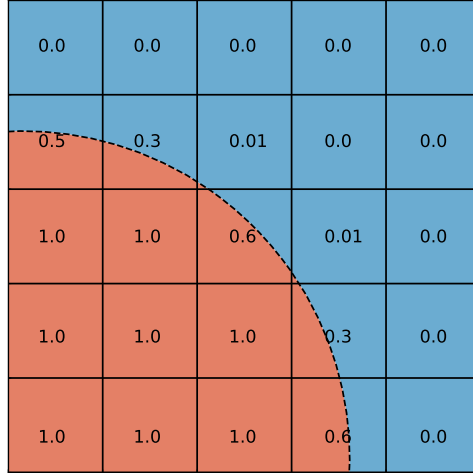


Figure 2.2: Sketch of the VoF scalar field C .

at each time step. This algorithm updates the Levelset from the interface iteratively over a fictitious time, τ , to conserve the distance property.

The application of the Levelset method in the ARCHER code for this work allows for the tracking of the interface deformation throughout the droplet lifetime and is an integral part for the development of the post-processing tool described in section 2.3 and for the computation of the method described in section 2.5.

2.1.2 Volume of fluid

Volume of fluid methods (VoF) are numerical techniques used to track and locate the free surface (interface) between two or more immiscible fluids within a computational domain. These methods are particularly useful for simulating multiphase flows, where distinct fluid phases coexist.

The Volume of Fluid method, as described in the work of Noh & Woodward (1976), uses the phase volume reconstruction in each cell. It is based on the liquid/gas ratio in a cell and the direction of transport. The VOF method uses a function $C(\mathbf{x}, t)$ to represent the volume fraction of one of the fluids in each computational cell. $C(\mathbf{x}, t) = 1$ indicates the cell is entirely filled with the fluid, $C(\mathbf{x}, t) = 0$ indicates it is entirely filled with the other fluid, and $1 < C(\mathbf{x}, t) < 1$ indicates the presence of the interface. The volume of fluid method, and the values of $C(\mathbf{x}, t)$, are represented in figure 2.2.

One of the advantages of the VOF method is its capacity to conserve the quantity of volume in the domain. Although the initial approach to calculating the interface characteristics (normal and curvature) was more accurate when using a Levelset method, recent developments in the VoF method have led to improvements in this calculation (Bornia et al. 2011). The application of the VoF method in the ARCHER code for this work al-

lows for the tracking of the volume distribution of the droplet throughout its lifetime and is an integral part for the development of the post-processing tools described in section 2.3 and 2.4.

2.2 PyARCHER

Results from ARCHER simulations are saved in HDF5 format, with one time series per processor and multiple time steps per file. For visualization, such as using ParaView, ARCHER also writes XMF files. These files provide information about the simulation domain's geometry (e.g., origin, grid spacing) and topology (connectivity between MPI blocks).

PyARCHER is the in-house Python platform for pre- and post-processing ARCHER data. Although designed for ARCHER data, PyARCHER's applications can be used with any staggered CFD code following the MAC discretization.

This code reads simulation data using the Dask library (Dask Development Team 2016), storing them in an 'xarray.Dataset'. All time steps and processors are merged into a 4D array with coordinates "x", "y", "z", and "t". These coordinates can be specified by the user or read from the XMF files. The minimal data blocks (one processor and one time step) are called chunks and serve as the unit of work for Dask.

Data written by ARCHER include ghost cells for boundary conditions and processor interfaces. The latter are removed during the merging operation, while the former can be removed if necessary.

PyARCHER is an open-source post-treatment tool continuously under development. It supports a "lazy" approach to post-processing, where necessary routines are prepared and introduced to the code beforehand. These routines can be utilized once the simulation is complete, allowing data to be processed multiple times without affecting DNS calculation time. Each implemented library includes automatic self-validation. Whenever any part of the code is changed, PyARCHER verifies that the subroutines still function as intended every time it is compiled.

In the following sections three different post-treatment algorithms are presented: the spherical harmonic decomposition, inertia tensor computation, and the Minkowski functionals computation. The two former were developed as a part of this PhD work to characterize droplet deformation and oscillations, implemented into PyARCHER. The latter was developed as a part of a previous study (Dumouchel et al. 2022) and has been used for the analysis presented in chapter 5.

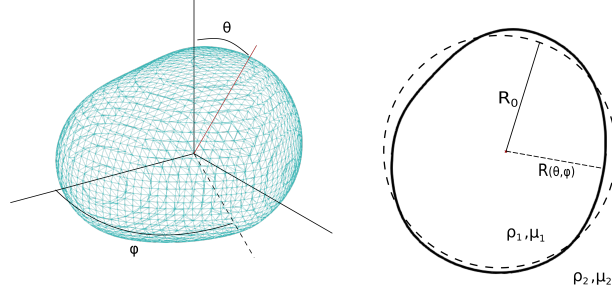


Figure 2.3: Drop deformation: sketch and definitions.

2.3 Spherical harmonic decomposition

2.3.1 Spherical harmonics

In mathematics and physics, spherical harmonics are special functions defined on the surface of a sphere, often used in solving partial differential equations. Since they form a complete set of orthogonal functions, any shape that is star shaped (radially convex set) that can be described in a spherical coordinate reference (see figure 2.3) can be written as a sum of spherical harmonic functions. The spherical harmonic functions provide a robust mathematical basis for representing complex shapes and variations in the radial, polar, and azimuthal directions.

To study the shape evolution of a drop immersed in a turbulent flow we introduce the spherical harmonic functions $Y_m^l(\theta, \varphi)$, following the works by Risso (2000), Lalanne (2012) and Perrard et al. (2021).

The distance from the centre of the reference frame to the droplet interface can be described by

$$R(\theta, \varphi) = R_0 \sum_{m=0}^{\infty} \sum_{l=-m}^m a_{m,l} Y_m^l(\theta, \varphi). \quad (2.6)$$

where $a_{m,l}(t)$ corresponds to the amplitude of the deformation expressed as a spherical harmonic coefficient, R_0 is the equivalent radius and Y_m^l is the spherical harmonic function. Finally, m and l correspond to the spherical harmonic degree and order respectively, with $m \geq 0$ and $-m \leq l \leq m$. The degree (often referred to in the literature as modes) m determines the number of lobes in the polar coordinate, while the order l specifies the orientation of these lobes in the reference frame system, with $l = 0$ corresponding to the axisymmetric configuration. A representation of the spherical harmonic functions can be seen in figure 2.4. The reference frame axes x, y, z are represented by the red, yellow and green lines respectively, considering z the axisymmetry axis. The spherical harmonic function is defined as

$$H_m^l(\theta, \varphi) = \sqrt{(2m+1) \frac{(m-l)!}{(m+l)!}} P_m^l(\cos \theta) e^{il\varphi}, \quad (2.7)$$

with $P_m^l(\cos \theta)$ corresponding to the associated Legendre functions, $m \in \mathbb{N}$ and $l \in [-m, m]$. Since H_m^l are complex functions of angle, it is often considered more convenient to use their real forms for their depiction in figures and in some calculations. A suitable real basis of spherical harmonics may be defined as:

$$Y_m^l(\theta, \varphi) = \begin{cases} \frac{i}{\sqrt{2}}(H_m^l - (-1)^m H_m^{-l}) & \text{if } m < 0 \\ H_m^0 & \text{if } m = 0 \\ \frac{i}{\sqrt{2}}(H_m^{-l} + (-1)^m H_m^l) & \text{if } m > 0. \end{cases} \quad (2.8)$$

To calculate the spherical harmonic expansion of a function $R(\theta, \varphi)$ defined on the surface of a sphere, certain conditions and properties of the function and the spherical harmonics must be met. These conditions ensure that the function can be appropriately represented and that the expansion converges.

The function $R(\theta, \varphi)$ must be square-integrable over the sphere. Meaning that

$$\int_{\Omega} |R(\theta, \varphi)|^2 d\Omega < \infty, \quad (2.9)$$

where $d\Omega$ corresponds to the differential surface area on the unit sphere $\sin \theta d\theta d\phi$. Square-integrability ensures that the function $R(\theta, \varphi)$ has finite energy over the sphere and can be expanded in terms of spherical harmonics.

A second condition is that the spherical harmonic functions must form an orthogonal basis for the function space. This orthogonality is given by

$$\int_{\Omega} Y_m^l(\theta, \varphi) Y_m^{l*}(\theta, \varphi) d\Omega = \delta_{mm} \delta_{ll}, \quad (2.10)$$

where δ is the Kronecker delta. This orthogonality property is essential for computing the coefficients $a_{m,l}$. The representation of the spherical harmonic function as a double series is a generalized Fourier series. Therefore, if normalized, it represents a complete orthonormal system of functions for all degrees m and orders l . Due to this property, the spherical harmonic coefficients of a function can be computed with the integral

$$a_{m,l} = \int_{\Omega} R(\theta, \varphi) Y_m^l(\theta, \varphi) d\Omega, \quad (2.11)$$

The objective is to relate the spherical harmonic expansion with the surface deformation. It is important to note that the total energy stored at the interface is directly proportional to the total surface area, represented by η_{Ω}^2 . Parseval's theorem, alternatively

known as Rayleigh’s energy theorem, provides a valuable tool for this purpose, as it establishes a relationship between the integral of the square of a function and the sum of the square of its transform. Due to the orthogonality properties of the spherical harmonic functions, this can be written as

$$\frac{1}{4\pi} \int_{\Omega} R^2(\theta, \phi) d\Omega = \eta_{\Omega}^2, \quad (2.12)$$

where

$$\eta_{\Omega}^2 = \sum_{m=0}^{\infty} \sum_{l=-m}^m a_{m,l}^2. \quad (2.13)$$

By leveraging Parseval’s theorem, we can quantify the energy stored in the surface deformation and relate it to the coefficients of the spherical harmonic expansion, thereby elucidating the contribution of different harmonic modes to the overall deformation energy (Perrard et al. 2021). The power spectrum a_m^2 is computed by

$$a_m^2 = \sum_{l=-m}^m a_{m,l}^2. \quad (2.14)$$

This expression sums the squares of all coefficients $a_{m,l}$ associated with the same degree m . Since the coefficients $a_{m,l}$ of same degree m are associated to the same oscillatory frequency, the power spectrum provides the energy contained in each mode and relate it to its contribution to the total deformation of the system. Importantly, the power spectrum is inherently positive by definition and remains independent of the orientation of the reference frame.

2.3.2 Decomposition framework

In order to describe the shape of a droplet as a series of spherical harmonic functions, the first step is to obtain the distribution of its radius as a function of the polar angles as $R(\theta, \varphi)$. The values of $R(\theta, \varphi)$ are obtained through a loop that computes the values of the radius across the interface (figure 2.5a) following the spherical coordinates reference frame over an array of angles, whose size is given by the maximum number of modes, M , we wish to evaluate. More specifically, the array (as shown in figure 2.5b) will be of shape $2(M + 1) \times 2(M + 1)$. The algorithm for obtaining the distribution of distances to the interface is the following:

1. **Center fields:** The ARCHER code allows two-phase DNS in periodic boundary conditions. This can cause instances in which the simulated liquid-phase passes through one side of the domain and re-appearing on the opposite side. To correct this, the first step is to ensure that the body is contained within the domain. The

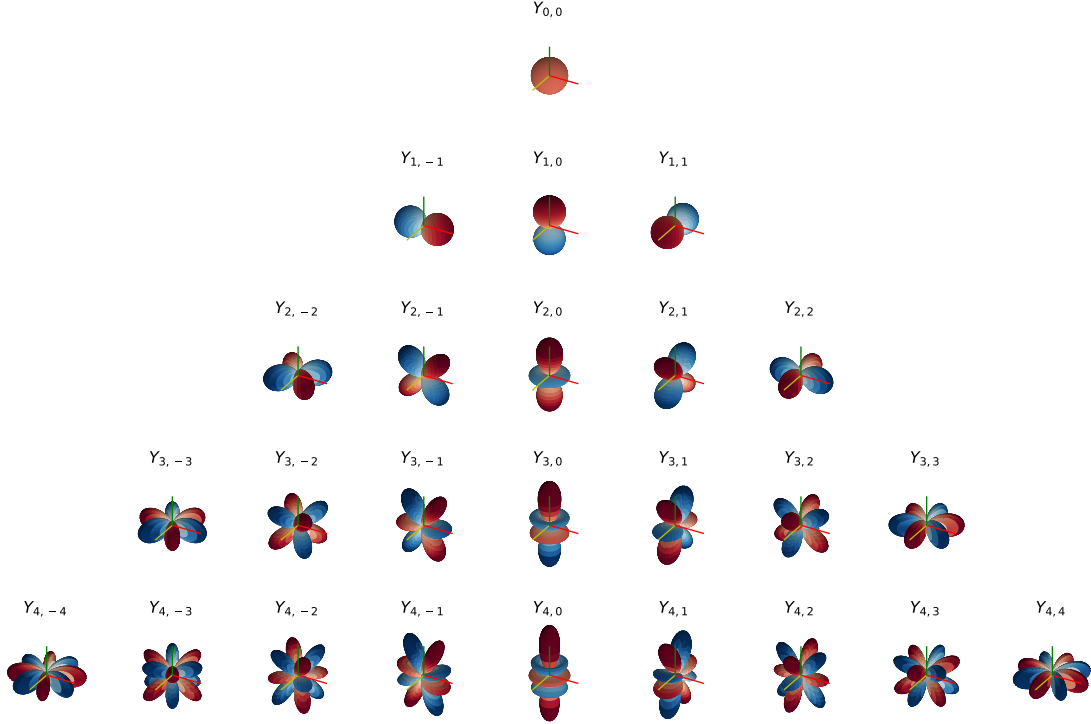


Figure 2.4: Representation of the spherical harmonic function Y_m^l for degrees until $m = 4$ with the corresponding degrees. The red and blue colours represent the positive and negative values respectively.

VoF and Levelset fields are repositioned to be, in a continuous form, within the bounds by moving these fields until none of the walls are being touched. If this is not possible due to the extended geometry of the body, the domain is expanded to ensure this condition.

2. **Obtain the centre:** To describe the surface of a body as an ensemble of spherical harmonic functions the computation of the origin of the reference frame is of utmost importance, since it will define the distance to the interface its position will greatly vary spherical harmonic amplitudes. To compute the values of $R(\theta, \varphi)$ distributed across the grid three methods were implemented: *cartesian centre*, *mass centre* and *surface centre*. These three methods are revised later in this section.
3. **Radius computation:** Once the centre of the body is obtained, the last step is to compute the distance from the centre to the interface following the spherical coordinates reference frame over an array of angles $R(\theta, \varphi)$. As discussed in section 2.1.1, to capture the interface at any time, one simply needs to locate where $\phi(\mathbf{x}, t) = 0$. Due to this, it is possible to capture the distance between the centre and the inter-

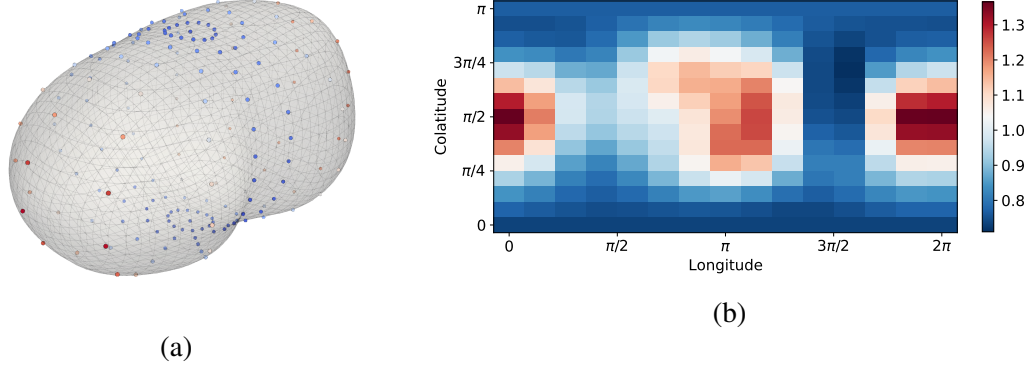


Figure 2.5: Illustration of the interface mapping of a droplet deformed by a turbulent background flow for a spherical harmonic decomposition with $M = 6$ using the centre of mass. (a) The points are distributed around a revolution axis given by the reference frame. (b) The normalized distances between the centre and the interface are stored in a grid. The colorbar corresponds in both figures to the values of the function $R(\theta, \varphi)$ normalized by the reference radius R_0 .

face for any set of angles (θ, φ) by tracing a line to a point outside of the droplet and finding the intersection to the drop’s interface. This subroutine has two different interpolation methods built-in: linear and cubic.

The coefficients are then computed from this array with the help of the library SHTOOLS (Wieczorek & Meschede 2018). A Fast Fourier Transform (FFT) is applied to the input data with respect to the longitude. This step transforms the data into the frequency domain for the longitudinal component. For each degree m and order l , the algorithm integrates the product of the input data $R(\theta, \varphi)$, the associated Legendre polynomial P_m , and the exponential term $e^{il\varphi}$ over the sphere, where φ is the longitude (refer to eq. 2.7) and θ the colatitude. The spherical harmonic coefficients $a_{m,l}$ are then obtained by solving the integral shown in equation 2.11. Furthermore, by obtaining the coefficients $a_{m,l}$, the body can be reconstructed with the desired number of spherical harmonics functions. As an example, the morphology of a droplet deformed by a turbulent background flow is reconstructed using the first 6 modes of deformation in figure 2.6.

Cartesian centre

The Cartesian mean centre method is a straightforward approach to determine the average position of a set of points in Cartesian coordinates. It is often used to find the centroid (or geometric centre) of a collection of points in two or three-dimensional space.

The Cartesian mean centre (or centroid) of a set of N points with coordinates in 3D space is defined as $\mathbf{c} = (\bar{x}, \bar{y}, \bar{z})$, where

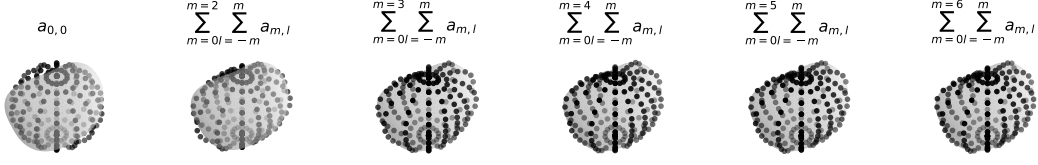


Figure 2.6: Reconstruction of a deformed droplet using the spherical harmonic modes $m = [2 - 6]$ obtained through its decomposition.

$$\bar{x} = \frac{1}{N} \sum_{i=0}^N x_i, \quad \bar{y} = \frac{1}{N} \sum_{i=0}^N y_i, \quad \bar{z} = \frac{1}{N} \sum_{i=0}^N z_i. \quad (2.15)$$

The coordinates (x_i, y_i, z_i) of the interface, are obtained from the Levelset field presented in section 2.1.1. The Cartesian mean centre is equidistant from all points in the sense that it minimizes the sum of squared distances to the points and involves straightforward arithmetic operations, making it computationally efficient.

Mass centre

The centre of mass of a body is a point that represents the average position of the mass distribution of the body. It is the point where the entire mass of the body can be considered to be concentrated.

For a continuous 3D body with a density ρ , the mass centre (or centroid) can be defined as the point $\mathbf{c} = (x_{mc}, y_{mc}, z_{mc})$ where

$$x_{mc} = \int_V x \rho_1 dV, \quad y_{mc} = \int_V y \rho_1 dV, \quad z_{mc} = \int_V z \rho_1 dV. \quad (2.16)$$

As presented earlier, the VoF field provides the information of the quantity of volume per mesh cell. Using this field allows for a rapid computation of the centre of mass simply as

$$x_{mc} = \frac{1}{\Pi} \sum_{i=0}^N m_i x_i, \quad y_{mc} = \frac{1}{\Pi} \sum_{i=0}^N m_i y_i, \quad z_{mc} = \frac{1}{\Pi} \sum_{i=0}^N m_i z_i, \quad (2.17)$$

where $\Pi = \sum_{i=0}^N m s_i$ is the total mass, which at the same time $m s_i = V_i \rho$ is the mass of each cell element.

Given that the VoF field is cell centred (located at the centre of the mesh cell), the computation of the centre of mass using this field is not entirely accurate. A more correct

approach would be to use the PLIC-VoF method (piecewise linear interface construction), which would provide a more accurate position of the volume concentration of the droplet in each cell. Nonetheless, for the purposes of this study, the approximation is sufficient.

Surface centre

The surfacic centre is not as commonly used or well-defined as the centroid or centre of mass, but it can generally be understood to mean a point that represents the average position of the surface of a geometric object. The surface centre can be considered analogous to the centroid but specifically for the surface rather than the volume.

For a 3D body of surface S with continuous coordinates (x, y, z) , the surface centre can be defined as $\mathbf{c} = (\bar{x}_S, \bar{y}_S, \bar{z}_S)$, where

$$\bar{x}_S = \frac{1}{A} \int_S x dA, \quad \bar{y}_S = \frac{1}{A} \int_S y dA, \quad \bar{z}_S = \frac{1}{A} \int_S z dA, \quad (2.18)$$

where A is the total surface area of the surface S and dA is a differential element of surface area. For the centre of surface, the Levelset field is used to triangulate the surface of the body. The individual areas A_i of the triangles along with their vertices are obtained by discretizing the zero Levelset surface with a triangulated mesh using a Marching Cube algorithm. The *surface operators*' library of PyARCHER is used for this end.

Finally, the centre of mass can be approximated as

$$\bar{x}_S = \frac{1}{A} \sum_{i=0}^N x_i A_i, \quad \bar{y}_S = \frac{1}{A} \sum_{i=0}^N y_i A_i, \quad \bar{z}_S = \frac{1}{A} \sum_{i=0}^N z_i A_i. \quad (2.19)$$

2.3.3 Validation of the framework

Sphere

The spherical harmonic decomposition corresponds to an expansion of the function that describes the surface over a sphere. To test and validate this framework, an initial validation test is conducted on a spherical droplet generated using ARCHER. In this context, for the first validation test involving a perfect sphere, the result of the expansion should closely resemble the surface of a unit sphere. This implies that:

$$\int_{\Omega} R(\theta, \varphi) Y_m^l(\theta, \varphi) d\Omega = 1 \quad (2.20)$$

To demonstrate the accuracy of spherical harmonic decomposition, we follow a systematic approach using a Levelset function field to represent a sphere. We begin by defining a sphere with a radius $R_s = 1$ within a numerical domain discretized into a grid containing $N_x \times N_y \times N_z = N^3$ points. The grid spacing is determined by

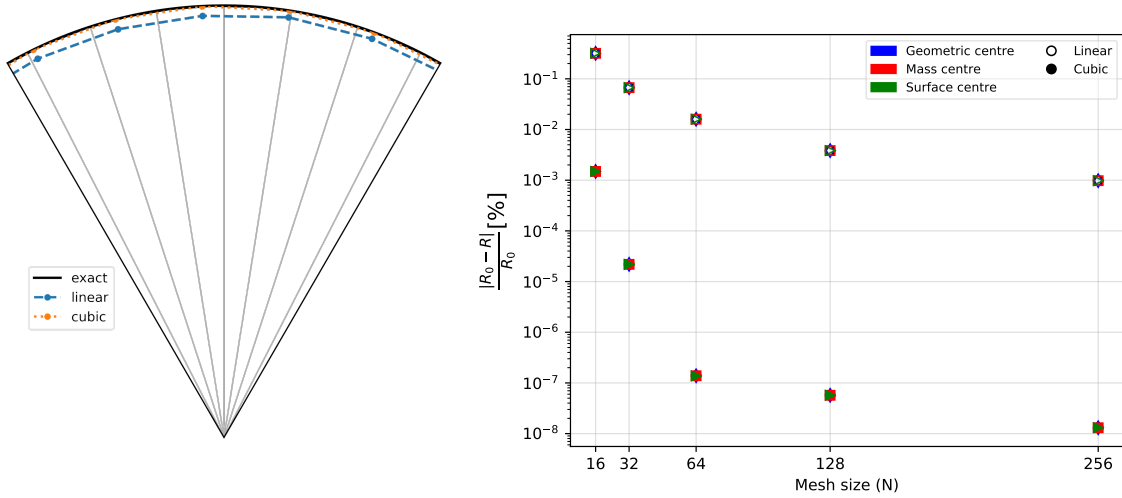


Figure 2.7: Interface reconstruction using linear and cubic interpolation methods is compared in the following analysis. Additionally, the error in radius calculation using each method is depicted on the right for comparison.

$\Delta x = \Delta y = \Delta z = \frac{3 \times R_s}{N}$, ensuring that the grid can accurately capture the geometry of the sphere. The sphere is placed at the centre of this numerical domain to facilitate symmetrical analysis and computation. For this particular validation case the reference centre is computed using the three different methods mentioned previously. The values of $R(\theta, \varphi)$ are obtained from across the interface (figure 2.5a) following the spherical coordinates reference frame over the array of angles given by the longitude and colatitude. In order to test the accuracy of the computation of the radius, both implemented interpolation methods are also tested. In figure 2.7 (left), the accuracy of the implemented interpolation methods in the computation of the droplet radius using the exact centre of the droplet is shown. At first glance its easy to realize that the higher the order of interpolation, the better the reconstruction of the droplets interface. This is also supported by figure 2.7 (right). It is found that the computation of the droplet radius with a cubic interpolation method has a relative error lower to 0.001% already for a coarse grid of 16^3 cells. Whilst the use of a linear interpolation for the computation of the distance from the centre to the interface of the droplet has a comparatively high relative error, for domains of 32^3 cells the relative error is already below 0.1%. This, combined with its high speed computation time makes it a great tool for tracking the evolution of the spherical harmonic coefficients for drops with long lifetimes.

Odd modes

We must also consider that for a proper computation of the spherical harmonic expansion it is of utmost importance to correctly select the body's centre. This aspect is quite

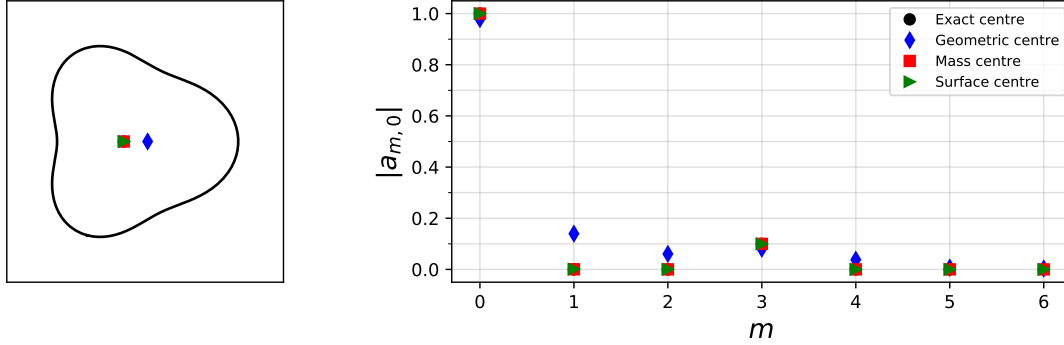


Figure 2.8: Computation of the centre with different methods for a droplet with a deformation Y_3^0 of amplitude $\eta = 0.1$. On the left, the contour of the interface of the body. On the right, a plot demonstrating the difference in the decomposition using the available methods for computing the centre.

challenging because we aim to reduce the influence of the eigen-mode 1, while also maintaining coherence of the centre as the droplet deforms. For spherical droplets affected by a symmetric deformation (even modes e.g. Y_2^l, Y_4^l , etc.) the computation of the centre is insignificant, with the highest relative error obtained being $3. \times 10^{-5}\%$ for the surface centre method.

In contrast, if the perturbation is asymmetrical (odd modes e.g. Y_3^l, Y_5^l , etc.), the choice of the centre of computation becomes more relevant. To show the difference in the computation of the coefficients $a_{m,l}$ we perform the spherical harmonic decomposition of a droplet initialized with a deformation of Y_3^0 with an amplitude $\eta = 0.1$ using the different available methods of setting the centre. The numerical conditions are the same as the previous validation. We expect the function to properly decompose the droplet into the inserted perturbation as to be able to expand this formulation into an oscillating drop.

We can observe in figure 2.8 the difference in the decomposition for a droplet with a deformation of $\eta = 0.1$ for mode 3 (Y_3^0). The cartesian, mass and surface centres are shown along with the exact centre of the droplet. It is noticeable that doing the decomposition without an appropriate centre can greatly alter the result. Nonetheless, it is important to note that this does not mean that the calculation is wrong. Since the Laplace expansion over the surface of the sphere depends on its reference frame, where the centre is placed will affect directly the way the grid of radius values $R(\theta, \varphi)$ is generated, hence, the decomposition will vary in amplitude of its $a_{m,l}$ coefficients. Figure 2.8 shows that the mass and surface centres more accurately represent the deformation introduced in the droplet. For the numerical domain discretized into a grid of 64^3 points, the relative error obtained considering the surface centre is 0.165%, while the error obtained using the mass centre is 0.145%.

2.4 Inertia tensor calculation

In a turbulent flow, the shape and mass distribution of the droplet can change dynamically due to the interaction of the droplet with the turbulent vortices. This requires real-time updates of the droplet's geometry and mass distribution for accurate inertia matrix computation. To find out its main directions, we calculate the inertia matrix I (Lalanne 2012, Chapter 5). It contains two types of component: the moments of inertia noted I_{xx} , I_{yy} , I_{zz} , which are respectively moments with respect to the x , y and z axes, and the products of inertia, I_{xy} , I_{xz} , I_{yz} , which model a geometric asymmetry of the mass distribution with respect to the respective planes (O, y, z) , (O, x, z) and (O, x, y) . The greater these moments, the further the mass is distributed from the axes or planes in question. The inertia matrix is written in the form

$$I = \begin{bmatrix} I_{xx} & -I_{xy} & -I_{xz} \\ -I_{xy} & I_{yy} & -I_{yz} \\ -I_{xz} & -I_{yz} & I_{zz} \end{bmatrix}, \quad (2.21)$$

$$\begin{aligned} I_{xx} &= \int_V \rho(y_o^2 + z_o^2)dV, & I_{yy} &= \int_V \rho(x_o^2 + z_o^2)dV, & I_{zz} &= \int_V \rho(x_o^2 + y_o^2)dV \\ I_{xy} &= \int_V \rho(x_o y_o)dV, & I_{xz} &= \int_V \rho(x_o z_o)dV, & I_{yz} &= \int_V \rho(y_o z_o)dV. \end{aligned} \quad (2.22)$$

Here, x_o , y_o , z_o are the coordinates of the o -th volume element relative to the centre.

The calculation of I is based on the VoF field and is carried out in the coordinate system with the centre of mass (see equation 2.17) as its origin. Since I is a symmetric matrix whose diagonal elements are positive, there is a frame of reference in which it is diagonal. This frame of reference is called the principal frame of inertia and its axes are called the principal axes of inertia. The eigenvalues of the matrix, denoted I_1 , I_2 and I_3 , are the principal moments of inertia. To ensure that the reference frame remains valid at all time (e.g. follow the drop rotation), it is necessary to ensure the continuity of the eigen values. The main inertial reference frame (v_1, v_2, v_3) provides the direction of the eigenvectors, but not their sign. By knowing the decomposition frame at time $n - 1$, $(v_{n-1,1}, v_{n-1,2}, v_{n-1,3})$, the inertial frame to be the frame at time n , $(v_{n,1}, v_{n,2}, v_{n,3})$ can be obtained. Denoting by v_3 the vector carried by the minor axis, the coordinate system must satisfy the following conditions:

1. If $v_{n-1} \cdot v_n < 0$ then $v_n = -v_{n-1}$. This is due to the fact that the eigenvectors cannot undergo a jump of more than 90° between two instants.
2. the eigenvectors given by v_n are obtained by minimizing the dot product $v_{n-1} \cot v_n$. This ensures that the axis are followed considering the smallest jump between vector position.

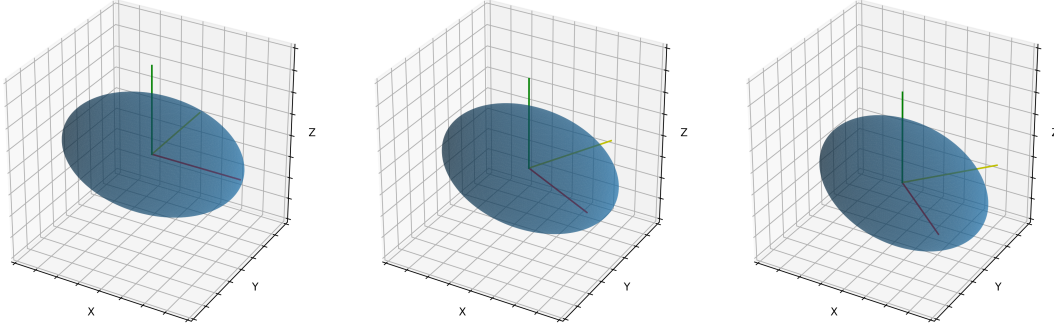


Figure 2.9: Tracking of the inertial reference frame over time. The red, yellow and green correspond to the principal axes of inertia.

By following these principal moments we can account for the droplet orientation variations influenced by the interaction with the surrounding fluid. This tracking can be seen in figure 2.9. It is important to note that this method does not grant that the provided reference frame will be the closest to an axisymmetric axis. It simply uses the inertia matrix as a mean to follow the drop's movement.

2.4.1 Validation of the inertia tensor framework

For the validation of the inertia tensor there are two steps to be followed. First, it is necessary to correctly compute the inertia tensor of the deformed droplets. Secondly, the evolution of the reference frame needs to be correctly tracked. To validate the computation of the inertia tensor two shapes are considered: a sphere and a spheroid. These two shapes are selected as these are the ones that more closely resemble the shape of the deformed droplet at the different stages of deformation.

$$I_{\text{sphere}} = \frac{2}{5} \left(\frac{4\pi R^2}{3} \right) \begin{bmatrix} R^2 & 0 & 0 \\ 0 & R^2 & 0 \\ 0 & 0 & R^2 \end{bmatrix} \quad (2.23)$$

$$I_{\text{spheroid}} = \frac{4}{3} \left(\frac{4\pi abc}{5} \right) \begin{bmatrix} b^2 + c^2 & 0 & 0 \\ 0 & a^2 + c^2 & 0 \\ 0 & 0 & a^2 + b^2 \end{bmatrix} \quad (2.24)$$

where a , b and c are the semi-axes aligned along the coordinate axes. For the generation of the spheroidal droplet, random values of a , b and c were considered to ensure that the computation works with any case.

In figure 2.10 the maximum error of the computed inertia tensor is shown as a function of the number of cells. It is observed that for both cases the error is below 0.1%, even for

coarse mesh definitions. These numerical errors are introduced by the computation of the centre of mass, as discussed in section 2.3.

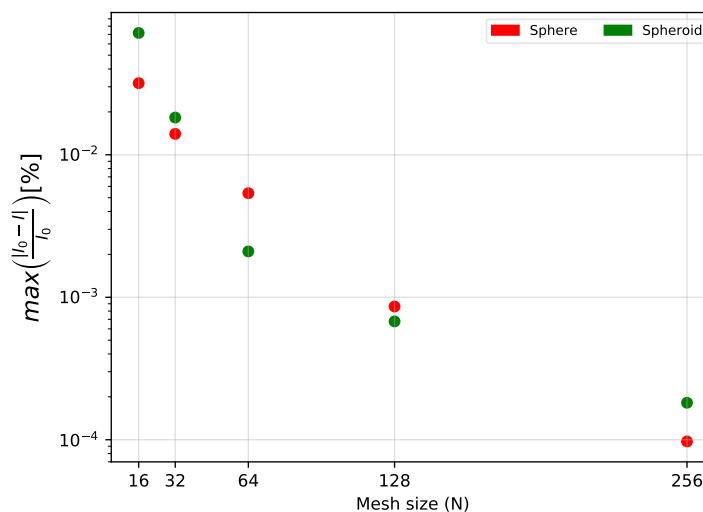


Figure 2.10: Maximum error in inertia tensor calculation for each case for different levels of mesh refinement.

2.5 Minkowski functionals

Another approach to characterize the morphology of a body is the use of Minkowski functionals. The Minkowski functionals are a set of morphological indicators that describe not only the envelope of the liquid system (surface) but also its topology (connectivity) and shape (geometric curvature) (Mantz et al. 2008). These indicators have been applied on various systems and are widely present in the literature dedicated to porous media (Arns et al. 2003, Mecke & Arns 2005) and cosmological structures (Mecke et al. 1993, Kersch et al. 2001). These indicators generalize the curvature integrals of smooth surfaces to those with singular bends (folds) or points.

The Minkowski functionals define four geometric quantities of a given body with a surface S : the volume V enclosed by the surface S , the surface area S , the area integrated mean curvature H and the area integrated Gaussian curvature G , considering

$$S = \int_S dS, \quad H = \int_S \frac{1}{2}(\kappa_1 + \kappa_2) dS, \quad G = \int_S \kappa_1 \cdot \kappa_2 dS \quad (2.25)$$

where κ_1 and κ_2 correspond to the two main curvature components and dS is an elementary surface element.

The set of Minkowski functionals has interesting properties, the most important being that they are additive (the Minkowski functionals of an ensemble of bodies is the sum

of their respective Minkowski functionals) and invariant to translation and rotation of the body. This means that the Minkowski functionals of an ensemble of systems is the sum of these functionals of each one of them (see figure 2.11). This is particularly useful for sprays made up of disjoint elements, where the Gaussian curvature at scale $d = 0$, $G(0)$, will therefore be directly proportional to the number N of drops in the spray. The previous assertion has been demonstrated in the works of Thieset et al. (2019) and Dumouchel et al. (2022).

2.5.1 Minkowski functionals computation

The Minkowski functionals computation is done using the routine of the same name implemented in the post-treatment code PyARCHER as a part of a previous study (Dumouchel et al. 2022).

The Minkowski functionals of a system are computed for all parallel surfaces at a distance Δx from the interface. The different parallel surfaces correspond to the operation of removing the region contained at a distance d from the interface. These systems are defined through the Levelset field, i.e. $\phi(\mathbf{x}) + \Delta x = 0$ considering only the region Ω_1 (see figure 2.1). The notion of parallel systems are presented in more detail in chapter 5.

This routine uses the *Surface operators* library of the in-house PyArcher for computing $S(d)$, $H(d)$, $G(d)$. These routines are based on earlier versions of the routines described by Mohamed et al. (2019) and Di Battista et al. (2019). The Minkowski functionals library allows the computation of the eroded functions for each individual structure present in the flow thanks to the labelization library present in PyARCHER by eroding the Levelset field. It also makes it possible to compute the Minkowski functionals considering the whole system as one. This is shown in figure 2.11.

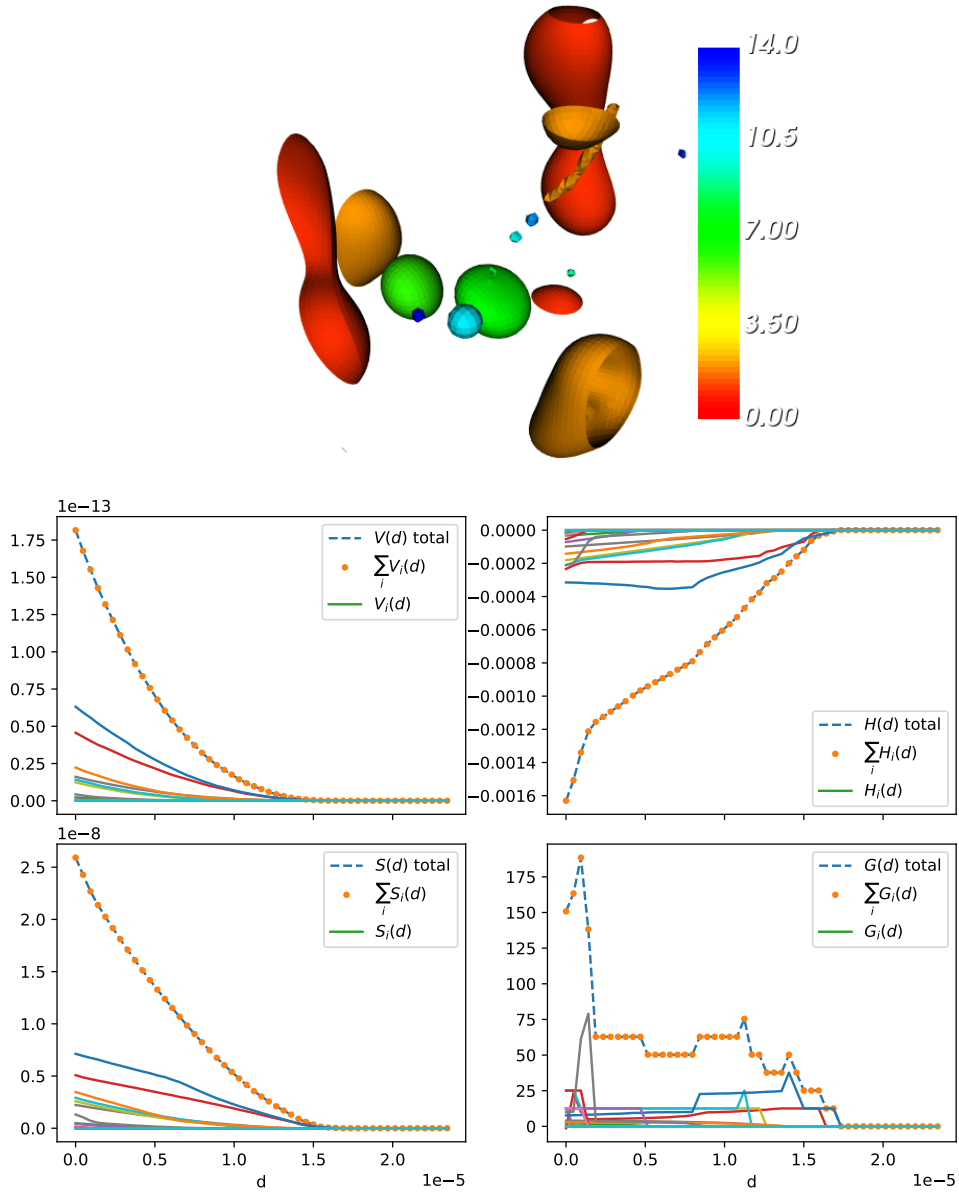


Figure 2.11: Example of the computation of the Minkowski functionals. (Top) The liquid structures are shown with their corresponding labels. (Bottom) Computation of the Minkowski functionals considering each system as independent and as an ensemble. Source: PyARCHER code examples.

Chapter 3

Linear oscillations of drops and bubbles

3.1 Introduction

The oscillations of drops and bubbles have been studied for over a century due to their importance in transport processes across interfaces. The first recorded analysis of linear drop shape oscillations dates back to Rayleigh (1879), who examined the vibrations of an inviscid spherical droplet in a vacuum, identifying the well-known solutions for the fundamental modes of motion characterized by modes $m = 2, 3, 4, \dots$, corresponding to the number of lobes across the interface. Lamb (1881) extended this work by considering the viscosity of the liquid sphere and the density of the surrounding medium. Chandrasekhar (1959) presented a normal-mode analysis of small amplitude oscillations of a viscous globe in a vacuum, deriving the characteristic equation for the angular oscillation frequency as a complex value described by the droplet Ohnesorge number. Reid (1960) later demonstrated that the forces driving the tendency to sphericity are due to surface tension, obtaining results identical to those of Lamb and Chandrasekhar for a self-gravitating sphere.

Miller & Scriven (1968) detailed the free oscillations of a viscous sphere immersed in a viscous ambient fluid, further generalising Lamb's work and providing an asymptotic estimation in the limit of weak viscous effects. Their analysis indicated that when both fluids are low-viscosity liquids, the primary contribution to the damping rate of oscillations comes from viscous dissipation in a boundary layer near the interface. Prosperetti (1980*a*) investigated droplet shape oscillations as an initial value problem, comparing his solutions with the normal-mode approach (Prosperetti 1980*b*), and analysed the oscillations of a viscous liquid drop surrounded by an immiscible liquid, finding a general solution to the dispersion relation between two fluids of varying densities and viscosity.

The introduction of viscosity into the system results in non-periodic drop-shape oscillations. To quantify this effect, Foote (1973) and Alonso (1974) were the first to numerically study viscous non-linear shape oscillations, with initial aspect ratios up to 1.9, considering an initially deformed state at rest given by a Legendre polynomial of mode m

or an initially oblate spheroid. Their work showed a decrease in the oscillation frequency for the first period with increasing aspect ratio for small viscosity. Tsamopoulos & Brown (1983) analytically studied non-linear oscillations of inviscid drops and bubbles for modes $m = 2, 3, 4$ and compared their results to those of Foote (1973) and Alonso (1974) for viscous drops oscillating in the fundamental modes. Tsamopoulos and Brown's results, compared against those of Foote and Alonso, showed that the effect of viscosity on the oscillation frequency is small for small Ohnesorge numbers (viscous versus inertial and surface tension forces), agreeing with Chandrasekhar's work, and observed that the drops spent a considerably longer part of each period in a prolate form than in an oblate one and observed a decrease in frequency caused by a larger initial amplitude deformation.

Lu & Apfel (1991) later investigated the effects of surfactants on the shape oscillations of drops, showing that the frequency change and damping constant are more pronounced for an extensible interface than an inextensible one, and the oscillation amplitude damps out faster when the interface exhibits rheological properties due to the generation of strong vorticity in the boundary layers. Lundgren & Mansour (1988) observed the oscillations of drops in zero gravity, considering weak viscous effects. They described a resonant energy transfer from the excited mode to higher frequencies due to the system's viscosity as another non-linear phenomenon in drop shape oscillations. The effect of mode coupling as a non-linear effect in droplet oscillations has been further analysed numerically by Patzek et al. (1991) and Basaran (1992). Both works considered the drop to be initially at rest. The coupling was found to be dependent on the initial state and viscosity of the droplet. Their results confirmed that viscous droplets released from an initial two-lobed shape spent less time in prolate form than inviscid droplets, consistent with previous literature.

Motivated by the recent work of Zrnić et al. (2022) on viscous drops in a vacuum and inspired by the linear stability analysis of a Newtonian ferrofluid cylinder immersed in a Newtonian fluid performed by Canu & Renoult (2021), a linear analysis of a Newtonian drop surrounded by a Newtonian fluid is performed. The characteristic equations derived from this analysis are compared with direct numerical simulation performed in the in-house code ARCHER. We study the dynamic effects of the surrounding fluid on the frequency and damping of perturbed droplets under different flow conditions. Modes of initial deformation up to mode $m = 6$ are investigated.

The use of a spherical harmonic decomposition framework, developed as part of previous work (Roa et al. 2023a,b) and described in detail in Chapter 2.3.2, is considered. Such framework has been used to study drop shape oscillations experimentally in the works of Kowalewski & Bruhn (1994), Risso & Fabre (1998) and Lalanne et al. (2019) as well as numerically in the work of Perrard et al. (2021).

This framework's utility comes from its ability to isolate each mode, allowing us to describe the droplet's oscillation frequency as an ensemble of different mode frequencies present, and thus observe not only the excited fundamental mode but also the coupling exhibited between all the present modes. In this work, we perform a linear shape analysis of a Newtonian droplet surrounded by a Newtonian fluid with symmetry in the azimuthal

coordinate for the general case where the two fluids have different densities and viscosities. After formulating this problem with various assumptions, the bulk equations for both fluids and the jump conditions across the interface between them are derived. A general dispersion relation in explicit form is then obtained, providing another formulation of this relation compared with previous studies. From the solution of the linearized system of equations, the corresponding first-order velocity field can be obtained provided that a set of initial conditions is imposed.

The droplets and bubbles are then initialized with both the theoretical velocity field and resting fluid, similar to the work of Simon (2024), in order to analyse its impact on drop shape oscillations. A similar study has recently been published on the weakly non-linear oscillations of a viscous droplet in vacuum (Smuda et al. 2024).

3.2 Linear theory

3.2.1 Formulation

We study the shape oscillations of a Newtonian globe immersed in a Newtonian surrounding fluid. In this chapter the oscillations of drops and bubbles will be explored. For simplicity purposes, throughout the chapter we will refer to both drops and bubbles as droplets except when specified. The droplet (dispersed phase) is of radius R_0 , viscosity μ_1 and density ρ_1 . These oscillations are assumed to be axisymmetric with respect to the azimuthal angular coordinate φ (see fig. 3.1). The surrounding fluid (continuous phase) is considered to be of viscosity μ_2 and density ρ_2 . The surface tension of the liquid drop against the ambient fluid is defined as σ . Both fluids are considered to be incompressible. Isothermal conditions are assumed and gravity is ignored.

We consider that the droplet departs from the spherical state by weakly disturbances characterized by the Legendre polynomials. The initial conditions of the drop surface are given by

$$\eta(\theta, 0) = \eta_0 P_m(\cos \theta), \quad \frac{\partial \eta}{\partial t}(\theta, 0) = 0, \quad (3.1)$$

These conditions determine the initial shape of the deformed droplet given by the Legendre polynomial P_m of order m while the second states that the drop surface has no radial velocity. The drop surface deformation is governed by the Legendre polynomial of the initial deformation. The amplitude parameter η_0 is assumed to be small compared to the radius of the unperturbed droplet. The drop surface is therefore described by the radial position $r_s = 1 + \eta(\theta, t)$, with η the non-dimensional deformation, measured with respect to the unperturbed droplet. The governing equations of this flow are described below.

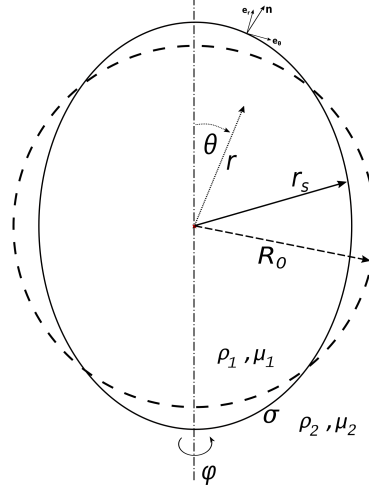


Figure 3.1: Representation of a perturbed Newtonian drop of radius R_0 , viscosity μ_1 and density ρ_1 surrounded by a Newtonian fluid of viscosity μ_2 and density ρ_2 , with interfacial tension σ .

3.2.2 Governing equations

The problem is characterized by the Navier-Stokes equations. The mass and momentum balance equations, valid for both the droplet and the surrounding fluid are expressed as a simplified form of equations 2.1 and 2.2

$$\nabla \cdot \mathbf{V}_i = 0, \quad (3.2)$$

$$\rho_i \left(\frac{\partial \mathbf{V}_i}{\partial t} + \mathbf{V}_i \cdot \nabla \mathbf{V}_i \right) = -\nabla p_i + \nabla \cdot \boldsymbol{\tau}_i, \quad (3.3)$$

In order to account for what happens at the interface we introduce the unit normal vector \mathbf{n} . It is defined at a point on the interface, in the direction towards the ambient fluid. The vector \mathbf{n} is given by

$$\mathbf{n} = \frac{\nabla S}{\|\nabla S\|} = \frac{1}{\sqrt{1 + \left(\frac{1}{r} \frac{\partial r_s}{\partial \theta}\right)^2}} \mathbf{e}_r - \frac{\frac{1}{r} \frac{\partial r_s}{\partial \theta}}{\sqrt{1 + \left(\frac{1}{r} \frac{\partial r_s}{\partial \theta}\right)^2}} \mathbf{e}_\theta, \quad (3.4)$$

where $S = r - r_s$ is introduced to characterize the position of the interface ($S = 0$). The kinematic boundary condition, which states that the rate of deformation of the drop surface equals the radial velocity at the position of the deformed surface, can be obtained by writing the mass balance equation at the interface without mass exchange between the two fluids,

$$\mathbf{V}_i \cdot \mathbf{n} = -\frac{1}{\|\nabla S\|} \frac{\partial S}{\partial t}, \quad \text{at } r = r_s. \quad (3.5)$$

We consider a no-slip condition at the interface (Tomotika 1935) given by

$$[\mathbf{V} \times \mathbf{n}] = 0, \quad \text{at } r = r_s, \quad (3.6)$$

with the convention $[A] = A_2 - A_1$. These equations lead to the continuity of the velocity components across the interface. To account for jump conditions for momentum, we describe the continuity in the tangential component of the stress acting at the interface as

$$[(\mathbf{n} \cdot \mathbf{T}) \times \mathbf{n}] = 0, \quad \text{at } r = r_s, \quad (3.7)$$

where $\mathbf{T}_i = -p_i \mathbf{I} + \tau_i$ is the stress tensor, considering \mathbf{I} the identity matrix. Lastly, the normal component of the stress acting on the interface is given by

$$[(\mathbf{n} \cdot \mathbf{T}) \cdot \mathbf{n}] = \sigma \kappa, \quad \text{at } r = r_s, \quad (3.8)$$

with $\kappa = \nabla \cdot \mathbf{n}$ the curvature of the interface. Considering the property $\mathbf{n} \cdot \mathbf{I} \times \mathbf{n} = 0$, the equations 3.7 and 3.8 are reduced to

$$(\mathbf{n} \cdot \tau_1) \times \mathbf{n} - (\mathbf{n} \cdot \tau_2) \times \mathbf{n} = 0, \quad \text{at } r = r_s, \quad (3.9)$$

$$p_1 - (\mathbf{n} \cdot \tau_1) \cdot \mathbf{n} = p_2 - (\mathbf{n} \cdot \tau_2) \cdot \mathbf{n} + \sigma \nabla \cdot \mathbf{n}, \quad \text{at } r = r_s. \quad (3.10)$$

The bulk equations (3.2,3.3), the conservation equations (3.5, 3.6) and as well as the jump conditions across the interface (3.7-3.10) are non-dimensionalized with the undeformed drop radius R_0 , the capillary timescale $\sqrt{\rho_1 R_0^3 / \sigma}$, characteristic velocity $\sqrt{\sigma / R_0 \rho_1}$ and the capillary pressure σ / R_0 . These characteristic values will be used for the rest of the chapter.

Given the geometry of the liquid droplet, the equations are formulated in polar coordinates, expanding the velocity into its radial and polar components $\mathbf{V}_i = (u_{ir} \mathbf{e}_r + u_{i\theta} \mathbf{e}_\theta)$. The dimensionless equations are linearized, and we thus obtain the equations for the perturbed quantities

$$\frac{1}{r^2} \frac{\partial(r^2 u_{ir})}{\partial r} + \frac{1}{r \sin \theta} \frac{\partial(u_{i\theta} \sin \theta)}{\partial \theta} = 0, \quad (3.11)$$

$$\frac{\partial u_{1r}}{\partial t} + \frac{\partial p_1}{\partial r} - Oh_1 \left(\frac{1}{r} \frac{\partial^2}{\partial r^2} (r^2 u_{1r}) + \frac{1}{r^2 \sin \theta} \frac{\partial}{\partial \theta} (\sin \theta \frac{\partial u_{1r}}{\partial \theta}) \right) = 0, \quad (3.12)$$

$$\frac{\partial u_{1\theta}}{\partial t} + \frac{1}{r} \frac{\partial p_1}{\partial \theta} - Oh_1 \left(\frac{1}{r^2} \frac{\partial}{\partial r} (r^2 \frac{\partial u_{1\theta}}{\partial r}) + \frac{1}{r^2} \frac{\partial}{\partial \theta} \left(\frac{1}{\sin \theta} \frac{\partial}{\partial \theta} (u_{1\theta} \sin \theta) \right) \right) = 0, \quad (3.13)$$

$$\rho_r \frac{\partial u_{2r}}{\partial t} + \frac{\partial p_2}{\partial r} - \mu_r Oh_1 \left(\frac{1}{r} \frac{\partial^2}{\partial r^2} (r^2 u_{2r}) + \frac{1}{r^2 \sin \theta} \frac{\partial}{\partial \theta} (\sin \theta \frac{\partial u_{2r}}{\partial \theta}) \right) = 0, \quad (3.14)$$

$$\rho_r \frac{\partial u_{2\theta}}{\partial t} + \frac{1}{r} \frac{\partial p_2}{\partial \theta} - \mu_r Oh_1 \left(\frac{1}{r^2} \frac{\partial}{\partial r} (r^2 \frac{\partial u_{2\theta}}{\partial r}) + \frac{1}{r^2} \frac{\partial}{\partial \theta} \left(\frac{1}{\sin \theta} \frac{\partial}{\partial \theta} (u_{2\theta} \sin \theta) \right) \right) = 0, \quad (3.15)$$

$$u_{ir} - \frac{\partial \eta}{\partial t} = 0 \quad \text{at} \quad r = 1, \quad (3.16)$$

$$\left(\frac{\partial u_{1\theta}}{\partial r} + \frac{1}{r} \frac{\partial u_{1r}}{\partial \theta} - \frac{u_{1\theta}}{r} \right) - \mu_r \left(\frac{\partial u_{2\theta}}{\partial r} + \frac{1}{r} \frac{\partial u_{2r}}{\partial \theta} - \frac{u_{2\theta}}{r} \right) = 0 \quad \text{at} \quad r = 1, \quad (3.17)$$

$$p_1 - 2Oh_1 \left(\frac{\partial u_{1r}}{\partial r} \right) - p_2 + 2\mu_r Oh_1 \left(\frac{\partial u_{2r}}{\partial r} \right) - \left(\frac{\partial^2 \eta}{\partial \theta^2} + \frac{\partial \eta}{\partial \theta} \cot \theta + 2\eta \right) = 0 \quad \text{at} \quad r = 1. \quad (3.18)$$

In the above equations $Oh_1 = \mu_1 / \sqrt{\rho_1 \sigma R_0}$ corresponds to the Ohnesorge number of the dispersed phase, $\rho_r = \rho_2 / \rho_1$ the density ratio and $\mu_r = \mu_2 / \mu_1$ the dynamic viscosity ratio. Due to the axisymmetric properties of the problem at hand, the components in the azimuthal direction \mathbf{e}_φ are not present. Due to the shape of the initial conditions presented in equation 3.1, the sought solution is of the form $\eta(\theta, t) = \hat{\eta} P_m(\cos \theta) e^{-\alpha_m t}$, with $\hat{\eta}$ the first-order initial surface amplitude and α_m the complex angular frequency for the deformation mode m .

3.2.3 Solution of the dispersion relation

Given the incompressibility assumptions of the flow and that only two-dimensional axisymmetric flow fields are investigated, the velocity in each fluid can be expressed using a Stokes stream function $\psi_i(r, \theta, t)$ such that $u_{ir} = -\frac{1}{r^2 \sin \theta} \frac{\partial \psi_i}{\partial \theta}$ and $u_{i\theta} = \frac{1}{r \sin \theta} \frac{\partial \psi_i}{\partial r}$.

By taking the curl of the linearized momentum equation for the dispersed phase in a vectorial form (Tomotika 1935) using Eq. 3.12-3.13, we obtain the fourth-order PDE

$$\left(\frac{1}{Oh_1} \frac{\partial}{\partial t} - E_s^2 \right) (E_s^2 \psi_1) = 0, \quad \text{where} \quad E_s^2 = \frac{\partial^2}{\partial r^2} + \frac{\sin \theta}{r^2} \frac{\partial}{\partial \theta} \left(\frac{1}{\sin \theta} \frac{\partial}{\partial \theta} \right) \quad (3.19)$$

This equation can be solved by using separable variables. The resulting stream functions ψ_1 is then represented by

$$\psi_{1,m} = [A_m r^{m+1} + B_m q_1 r j_m(q_1 r)] P'_m(\cos \theta) \sin^2 \theta e^{-\alpha_m t}, \quad (3.20)$$

where A_m and B_m are determined by kinematic and dynamic boundary conditions, $P'_m(\cos \theta)$ is the first-order derivative of the Legendre polynomial P_m , j_m is a spherical Bessel function of the first kind and order m and $q_1 = \sqrt{\alpha_m/Oh_1}$, is obtained from the Eq. 3.19.

Following the same procedure for the continuous phase momentum equations (Eq. 3.14 and 3.15) we recover the following fourth-order PDE

$$\left(\frac{\rho_r}{\mu_r Oh_1} \frac{\partial}{\partial t} - E_s^2 \right) (E_s^2 \psi_2) = 0. \quad (3.21)$$

The corresponding stream function for the ambient fluid must be determined such that it is consistent when the radial coordinate goes to infinity. The spherical Bessel functions do not converge to zero when their argument $q_i r$ approaches infinity, but rather oscillate around it. To ensure the convergence the solution for the continuous phase is written in terms of the spherical Hankel function $h_m^{(1)}(qr) = j_m(qr) + iy_m(qr)$. Then, the stream function of the outer fluid is given by

$$\psi_{2,m} = [C_m r^{-m} + D_m q_2 r h_m^{(1)}(q_2 r)] P'_m(\cos \theta) \sin^2 \theta e^{-\alpha_m t}, \quad (3.22)$$

where C_m and D_m are determined by kinematic and dynamic boundary conditions and $q_2 = \sqrt{\rho_r \alpha_m / \mu_r Oh_1}$ is obtained from Eq. 3.21.

The radial and angular components of the linearized velocity vector are recovered by replacing Eq. 3.20 and 3.22 in the Stokes functions

$$u_{1r} = - \left[A_m r^{m-1} + B_m q_1^2 \frac{j_m(q_1 r)}{q_1 r} \right] m(m+1) P_m(\cos \theta) e^{-\alpha_m t}, \quad (3.23)$$

$$u_{1\theta} = \left[A_m (m+1) r^{m-1} + B_m q_1^2 \left(\frac{(m+1) j_m(q_1 r)}{q_1 r} - j_{m+1}(q_1 r) \right) \right] \sin \theta P'_m(\cos \theta) e^{-\alpha_m t}, \quad (3.24)$$

$$u_{2r} = - \left[C_m r^{-m-2} + D_m q_2^2 \frac{h_m^{(1)}(q_2 r)}{q_2 r} \right] m(m+1) P_m(\cos \theta) e^{-\alpha_m t}, \quad (3.25)$$

$$u_{2\theta} = \left[-C_m r^{-m-2} + D_m q_2^2 \left(h_{m-1}^{(1)}(q_2 r) - \frac{m h_m^{(1)}(q_2 r)}{q_2 r} \right) \right] \sin \theta P'_m(\cos \theta) e^{-\alpha_m t}. \quad (3.26)$$

The pressure fields can be obtained by integration of one component of the momentum equation as

$$p_1 = -\alpha_m A_m (m+1) r^m P_m(\cos \theta) e^{-\alpha_m t} \quad (3.27)$$

$$p_2 = \alpha_m \rho_r C_m m r^{-m-1} P_m(\cos \theta) e^{-\alpha_m t} \quad (3.28)$$

By replacing these terms into the linearized kinematic and shear stress boundary conditions we can then recover the constants A_m , B_m , C_m , D_m by considering the properties of the spherical Bessel functions $j'_m(x) = \frac{m}{x} j_m(x) - j_{m+1}(x)$ and $j_{m+1}(x) = \frac{2m+1}{x} j_m(x) - j_{m-1}(x)$ Brown (2007)(Ch. 13.4.1).

We finally obtain a solution of the form

$$\begin{aligned} \Omega_m = \frac{\alpha_{m,0}^2}{\alpha_m^2} = -1 - \frac{m}{m+1} & \left[\rho_r - \mu_r \gamma \frac{H_m^{(k)} \left(\sqrt{\frac{\rho_r \alpha_m}{\mu_r O h_1}} \right)}{\alpha_m} O h_1 \right] \\ & + [(2m+1) - \gamma] \frac{J_m \left(\sqrt{\frac{\alpha_m}{O h_1}} \right)}{\alpha_m} O h_1 + \frac{2m O h_1}{\alpha_m} (1 - \mu_r) (m+2 + \gamma) \end{aligned} \quad (3.29)$$

with

$$\gamma = \left[\frac{2(m^2 - 1) + (2m+1)(2 - J_m(\sqrt{\frac{\alpha_m}{O h_1}})) - 2\mu_r m(m+2)}{(2 - J_m(\sqrt{\frac{\alpha_m}{O h_1}})) - \mu_r (2 + H_m^{(k)}(\sqrt{\frac{\rho_r \alpha_m}{\mu_r O h_1}}))} \right]. \quad (3.30)$$

This equation determines the complex angular frequency α_m , with $\alpha_{m,0} = \sqrt{m(m-1)(m+2)}$ being the solution of the angular frequency for an inviscid globe in vacuum (Rayleigh 1879). Here, we introduce the quotients of the spherical Bessel and Hankel functions

$$J_m(z) = z j_{m-1}(z)/j_m(z) \quad \text{and} \quad H_m^{(k)}(z) = z h_{m-1}^{(k)}(z)/h_m^{(k)}(z). \quad (3.31)$$

A change in notation when working with the spherical Hankel function is introduced due to the complex roots sought occurring in pairs. Given the fact that $\overline{h_m^{(1)}(x)} = h_m^{(2)}(\overline{x})$ then when looking for the roots in Eq. 3.29 it is necessary to consider the following values of the super-index k

$$k = \begin{cases} 1 & \text{if } \text{im}(\Omega_m) > 0 \\ 2 & \text{if } \text{im}(\Omega_m) < 0. \end{cases} \quad (3.32)$$

From equation 3.29, the negligible surrounding fluid case can be obtained by considering $\rho_r = \mu_r = 0$. The characteristic equation displayed draws the exact solution obtained by Chandrasekhar (1959) and that was studied by Zrnić et al. (2022) in their weakly non-linear analysis. These solutions are presented in figure 3.2 for modes $m = 2 - 4$. It

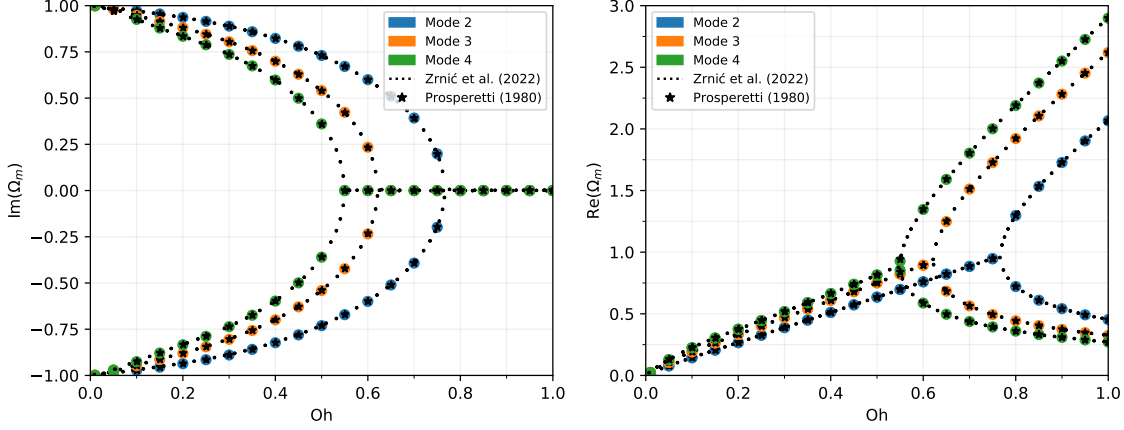


Figure 3.2: Solutions of the characteristic equation for varying Ohnesorge number for a surrounding fluid of negligible dynamical effects ($\rho_r = \mu_r = 0$). The imaginary and real portion of the non-dimensional frequency $\Omega_m = \alpha_m/\alpha_{m,0}$ are left and right respectively.

is shown that we have an exact agreement with the references, obtaining critical Ohnesorge numbers of 0.7665, 0.6209, 0.5496 for modes $m = 2, 3, 4$ respectively. This critical behaviour corresponds to the transition from damped oscillations to an aperiodic relaxation towards equilibrium. For Ohnesorge numbers below those critical values, the drop performs damped oscillations starting from the initial deformation. In this range, the characteristic equation of the drop exhibits complex conjugate solutions. For Ohnesorge numbers greater than the critical values, the initially deformed drop returns to its equilibrium shape by an aperiodic motion without an oscillation frequency, and for the damping rate of the initial deformation, two real solutions are found. The general form of this equation is consistent with the findings of Prosperetti (1980*b*). It can be seen that the solution of the dispersion relation is therefore dependent on the dimensionless values Oh_1 , ρ_r , and μ_r . Some examples are shown in Figure 3.3 for mode $m = 2$.

The results obtained from solving the dispersion relation are then normalized by the frequency $\omega_m = ((m - 1)m(m + 1)(m + 2))/(\rho_r m + m + 1)$. Since we have solved the two flow equations, we are also able to obtain a solution for different viscosity and density ratios. In figure 3.3, the solution to the dispersion relation for different viscosity and density ratios are plotted for different configurations of ρ_r and μ_r , for the values of $Oh_1 = 0.1Oh_2$, $Oh_1 = 0.5Oh_2$ and $Oh_1 = Oh_2$ (where $Oh_2 = \mu_2/\sqrt{\rho_2\sigma R_0}$) hence $\mu_r = 0.1\sqrt{\rho_r}$, $\mu_r = 0.5\sqrt{\rho_r}$ and $\mu_r = \sqrt{\rho_r}$ for simplicity. As seen in the figure, the existence of a pair of solutions of the imaginary term of Ω_m is maintained for all configurations. In the case of a drop in a negligible surrounding fluid (see Figure 3.2) a pair of solutions was also obtained for the real term of Ω . In Figure 3.3 (bottom) the same is not observed. The introduction of the viscosity term in the linearized equations returns a single solution for the damping rate, even for low viscosity ratios (as seen with $\rho_r = 0.01$ in figure

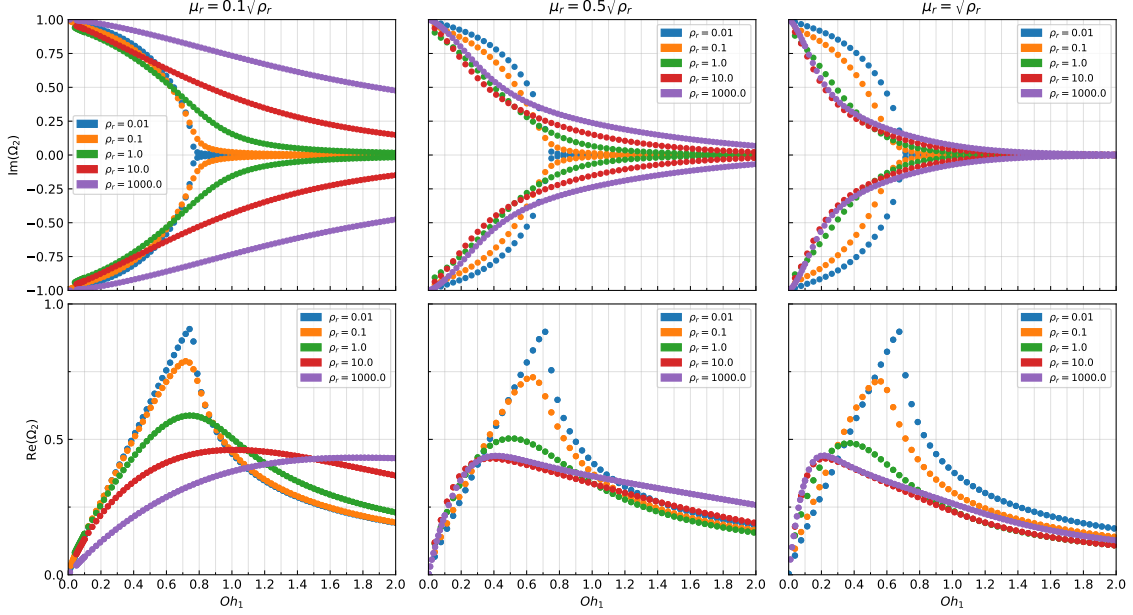


Figure 3.3: Solutions of the characteristic equation for varying Ohnesorge number for a surrounding fluid of varying dynamical effects considering that the inner and outer Ohnesorge numbers are equal ($\sqrt{\rho_r} = \mu_r$) for mode $m = 2$. The imaginary and real portion of the non-dimensional frequency $\Omega_2 = \alpha_2/\alpha_{2,0}$ are left and right respectively.

3.3). This could be due to the algorithm used to compute the solutions, although a similar phenomenon was also observed in Prosperetti (1980b).

It is observed that an increment of the Ohnesorge number ratios (given by $\mu_r = c\sqrt{\rho_r}$ with c a constant $\in [0, 1]$) involves a decrease in the critical Ohnesorge number due to the viscous effects of the surrounding fluid. This means the value of Ohnesorge in which the transition between the periodic to aperiodic damping motion for an initially deformed drop occurs decreases with increasing viscosity of the surrounding fluid.

Given that the characteristic equation of the drop exhibits a pair of solutions in the range of the Ohnesorge numbers explored, the first-order deformation of the drop surface is reformulated to account for this phenomenon as

$$\eta(\theta, t) = \left(\hat{\eta}^{(p)} e^{-\alpha^{(p)} t} + \hat{\eta}^{(n)} e^{-\alpha^{(n)} t} \right) P_m(\cos \theta), \quad \text{at } r = 1. \quad (3.33)$$

From the initial conditions 3.1 defining the initial drop shape and velocity at the drop interface we can then find the amplitudes $\hat{\eta}^{(p)}$ and $\hat{\eta}^{(n)}$

$$\hat{\eta}^{(p)} = -\frac{\alpha^{(n)}}{\alpha^{(p)} - \alpha^{(n)}}, \quad \hat{\eta}^{(n)} = \frac{\alpha^{(p)}}{\alpha^{(p)} - \alpha^{(n)}}. \quad (3.34)$$

The (p) and (n) superscripts denote the eigenvalue solutions with positive and negative

imaginary parts respectively. To account for the pair of solutions, the obtained amplitudes need to be introduced to the solutions of the stream function, velocity field, etc. for both fluids, having that

$$u_{1r} = u_{1r}^{(p)} + u_{1r}^{(n)}, \quad u_{1\theta} = u_{1\theta}^{(p)} + u_{1\theta}^{(n)}, \quad u_{2r} = u_{2r}^{(p)} + u_{2r}^{(n)}, \quad \dots \quad (3.35)$$

The constants A_m, B_m, C_m, D_m are

$$A_m = \eta \frac{\alpha_m}{(m(m+1))} \left(1 - ((2m+1) - \epsilon) \frac{J_m(q_1)}{q_1^2} \right) \quad (3.36)$$

$$B_m = \eta \frac{\alpha_m}{m(m+1)} \left(\frac{2m+1-\epsilon}{q_1^2 j_{m+1}(q_1)} \right) \quad (3.37)$$

$$C_m = \eta \frac{\alpha_m}{(m(m+1))} \left(1 - \epsilon \frac{H_m^k(q_2)}{q_2^2} \right) \quad (3.38)$$

$$D_m = \eta \frac{\alpha_m}{(m(m+1))} \left(\frac{\epsilon}{q_2^2 h_{m-1}^k(q_2)} \right) \quad (3.39)$$

The characteristic equation of an axisymmetric Newtonian droplet surrounded by a Newtonian fluid has been obtained considering a small perturbation imposed at the interface between the two fluids, similar to the equations derived in the work of Miller & Scriven (1968). This analysis allows to investigate the shape oscillations of the droplet at different modes of initial deformation with fluids of different characteristics. In the following sections, the linear theory is compared against numerical simulations performed with the in-house code ARCHER.

3.3 Numerical approach

Previous work done within the research group has explored the oscillations of low density and viscosity ratios (Aniszewski et al. 2014) and inviscid (Cordesse et al. 2020) ellipsoidal deformed droplets around a spherical shape in order to validate the in-house code ARCHER against Lamb's linear theory. One problem with that methodology is that the initialization given by an ellipsoidal shape is that it is inherently composed of multiple modes with little control on their distribution. For the initialization of the simulations of the present work, a droplet with an initial small amplitude deformation is generated considering the introduction of a single or multiple modes. The mathematical analysis presented earlier was developed considering axisymmetric conditions, hence the appearance of the Legendre polynomial function $P_m(\cos \theta)$. Nonetheless, we wish to validate the linear theory and relate it to the oscillations of droplets in turbulence (chapter 4) using the developed spherical harmonic framework described in section 2.3.2. To introduce

the perturbation in the surface of the droplet, we choose the amplitudes of the desired perturbation for the desired fundamental modes following

$$R(\theta, \varphi, t = 0) = R_0(t) + \sum_{m=2}^{\infty} \sum_{l=-m}^m a_{m,l}(t) Y_m^l(\theta, \varphi), \quad (3.40)$$

where $a_{m,l}(t)$ corresponds to the amplitude of the deformation over time and $Y_m^l(\theta, \varphi)$ is the spherical harmonic function, which is related to the Legendre functions P_m^l as

$$Y_m^l(\theta, \varphi) = \sqrt{(2m+1) \frac{(m-l)!}{(m+l)!}} P_m^l(\cos \theta) e^{il\varphi}. \quad (3.41)$$

Given the axisymmetric conditions of the considered problem, the value of the spherical harmonic degree is considered as $l = 0$.

The linear theory describes the flow field and the evolution of the drop surface at the first order. Due to this truncation, the conservation of volume during the shape oscillations is not guaranteed. For this reason, the radius $R_0(t)$ in equation 3.40 is described as a function of time, ensuring volume conservation. The non-dimensional drop volume $v(t)$ is given as

$$v(t) = \frac{2\pi}{3} \int_{-1}^1 R^3(\theta, t) d \cos \theta = \frac{4\pi}{3}, \quad (3.42)$$

so as for the undeformed state ($a_{m,l} = 0$) it is obtained that $R_0 = 1$. The initial shape of the body is as seen in figure 3.4a for a droplet deformed with $\eta_0 = 0.2$ and $m, l = 2, 0$. Given the axisymmetry of the problem at hand, computational time is reduced by simply simulating the oscillations of a quarter of the droplet. Given that the spherical harmonic decomposition developed as a part of a previous study (Roa et al. 2023a,b) has been built considering a three-dimensional body, we reconstruct the original droplet during the post-treatment. Since the goal of this work is to study the shape oscillations in different flow characteristics, we perform DNS for various Ohnesorge numbers as well as different density and viscosity ratios.

The existing literature following the oscillations of inviscid (Patzek et al. 1991, Tsamopoulos & Brown 1983) and viscous (Basaran 1992) drops through numerical means, studies the case in which only an initial deformation is considered in a droplet initially at rest. From solving the linear shape oscillations of a drop immersed in a surrounding fluid, equations describing the velocity and pressure fields are obtained from the Stokesian system in Sec. 3.2. Following the previously mentioned works, a set of droplets are initialized considering a system initially at rest, i.e. the drops are released from an initial static deformation. At the same time, a second set of droplets is initialized by introducing the velocity field obtained from the analytical equations at $t = 0$ obtained from equations 3.23, 3.24 and equations 3.25, 3.26 for the inner and outer fluid, respectively. The next step involves

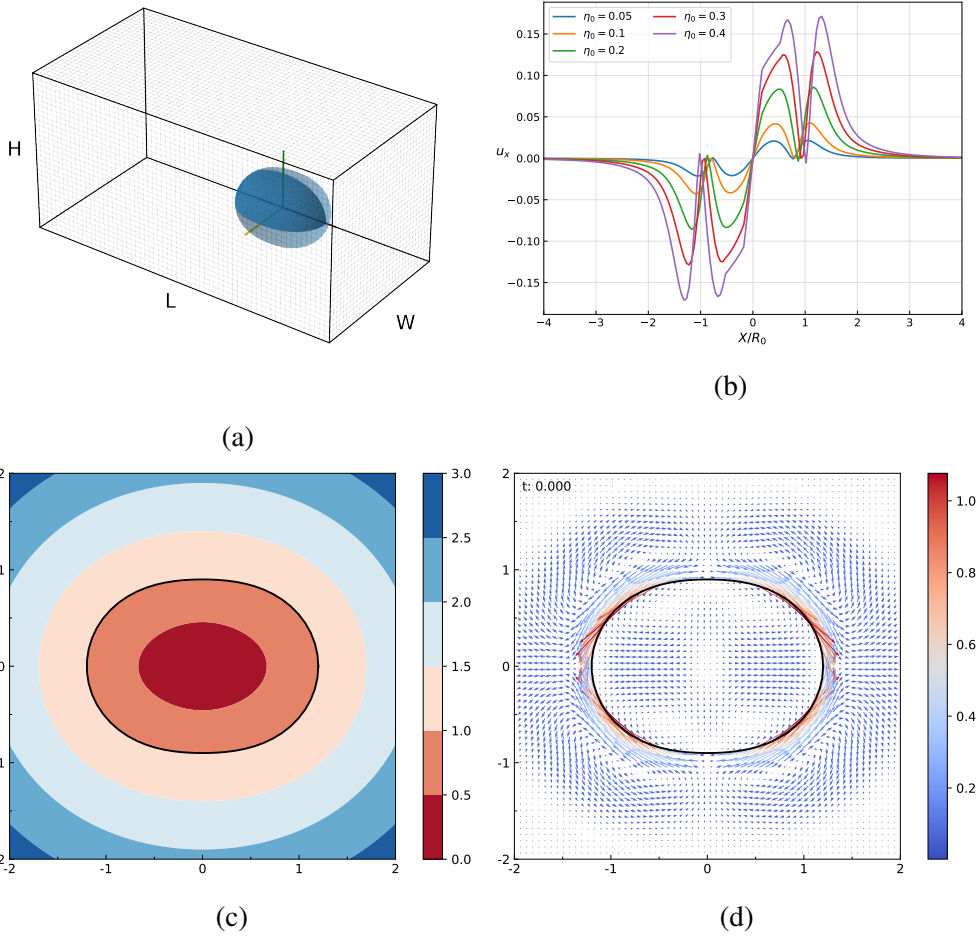


Figure 3.4: (a) Initialization of a droplet initially deformed by a spherical harmonic mode $m=2$ with $\eta_0 = 0.2$. The initialized shape is axisymmetric with respect to the x -axis represented in the red solid line. (b) the x component of the velocity field along the x -axis normalized by R_0 for different η_0 , with $Oh_1 = 0.1$. (c) The synthetic field Φ . (d) A visual representation of the first-order velocity field from the linear theory.

ensuring that the computed velocity field maintains the condition of being divergence-free (Eq. 2.1). To achieve this, a divergence correction strategy is employed through a Poisson step, where an artificial pressure field is introduced. This pressure field adjustment serves to align the computed velocity field with the principle of mass conservation, thus ensuring the accuracy of the results. Similar to the works of Simon (2024) in interfacial instabilities in a three-layer fluid system, we analyse both initialization conditions to inspect the shape oscillations of the droplet, and how the initialization method affects the linear and non-linear oscillations.

For the simulations presented in this chapter, the computational domain is set to $L = [-4R_0, 4R_0]$ and $W = H = [0, 4R_0]$, corresponding to a quarter of the simulated droplet (see Figure 3.4a), with the x-axis as the symmetry axis. For all simulations, a mesh of $128 \times 64 \times 64$ cells is considered. The size of the computational domain is justified by the necessary length needed to accurately represent the first-order velocity field in the whole domain. In figure 3.4b the velocity in the x direction along the x-axis is shown. For all cases studied, the domain is sufficiently large to converge towards zero.

The first-order solution is obtained by assuming that the drop's radius $r_s(\theta)$ equals to the undeformed drop radius. However, directly computing the velocity field at the interface for drops that are initially deformed poses a challenge within this framework. To address this limitation, a synthetic scalar field, denoted as Φ , is introduced. This scalar field serves as an artificial radius, where $\Phi = 0$ denotes the centre of the drop and $\Phi = 1$ is the interface. By utilizing this scalar field, we can effectively map the regions within and outside the droplet, allowing for the computation of the velocity field (see Figure 3.4c). The velocity field obtained from the linear development of the droplet shown in figure 3.4a is shown in figure 3.4d.

3.4 Cross-validation

3.4.1 Shape oscillations

In order to validate the linear theory developed with numerical data, a numerical library of droplets and bubbles of Ohnesorge numbers in the range of $Oh_1 = [0.1 - 0.7]$ has been generated. From these realizations, the frequency ω_m and the damping factor β_m were computed by using a Levenberg-Marquardt fitting algorithm. In figure 3.5, the results of the curve fit are plotted against the analytical solutions for density ratios of $\rho_r = [1 \times 10^{-3} - 1 \times 10^3]$, considering an initial amplitude deformation $\eta_0 = 0.1$ in the fundamental mode $m = 2$. It can be observed that through both initialization approaches both the frequency and damping are in good agreement with the linear theory up until the critical Ohnesorge values. This behaviour can be explained through the fitting algorithm used since the curve assumes a linear behaviour. Following the shape oscillations of each individual mode it is observed that the initialization with the theoretical velocity field does not yield a better agreement with the theory.

In order to observe how well the linear theory aligns with the numerical simulation, in figure 3.6 the shape oscillations of the excited modes $m = 2, 3, 4$ over time are presented and their evolution compared with the analytical solution obtained considering an $Oh_1 = 0.1$ and viscosity/density ratios 1×10^{-3} , 1 and 1×10^3 which from now on will be presented as droplet ($\rho_r = \mu_r = 1 \times 10^{-3}$), neutrally buoyant ($\rho_r = \mu_r = 1$) and bubble case ($\rho_r = \mu_r^2 = 1 \times 10^3$) respectively. As expected, the results show great agreement between the DNS and the linear theory, regardless of the initialization method used. It is

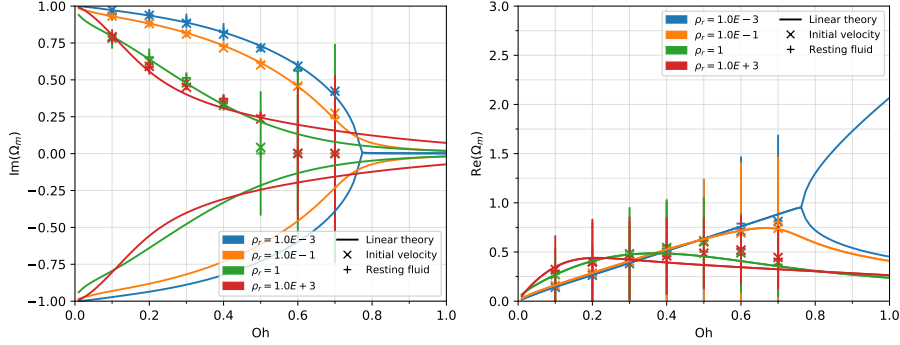


Figure 3.5: Solution of the dispersion relation for a fundamental mode $m = 2$ and varying density ratio $\rho_r = [1 \times 10^{-3}, 1 \times 10^3]$ against the fitted values of the frequency ω_m and damping rate β_m obtained from the numerical realizations through initialization with the analytical first-order velocity field and static deformation for an initial deformation $\eta_0 = 0.1$. The error bars correspond to the covariance of the curve fit.

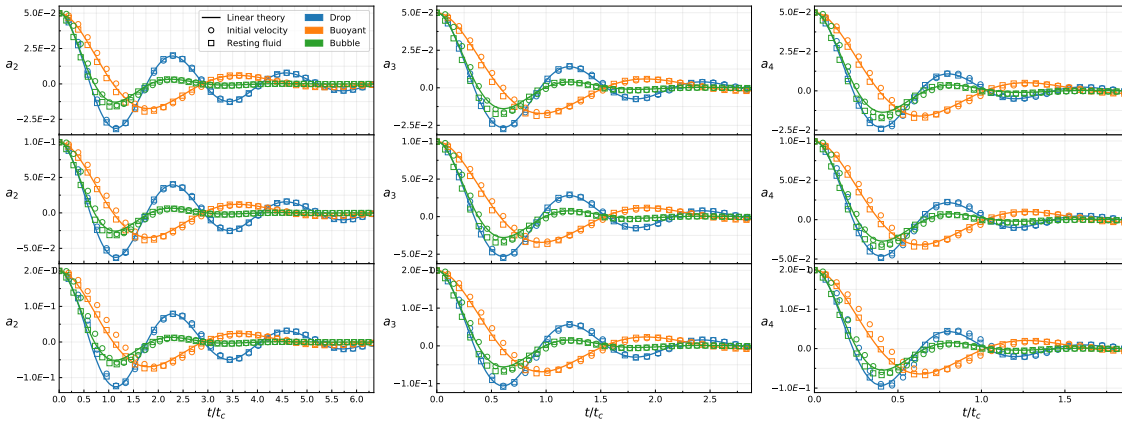


Figure 3.6: Oscillations of droplets initialized with the fundamental modes $m = 2 - 4$ considering an $Oh = 0.1$ and an initial amplitude of $\eta_0 = 0.05$ (top), $\eta_0 = 0.1$ (centre) and $\eta_0 = 0.2$ (bottom).

observed though that the inclusion of the first-order velocity field causes a small overshoot at the beginning of the simulation (as seen in figure 3.6) as the initial deformation η_0 increases. This can be seen in greater detail in Figure 3.6 (bottom), although this behaviour is displayed as soon as $\eta_0 \geq 0.05$ for the bubble case. This overshoot has been linked to an increase in the velocity field in the first time steps of the simulation and corresponds to a purely numerical error. After the first couple of time-steps, the velocity field regulates and follows the theoretical field correctly.

In figure 3.7, the time the droplet spends in prolate state is shown. The results from the two initialization methods are shown and compared with existing literature for a drop

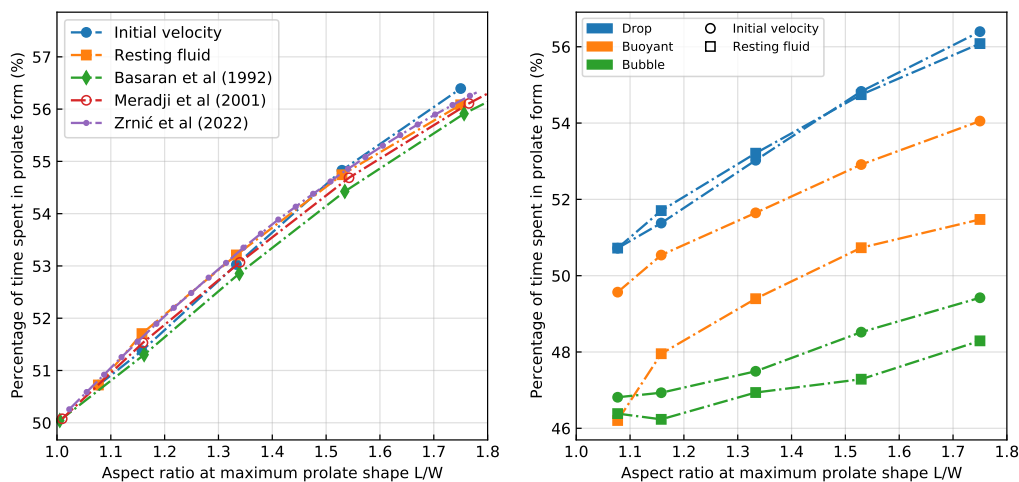


Figure 3.7: Time percentage spent in prolate form as a function of the initial drop aspect ratio L/W compared to the existing literature (left) and analysing the different test cases of this work for a drop in vacuum, a fluid of equivalent dynamic effects and bubble (right).

initially excited in the fundamental mode $m = 2$ and considering an $Oh_1 = 0.1$. The times are extracted from the first period of the drop-shape oscillation. As shown in figure 3.7 (left), the initialization with the first-order velocity field does not significantly impact the drop shape oscillations when considering an outer fluid of negligible dynamic effects. In both cases, we can notice the tendency to display non-linear effects, i.e. the excess time of the drop spent in the prolate shape during one period (Basaran 1992, Tsamopoulos & Brown 1983, Zrnić et al. 2022).

In Figure 3.7 (right) the prolate time for the three studied cases is shown. The initialization method has a far more important effect on the excess time of the drop in prolate shape for the cases in which the ambient fluid has equal or greater dynamic effects. It is observed that in the case of oscillating bubbles, the shape oscillations spend a greater amount of the first period in an oblate state, contrary to the case of drops in vacuum. For the case in which both fluids have equal dynamical effects, the behaviour greatly differs by changing the initial conditions, obtaining closer values to those expected when initializing with the theoretical velocity field. For both of them though it is seen that the droplet spends more time in the prolate state when the initial perturbation is greater or equal to $\eta = 0.1$ and $\eta = 0.2$. These results show that introducing the first-order velocity field obtained from the linear theory does not guarantee a linear oscillatory motion of perturbed droplets. It is necessary to point out though that whilst the droplet in vacuum results are well captured and in good agreement with the non-linear oscillations' literature, the buoyant and bubble cases are not physical. The time spent in prolate state should converge to 50% when decreasing the amplitude of the initial perturbation. The error is perceived as purely numerical. Further work will be done to understand this problem. From the

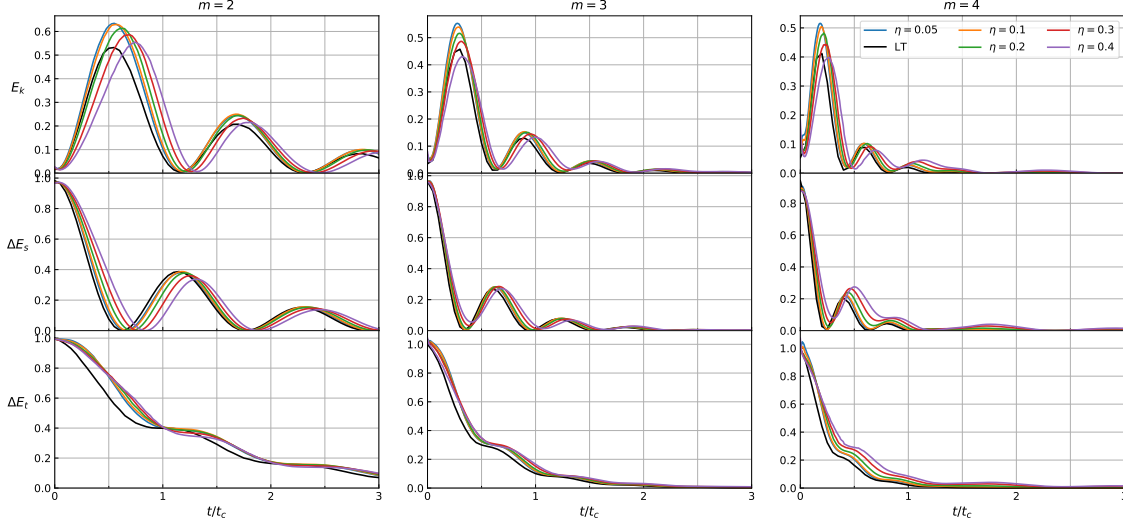


Figure 3.8: Evolution of the drop kinetic energy E_k (top), variation of surface energy ΔE_s (centre) and variation of total energy ΔE_t (bottom) for a droplet in vacuum ($\rho_r = \mu_r = 1 \times 10^{-3}$) for modes $m = 2, 3, 4$ from left to right respectively. The red dotted-lines correspond to the linear theory results.

current understanding, this may be related to the initial overshoot discussed and presented in figure 3.6.

3.4.2 Energetic approach

Having a database of different realizations including different modes of deformation and amplitudes, the kinetic energy E_k , the variation of surface energy ΔE_s and the corresponding variation in total energy ΔE_t can be computed from the evolution of the DNS velocity field and interface change. The same approach has been recently explored in the work of Smuda et al. (2024) for droplets in vacuum. These quantities in their non-dimensional form are defined as

$$E_k = \frac{1}{2} \rho_i \int_v (\mathbf{V}_i \cdot \mathbf{V}_i) dv, \quad \Delta E_s = \sigma \left(\int_a 1 d_a - 4\pi \right), \quad \Delta E_t = E_k + \Delta E_s. \quad (3.43)$$

In figures 3.8, 3.9, and 3.10, the bulk kinetic energy, surface energy, and total energy variation of the oscillating droplets are presented for $Oh_1 = 0.1$. These values are derived from droplets initialized with the first-order velocity field, allowing comparison with the linear theory for three different cases ($\rho_r = 1 \times 10^{-3}, 1, 1 \times 10^3$ and $\mu_r = 1 \times 10^{-3}, 1, \sqrt{1 \times 10^3}$ respectively). Given the negligible nature of the continuous

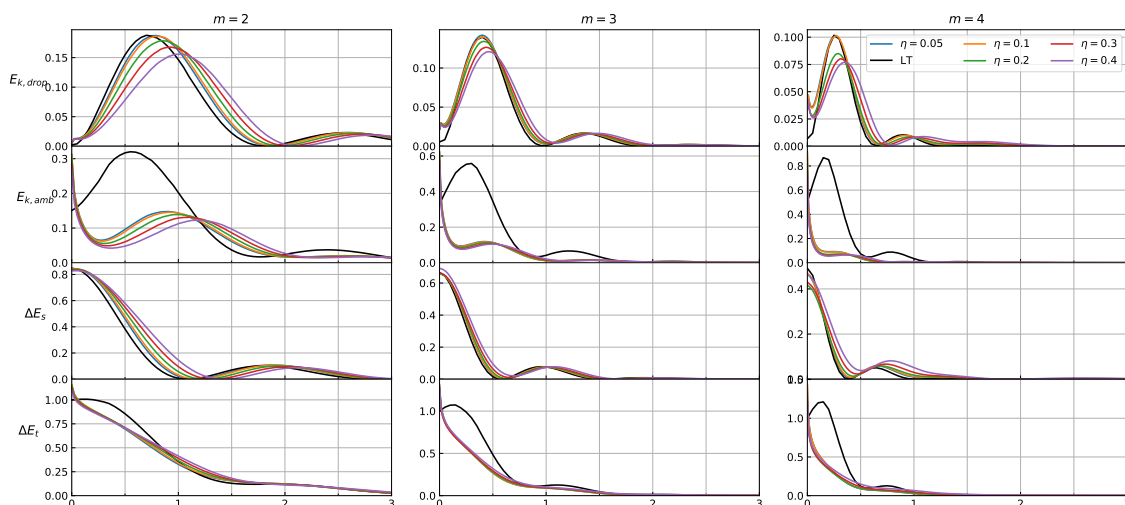


Figure 3.9: Evolution of the drop kinetic energy $E_{k,\text{drop}}$, ambient kinetic energy $E_{k,\text{amb}}$, variation of surface energy ΔE_s and variation of total energy ΔE_t for a droplet in a surrounding fluid of equivalent dynamic effects ($\rho_r = \mu_r = 1$) for modes $m = 2, 3, 4$ from left to right respectively. The red dotted-lines correspond to the linear theory results.

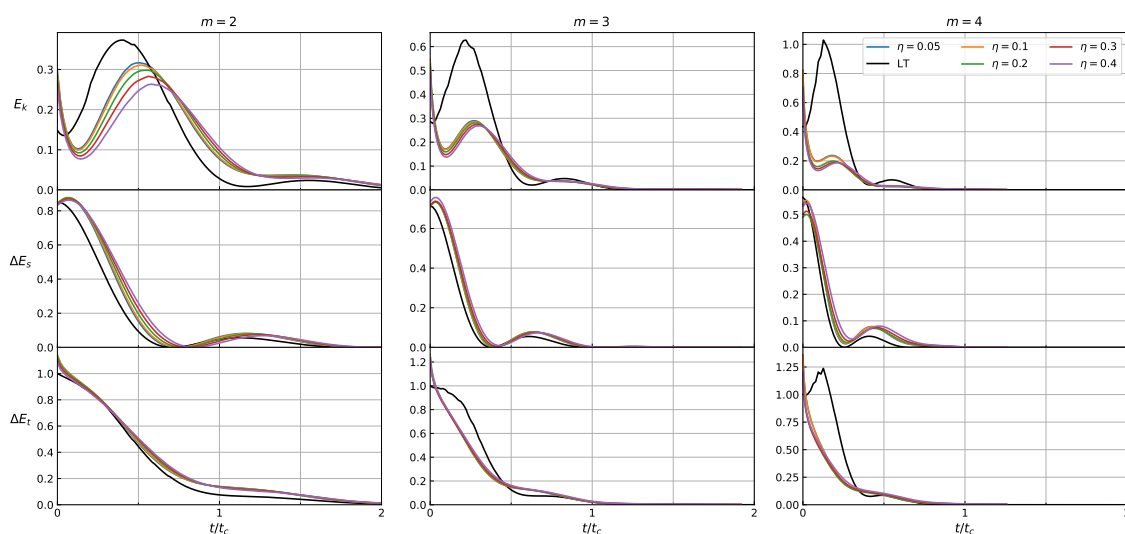


Figure 3.10: Evolution of the ambient kinetic energy E_k (top), variation of surface energy ΔE_s (centre) and variation of total energy ΔE_t (bottom) for a bubble in a fluid of equal Oh ($\rho_r = \mu_r^2 = 1 \times 10^3$) for modes $m = 2, 3, 4$ from left to right respectively. The red dotted-lines correspond to the linear theory results.

phase in the vacuum case and the dispersed phase in the bubble case, the respective kinetic energy results are not presented and are only included when both phases are equal.

The findings for mode $m = 2$ are compared against the theoretical values of the linear theory. The kinetic energy of the droplet exhibits the expected behaviour and aligns well with linear theory predictions for small deformations, though there is a slight overshoot for smaller amplitudes in the vacuum case. At higher deformation amplitudes, the kinetic energy shows quasi-periodicity, corresponding to excited mode oscillations, with dissipation increasing from the drop to the bubble scenario as anticipated.

The surface energy difference is illustrated in the middle of figures 3.8, 3.9, and 3.10 for initial deformation modes $m = 2, 3, 4$. This corresponds to the deformation of the drop compared to the spherical state. The results are normalized using the theoretical initial energy of the system at $t = 0$. Higher modes of deformation are linked with greater surface energies and a steeper decay of surface energy with increasing mode. It is observed that for excited modes $m \geq 3$, the first kinetic energy minimum does not reach zero for large amplitude deformations.

In all cases, this is noticeable from $\eta_0 \geq 0.05$ for $m = 3$ and $m = 4$. The same phenomenon occurs for surface energy in mode $m = 3$ for $\eta_0 \geq 0.2$ in the droplet case, $\eta_0 \geq 0.3$ in the buoyant case, and $\eta_0 \geq 0.4$ in the bubble case. Similarly, for mode $m = 4$, it occurs at $\eta_0 \geq 0.2$ in the droplet case, $\eta_0 \geq 0.1$ in the buoyant case, and $\eta_0 \geq 0.05$ in the bubble case. These variations are due to the energy exchange between the dispersed and continuous phases, indicating that the drop's kinetic energy is not entirely converted into surface energy and vice versa at the first maxima and minima respectively.

The total energy is depicted at the bottom of figures 3.8, 3.9, and 3.10. Typically, the total energy E_t dissipates over time due to viscosity. For the three cases presented, the dissipation rate of the total energy is highest during the drop's retraction motion, transitioning from a deformed state to spherical, as seen in the two slopes present in each prolate-oblate period. This change in decay rate aligns with the point of the highest kinetic energy and is already predicted by linear theory. The numerical results show a shift in the period of the drop's energy with increasing initial deformation, expected given the non-linearity of the oscillations. The maximum kinetic energy from the numerical simulations is higher than the linear theory prediction, possibly due to domain constraints.

A significant discrepancy is found between the theoretical and numerical kinetic energy of the surrounding fluid. First, the initial value of $E_{k,amb}$ differs from the linear theory due to corrections made to the velocity field to ensure the divergence-free condition. Additionally, in the buoyant and bubble cases, where ambient fluid dynamic effects are considerable, accurate capture of the interface interaction with the medium is necessary. As seen in figure 3.4a, the system's velocity concentrates around the interface. Secondly, the behaviour significantly deviates from theory in the buoyant and bubble cases, which could be due to domain size or substantial changes to the field while maintaining the divergence-free flow condition.

In figures 3.11, 3.12, and 3.13, the bulk kinetic energy, surface energy, and total energy

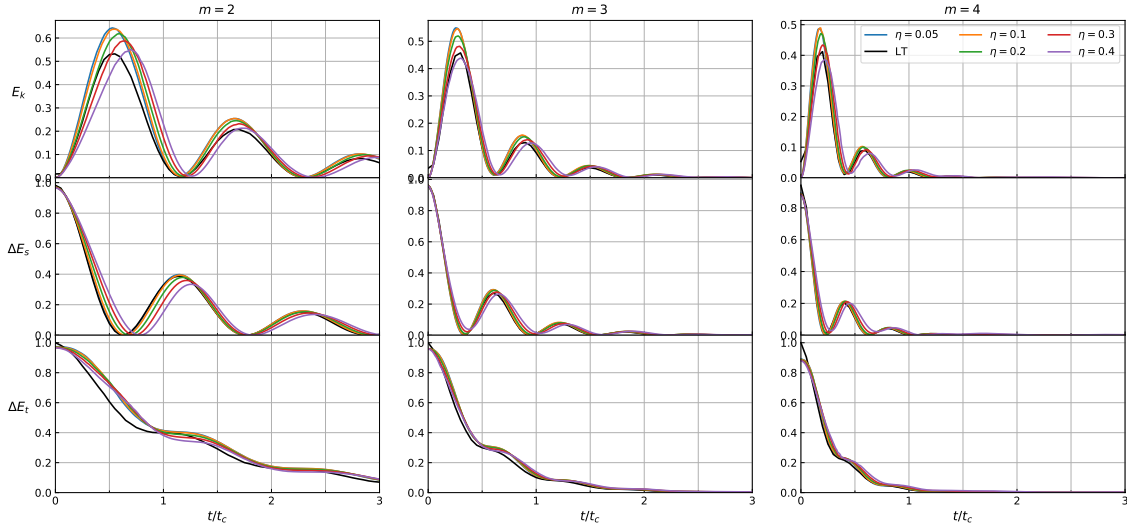


Figure 3.11: Evolution of the drop kinetic energy E_k (top), variation of surface energy ΔE_s (centre) and variation of total energy ΔE_t (bottom) for a droplet in vacuum ($\rho_r = \mu_r = 1 \times 10^{-3}$) for modes $m = 2, 3, 4$ from left to right respectively with an initial resting fluid condition. The red dotted-lines correspond to the linear theory results.

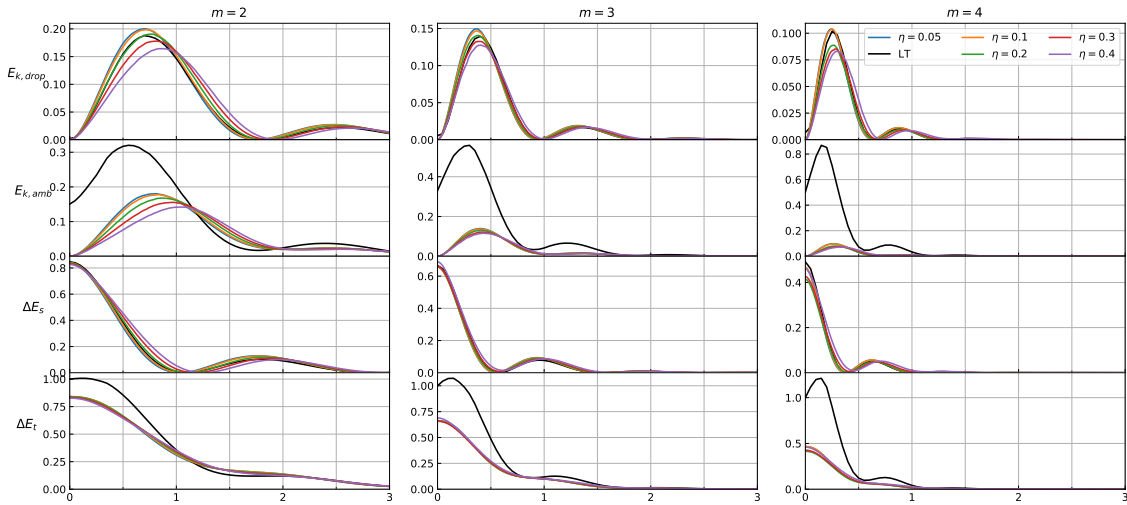


Figure 3.12: Evolution of the drop kinetic energy $E_{k,drop}$, ambient kinetic energy $E_{k,amb}$, variation of surface energy ΔE_s and variation of total energy ΔE_t for a droplet in a surrounding fluid of equivalent dynamic effects ($\rho_r = \mu_r = 1$) for modes $m = 2, 3, 4$ from left to right respectively with an initial resting fluid condition. The red dotted-lines correspond to the linear theory results.

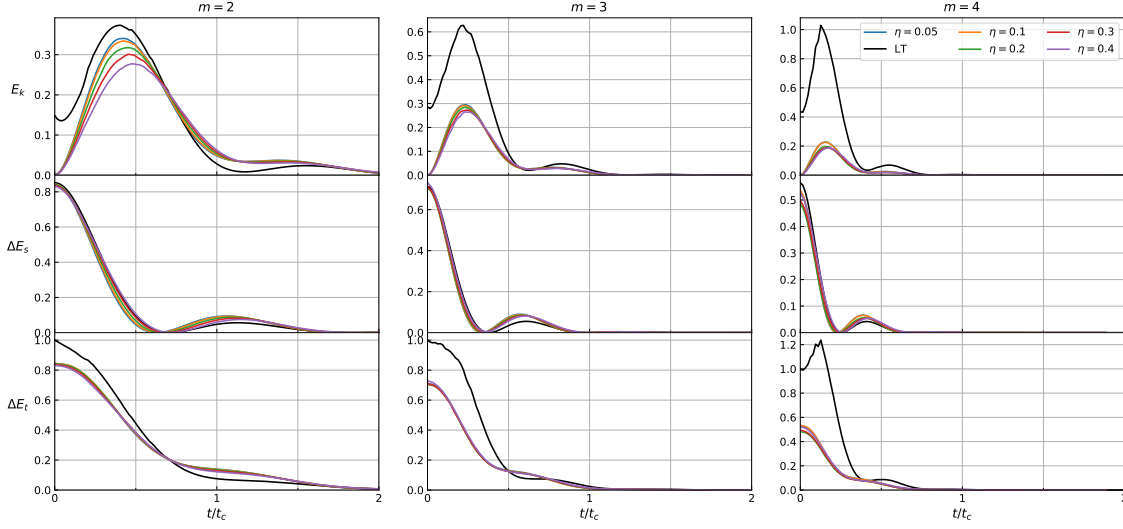


Figure 3.13: Evolution of the ambient kinetic energy E_k (top), variation of surface energy ΔE_s (centre) and variation of total energy ΔE_t (bottom) for a bubble in a fluid of equal Oh ($\rho_r = \mu_r^2 = 1 \times 10^3$) for modes $m = 2, 3, 4$ from left to right respectively with an initial resting fluid condition. The red dotted-lines correspond to the linear theory results.

variation of the oscillating droplets are shown, with the same characteristics but initialized with zero velocity. For all cases, the results do not vary greatly between different initializations. As in the previous instance, the kinetic energy in the droplet $E_{k,\text{drop}}$ overshoots for smaller amplitude deformations across all modes shown for the drop in vacuum and buoyant cases. Similarly, for droplets initialized with the linear velocity field, the values of $E_{k,\text{amb}}$ differ significantly from the linear theory, with discrepancies increasing with higher modes. The evolution of the total energy is captured accurately, even though the initial value differs due to initialization with a resting fluid. For the bubble case, the maximum $E_{k,\text{amb}}$ is slightly better captured, especially for mode $m = 2$, even when starting from a resting fluid. As expected, the dissipation rate increases with higher fundamental modes and initial deformation in all cases shown. The highest dissipation rate occurs in the bubble case, due to the greater viscosity of the surrounding fluid.

3.5 Beyond linear theory

3.5.1 Coupling between modes

It is well established that the introduction of viscosity leads to the coupling of different oscillation modes as a non-linear effect. Basaran (1992) identified that this mode coupling depends on the initial state of the drop and its viscosity. The work of Kowalewski & Bruhn

(1994) and later the work of Smith (2010) further confirmed the presence of non-linear phenomena for amplitudes exceeding 10% of the undeformed drop radius, highlighting the influence of viscosity on mode coupling.

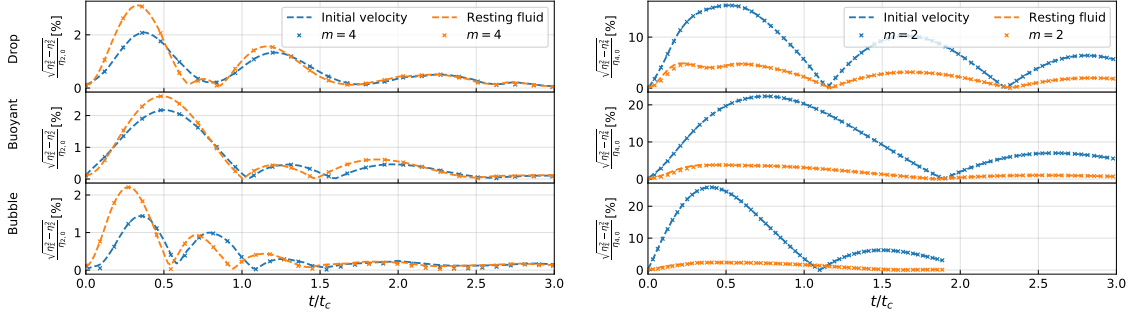


Figure 3.14: Percentage of modes different to the excited one in the total deformation for shape oscillations of a droplet initialized with the fundamental modes $m = 2$ (left) and $m = 4$ (right) and initial deformation amplitude $\eta_0 = 0.1$ considering $Oh_1 = 0.1$ for the drop, buoyant and bubble cases (from top to bottom respectively).

The evolution of a droplet initially deformed by modes $m = 2$ and $m = 4$ is observed in Figure 3.6, considering both initialization methods. There is good agreement between the numerical and analytical approaches concerning linear theory, independent of the initial conditions. To visualize the interaction of the drop oscillations with the non-initially-excited modes, Figure 3.14 shows the difference between the amplitude deformation given by the rest of the modes ($\eta_{\Sigma}^2(t) = \sum_{m=0}^6 a_{m,l}^2(t)$) and the amplitude of the excited fundamental mode over time (η_m^2), versus the initial deformation amplitude for an initial amplitude $\eta_0 = 0.1$ for both modes. The results indicate that even if the initial drop shape involves a single mode, other modes appear during its lifetime, demonstrating the non-linear characteristics of the drop shape oscillations. Specifically, the oscillations different from the excited mode are entirely linked to modes $m = 4$ and $m = 2$ for the oscillations of excited modes 2 and 4 respectively, as shown in figure 3.14. This coupling has been observed multiple times in existing literature (Tsamopoulos & Brown 1983, Basaran 1992, Risso 2000, Ravelet et al. 2011, Zrnić & Brenn 2021, Zrnić et al. 2022, Roa et al. 2023b), showing that the coupling between different even modes depends on the initial condition of the flow.

Realizations initialized with the first-order velocity field demonstrate a slightly lower coupling effect in the first half of the first period for the fundamental mode $m = 2$. However, for the excited mode $m = 4$, initialization seems to play a more significant role. This phenomenon is strongly influenced by the viscous effects of the surrounding fluid in terms of dissipation, as expected. Nonetheless, the effects of the coupled modes do not vary greatly for the case in which mode 2 is excited. A different behaviour is observed when mode 4 is excited, where increased viscosity of the surrounding fluid correlates

with stronger coupling, persisting far longer than the oscillations of the excited mode. The damping rates of these two modes vary significantly (as discussed in Section 3.4.2), with higher modes experiencing faster damping than lower modes. This variation explains the aforementioned phenomena, where the coupling and persistence of modes are affected by viscosity and the initial conditions of the flow.

To study the influence of the magnitude of the excited mode in the coupling Figure 3.15 shows the maximum percentage of modes different from that excited for drops initialized with modes $m = 2, 3, 4$ for different initial deformations considering an $Oh = 0.1$ for the three studied cases.

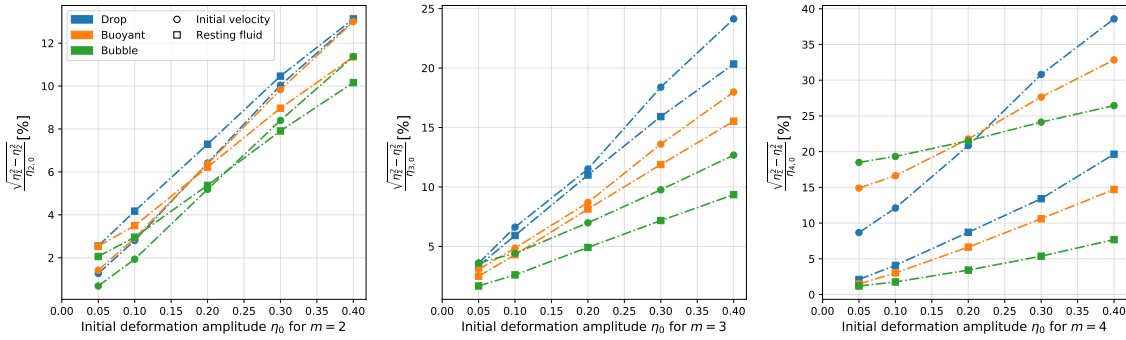


Figure 3.15: Presence of other modes different from the excited one in percentage for modes $m = 2, 3, 4$ for the droplet, buoyant, and bubble case for varying initial deformation amplitude and $Oh = 0.1$.

The three highlighted modes exhibit different behaviours but share a common trend: a linear increase in coupling with other modes as initial deformation increases, with the smallest percentage observed for an initial deformation of $\eta_0 = 0.05$. For oscillations driven by the exciting mode $m = 2$, the presence of other modes is somewhat reduced when using the linear velocity field at $t = 0$ for smaller η_0 . However, as η_0 increases, coupling grows rapidly and eventually exceeds that observed with the stagnant velocity field.

In contrast, oscillations involving modes $m = 3$ and $m = 4$ display different behaviour. The coupling with modes other than the excited one is equal to or greater when the theoretical linear velocity field is used for all η_0 values studied. When only deformation is introduced, the coupling between modes decreases with increasing dynamic effects of the surrounding fluid. This is due to the faster damping of oscillations in higher modes caused by the increasing viscosity of the continuous phase.

Given the scope of the simulations, a comprehensive study on the influence of the Ohnesorge number on mode coupling has not been conducted. Nonetheless, Figure 3.16 illustrates the relationship between coupling and Oh for $\eta_0 = 0.1$ with drops initialized using a zero velocity field. These results confirm that, as noted by Smith (2010), viscosity influences coupling. A higher Ohnesorge number (viscous forces relative to inertial and

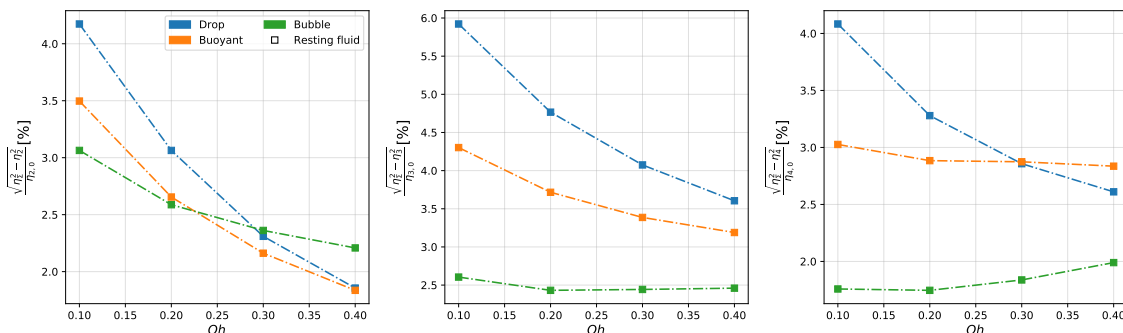


Figure 3.16: Presence of other modes different to the excited one in percentage for modes $m = 2, 3, 4$ for the droplet, buoyant and bubble case for: varying initial deformation amplitude for varying Oh and $\eta_0 = 0.1$.

surface tension forces) leads to fewer modes other than the excited one being present. This is linked to the faster damping effect in higher viscosity systems, which prevents significant excitation of lower or higher modes.

As a test case, a droplet initialized with axisymmetric initial deformation amplitude $\eta_0 = 0.01$ and $\eta_0 = 0.1$ for modes $m = 2, 3$ and 4 simultaneously is studied and compared against single-mode deformation oscillations of the same individual m and $l = 0$. (Figure 3.17) for the denominated drop case ($\rho_r = \mu_r = 1 \times 10^{-3}$). The oscillations of each mode are isolated and tracked over time with the aid of the spherical harmonic decomposition framework presented in subsection 2.3.1. It is observed for the amplitude $\eta_0 = 0.01$ (Figure 3.17 (top)) that the different oscillation modes appear to not interact with each other, following the linear theory in frequency and damping. This is not the case when the amplitude is increased to $\eta_0 = 0.1$. The oscillations of the present modes are affected by the presence of the other modes. These results further cement the previous statement that the coupling between modes, as a non-linear effect, depends on the amplitude of the deformation.

In order to account for more complex geometries that can more accurately represent realistic droplets (as the ones studied in chapter 4), a similar test case to that presented previously is considered, but this time with the initial conditions set up to include non-axisymmetric deformations. This is achieved by introducing perturbations in terms of spherical harmonics 2.3.1. In the presented test case, a droplet initialized with perturbations of amplitudes of $\eta_0 = 0.1$ for spherical harmonic functions Y_2^0 , Y_3^1 and Y_4^3 (see figure 2.4) can be seen in figure 3.18.

3.5.2 High amplitude deformations

In order to have a reference for the case studied in chapter 4, a series of simulations without turbulence are performed with similar conditions and numerical resolution as for

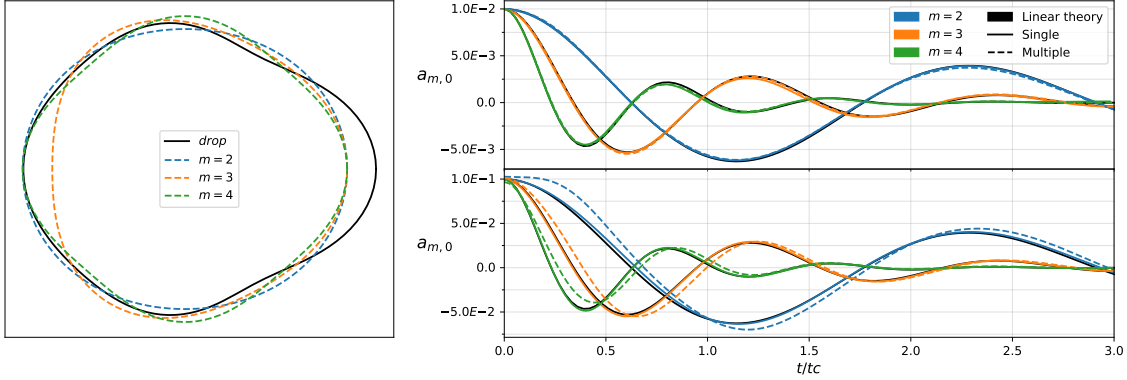


Figure 3.17: Left: Representation of droplet initialized with modes $m = 2, 3$ and 4 simultaneously (black line) and its equivalent single modes (dashed coloured lines) for an initial amplitude of $\eta_0 = 0.1$. Right: Oscillations of a droplet initialized with axisymmetric initial deformation amplitude $\eta_0 = 0.01$ (top) and $\eta_0 = 0.1$ (bottom) for modes $m = 2, 3$ and 4 simultaneously compared against single-mode deformation oscillations for the same m .

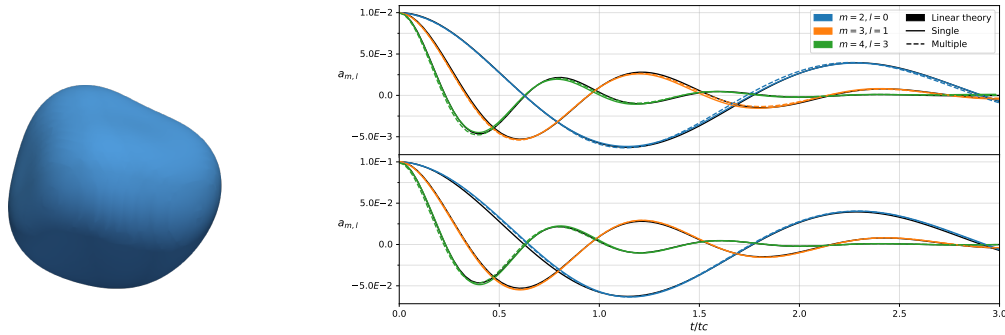


Figure 3.18: Left: Representation of droplet initialized with modes $m = 2, 3$ and 4 simultaneously in different. Right: Oscillations of a droplet initialized with non-axisymmetric initial deformation amplitude $\eta_0 = 0.01$ (top) and $\eta_0 = 0.1$ (bottom) for modes $m = 2, 3$ and 4 and orders $l = 0, 1, 3$ respectively, compared against single-mode deformation oscillations for the same m and the corresponding linear theory.

the turbulent case. The selected configuration is to investigate the oscillations of each isolated mode in a fluid initially at rest. Both the drop and the surrounding fluid are of equivalent physical characteristics (i.e. μ_r, ρ_r) as those used for the generation of the database.

Each simulation corresponds to the amplitude perturbation of modes $m = 2 - 6$. The spherical harmonic coefficients $a_{m,0}$ were chosen in accordance to the highest amplitude of the coefficients found in turbulent flow deformation (presented later in section 4.3).

The reference frame was selected so that we would follow the axisymmetric oscillations of the liquid drop (i.e. θ is the angle respecting to the axisymmetric axis.). The temporal evolution of the coefficients, as well as their initial shape, are given in figure 3.19.

In the simulation common results are observed. First the oscillatory behaviour is clearly seen. The amplitude reduces in time as expected by the theory. Second, it is noticeable that the droplet tends to spend more time in the prolate state for mode 2 as a known non-linear effect (Trinh & Wang 1982). This can be seen comparing the time spent on positive (i.e. prolate) and negative (i.e. oblate) $a_{m,0}$ when considering even modes (i.e. 2, 4, 6). For mode 2 oscillations, it is computed that the droplet spends 56.75% of the total time in prolate state. This phenomenon has been analysed in detail in the works of Foote (1973), Basaran (1992), Meradji et al. (2001), Zrnić et al. (2022) and discussed in section 3.4.1. For modes 4 and 6, the oscillations appear to be more periodic, not having such a difference when comparing prolate to oblate state. Finally, even if only a pure mode is initially perturbed, a coupling between modes is observed. That is particularly seen for even modes (see figures 3.19a, 3.19c, 3.19e) as suggested by Foote (1973) and Alonso (1974). The coupling between orders seems negligible in all the cases, except order $l = 4$ that appears for modes $m = 4 - 6$. Indeed, this order is aligned with the Cartesian grid, and thus numerical approximations affect this order.

The frequency and damping of each simulation are given in table 3.1. The values of ω_m and β_m were computed by using a Levenberg-Marquardt fitting algorithm. The covariance of the fitted results was below 0.5% for all cases. As predicted by the theory, (Lamb 1881, Prosperetti 1977), these values increase with the degree. In other words, the deformations with smaller amplitude have larger frequency and are dissipated faster. The computed values differ from the theoretical predictions. This is due to different considerations. First, the selected mesh resolution has been chosen to fit the simulations of the numerical database of droplets in turbulence presented in section 4.2.1. Second, the droplet is not in an infinite domain, since the domain is considered as tri-periodic as in the database. Finally, the theory is done for small perturbations (i.e. $a_{m,l} \ll R_0$), assumption that is not verified in the current simulations.

Mode	2		3		4		5		6	
	ω	β								
Inviscid case	1.00	0.0106	1.890	0.0297	2.89	0.057	3.99	0.0933	5.19	0.138
Eq. 3.29	0.959	0.0441	1.81	0.0849	2.76	0.135	3.81	0.195	4.95	0.264
Individual mode (figure. 3.19)	0.738	0.0841	1.861	0.214	2.544	0.288	3.70	0.374	4.79	0.440

Table 3.1: Summary of frequencies ω and damping ratio β normalized by ω_{20} .

3.6 Conclusion

This chapter provides the mathematical development of the linear shape oscillations of a Newtonian droplet or bubble immersed in a Newtonian surrounding fluid and extends

the existing literature by providing the equations to solve the general case. This has been accompanied by a direct numerical simulation of the studied case considering different Ohnesorge numbers as well as different density and viscosity ratios (ρ_r, μ_r).

The analytical solution of the dispersion relation is obtained and validated against the existing literature on the limiting cases of drops and bubbles. DNS of droplets with different Ohnesorge numbers and density/viscosity ratios are performed and validated against the developed linear theory. It is shown that the linear theory is good at predicting the evolution of the excited mode when considering small amplitude deformations ($\eta_0 < 0.4$), with good agreement with both initialization methods. It is also shown that the use of the initial velocity field obtained by the linear theory is of great importance in the analysis of the coupling between the different deformation modes since the results differ not only in amplitude but also in frequency.

The use of direct numerical simulation to analyse the present problem allows us to evaluate the energy in the system and compare it with the linear theory. The results show the expected damping influence of the surrounding fluid, as well as the increasing damping rate with increasing mode m and initial deformation η_0 . For the cases in which the surrounding fluid has strong dynamic effects, the simulations need to be improved, as the kinetic energy of the ambient fluid is not fully captured.

When considering the effects of the viscosity present in both the continuous and dispersed phase and the high-amplitude deformation observed for droplets in turbulence (see chapter 4), non-linear behaviour of the drop oscillations is expected. Hence, in section 3.5 the coupling between modes as a non-linear effect is studied, with the biggest takeaways that: when considering small amplitude deformations ($\eta_0 \geq 0.05$), isolating the oscillatory motion of each present mode shows that the individual modes are in agreement with the linear theory. When the modes are aligned (same axis of symmetry), increasing their initial amplitudes promotes the coupling between them. When they are not aligned (different axes of symmetry), even when increasing the initial amplitude of each mode will result in each one acting independently and in agreement with the linear theory.

Even though the results obtained show the capacity of the linear theory, this work could be improved by further developing the analytical work and determining the non-linear flow characteristics akin to the works of Zrnić et al. (2022), Smuda et al. (2024). Nonetheless, the results present in this chapter serve as groundwork for the analysis of the deformation and oscillations of droplets in turbulence explored in chapter 4.

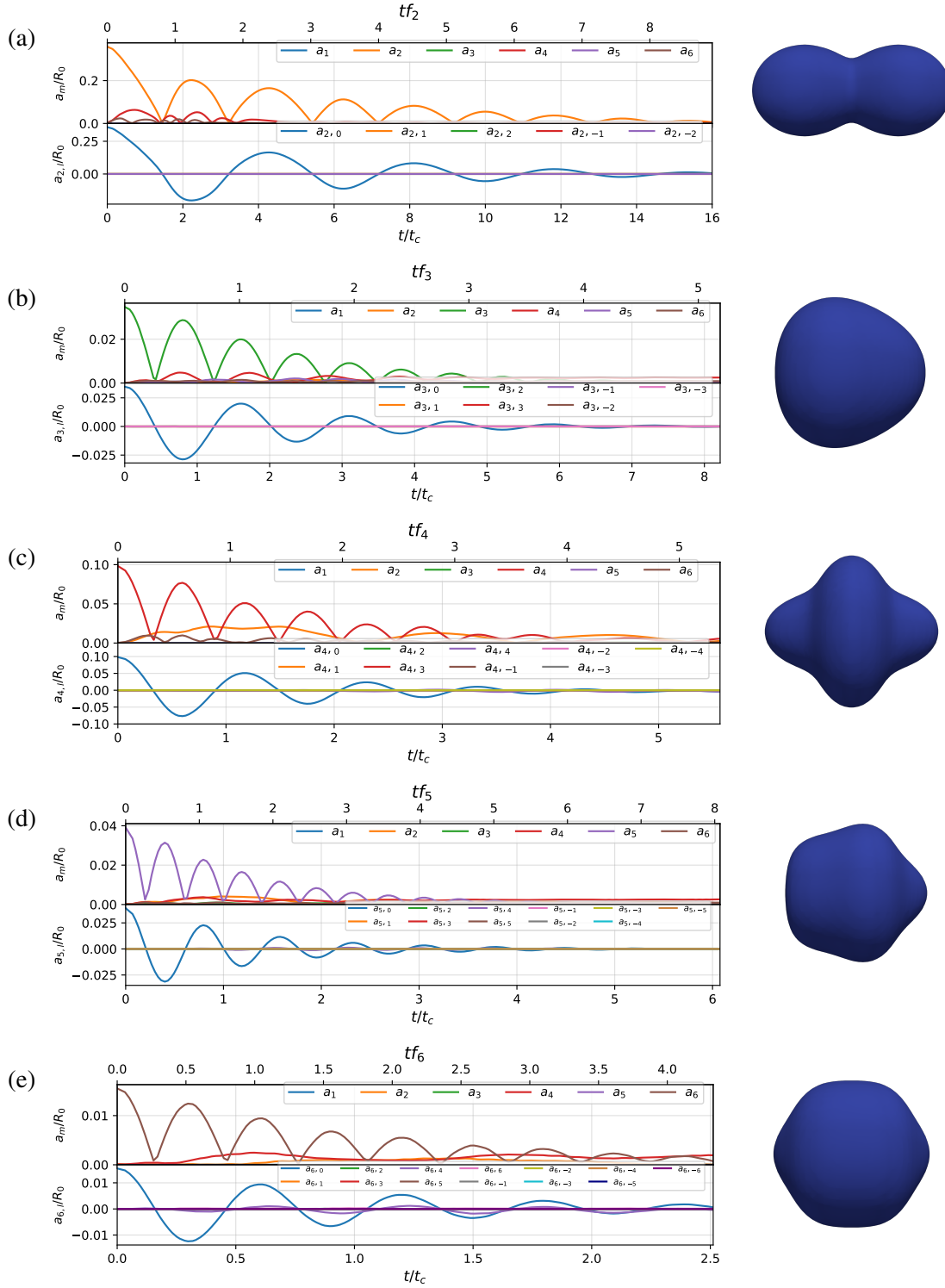


Figure 3.19: On the left: Oscillations of a droplet initialized with a spherical harmonic mode coefficient $m=2-6$. (a) $a_{2,0} = 0.36R_0$ (b) $a_{3,0} = 0.035R_0$ (c) $a_{4,0} = 0.1R_0$ (d) $a_{5,0} = 0.04R_0$ (e) $a_{6,0} = 0.016R_0$. On the right: Droplet shape at $t = 0$.

Chapter 4

Droplets in turbulence

4.1 Introduction

Droplet deformation and breakup are critical phenomena in the atomization process due to their impact on the final droplet size distribution. The deformation dynamics and potential breakup of a droplet primarily depend on the surrounding fluid's ability to deform the droplet in opposition to surface tension forces.

In turbulence, the range of eddy sizes is characterized by different turbulent scales. The largest eddies correspond to the integral length scale, where energy is injected into the system. As energy cascades down to smaller scales, it reaches the Kolmogorov scale, where viscous forces dominate and dissipate energy as heat. The interaction between droplets and turbulence can thus be influenced by these scales, affecting the droplet breakup dynamics (Kolmogorov 1941). The Kolmogorov-Hinze theory provides a framework for understanding the breakup of droplets in turbulent flows. It suggests that breakup occurs when the turbulent stresses at the Kolmogorov scale exceed the cohesive forces of surface tension.

A common assumption in various models is the existence of a critical Weber number (the ratio between turbulent and surface tension forces) for breakup. However, this criterion is not universally applicable, as it does not apply to cases where the residence time of the drop is significantly longer than the period of its shape oscillations (Risso 2000). Many researchers have attributed droplet breakup in turbulence to their free oscillations, particularly at low turbulence levels, as a result of a resonant mechanism. This has been evidenced by studies such as those conducted by Sevik & Park (1973), Risso & Fabre (1998), Lalanne et al. (2019).

Direct numerical simulation (DNS) has been extensively used to study droplet/bubble-turbulence interactions, from seminal works to more recent studies (Qian et al. 2006, Perlekar et al. 2012, Perrard et al. 2021, Vela-Martín & Avila 2022). Different numerical approaches have been employed, such as Volume of Fluid (VoF), Levelset, coupled Levelset and Volume of Fluid (CLSVOF), and Lattice-Boltzmann methods (Kékesi et al.

2014, Perrard et al. 2021, Trontin et al. 2010, Shao et al. 2018, Duret et al. 2018, Perlekar et al. 2012, Montessori et al. 2021).

Following the study of Newtonian drops' oscillations in a Newtonian surrounding fluid depicted in the previous chapter, we aim to generalize the classical linear theory to account for more complex geometries that better represent realistic droplets by introducing spherical harmonics, thus tracing oscillations in both azimuthal and polar directions.

This study is motivated by previous literature using spherical harmonic decomposition to describe deformed surfaces. The study of a liquid globe oscillating in a resting fluid introduced mode oscillation studies (Chandrasekhar 1959, Miller & Scriven 1968). Later, damping isolating the spherical harmonic coefficient for mode 2 was investigated, and the signature of deformation modes to infer bubble dynamics in turbulent flow was presented (Prosperetti 1980*a*, Risso & Fabre 1998). The development of a similar framework to describe bubble deformation has also motivated this work (Perrard et al. 2021).

The utility of the present framework comes from its ability to isolate each mode and describe the droplet's oscillation frequency as an ensemble of the different mode frequencies since we can monitor oscillations in all directions. This framework is applied to a series of independent droplets immersed in a turbulent background flow generated by direct numerical simulation of the Navier-Stokes equations. The in-house code Archer is chosen for its capability to reproduce Lamb theory oscillations and its level-set implicit description that allows accurate computation of spherical harmonic coefficients (Aniszewski et al. 2014, Cordesse et al. 2020).

In the following work, carrier and dispersed phases with similar density and viscosity are considered, representing a specific case between droplets and bubbles. No mass exchange or mixing between the fluids is considered. Additionally, DNS of individual deformation modes in a fluid initially at rest, with amplitudes comparable to turbulent mode oscillations, has been performed to compare their frequencies with those obtained from studies under turbulence effects. The results show good agreement with both experimental and numerical literature, particularly exhibiting mode 2 deformation dominance throughout the droplet lifetime and strong coupling between even modes (i.e., 2, 4, 6). The study confirms that the oscillator is driven by capillary forces through the decay following high-amplitude deformations in both turbulent and quiescent flows.

The contents presented in this chapter have been published in the context of this PhD work (Roa et al. 2023b).

4.2 Droplet database

4.2.1 Generation of the database

The methodology employed to generate droplet breakup under turbulent flow was initially presented in Chen et al. (2019) and Chéron et al. (2019). Here, the methodology is used to

create a database of droplets evolving under turbulent conditions. This database is created by performing multiple realizations of the same physical configuration, with the viscous and density ratios, as well as the turbulent Reynolds and Weber numbers, kept constant. The overall procedure is illustrated in figure 4.1. Each realization involves three steps:

1. **Generation of Turbulent Background:** A single-phase turbulent flow is generated and sustained in a tri-periodic domain by continuously forcing the energy to a desired level using the linear forcing method described by Rosales & Meneveau (2005). This method has been utilized in our research group for a decade (Duret et al. 2012, Martinez et al. 2023). The turbulent flow is maintained for several eddy-turnover times to develop a fully developed, homogeneous, isotropic turbulence.
2. **Introduction of Solid Particle:** A fixed solid spherical particle is introduced into the computational domain. The no-slip velocity condition on the particle's surface is enforced using the immersed boundary method (Chéron 2020).
3. **Replacement with a Droplet:** Once the turbulent flow is statistically steady and the no-slip boundary condition is accurately enforced, the solid particle is replaced by a freely moving spherical droplet of the same radius, following the methodology described by Chéron et al. (2023) and Deberne et al. (2024).

The simulations continue until droplet breakup is detected. Long simulation durations are feasible because there is no mass loss, allowing for multiple realizations at a limited numerical cost.

The simulation timeline includes the following details: every five eddy-turnover times, the single-phase velocity and pressure fields are recorded (step 1). For each single-phase snapshot, nine different simulations are conducted, each with the solid particle fixed at a different position within the computational domain. Every half eddy-turnover time, the flow field is saved (step 2). A two-phase flow simulation is then initiated for each snapshot from step 2, with the two-phase flow data saved 25 times per eddy-turnover time (step 3).

This approach ensures that the initial turbulent condition does not disturb the droplet's surface. The impact of this methodology for initializing flow conditions compared to a setup where the droplet is instantly introduced into a turbulent flow (Crialesi-Esposito et al. 2023, Vela-Martín & Avila 2022, Håkansson et al. 2022b, Håkansson & Brandt 2022a), on the droplet shape's temporal evolution can be seen in detail in Deberne et al. (2024). The chosen strategy to initialize DNS of single droplets in turbulent flow influences the initial growth of shape deformation, avoiding the initial surface corrugations noted by Crialesi-Esposito et al. (2023) and Komrakova et al. (2015). For bubbles, the velocity can be set to zero inside the bubble (Riviere et al. 2021, Perrard et al. 2021); however, this approach is unsuitable for this study due to the non-negligible volume fraction and density of the disperse phase. Out of 260 breakup events, 68 cases were excluded due to degeneration, resulting in a database of 192 realizations.

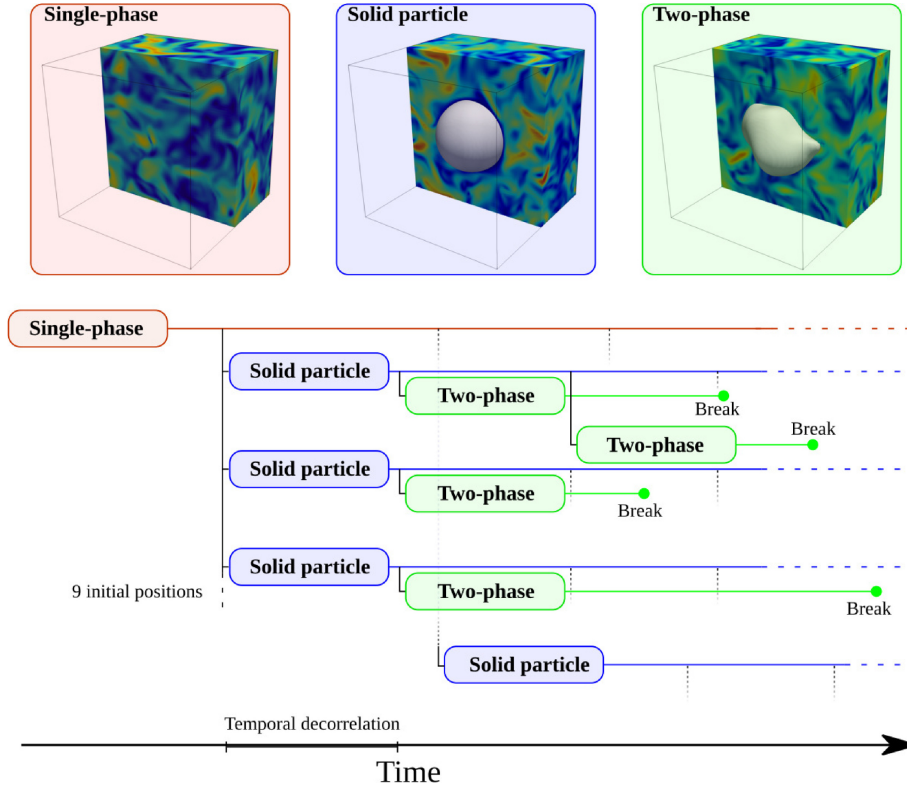


Figure 4.1: Droplet database numerical procedure (Source: Deberne et al. (2024)).

This database, or portions of it, has been used in previous studies on the transformation criteria for Lagrangian–Eulerian hybrid methods Chéron et al. (2019), the investigation of 2D projection on shape parameters Chéron et al. (2022), and the analysis of droplet oscillations Roa et al. (2023a). A complete analysis of the generated database can be found in the work of Deberne et al. (2024).

4.2.2 Physical and numerical parameters

The numerical simulation was performed over a 64^3 grid, providing a sufficient resolution to capture the interactions between the droplets and the surrounding turbulent flow. A ratio between the droplet radius R_0 and domain size L of $R_0/L = 0.233$. The droplet diameter is fixed at $D = 30\delta x$, where δx represents the Eulerian fluid mesh size, as determined from a previous study Chéron et al. (2019). This configuration is chosen with the aim of carrying out numerous realizations in order to generate a large database. However, this numerical setup can produce non-isolated droplets that can interact with each other across the periodic domain. A total of 68 such cases were identified and subsequently removed from the database, as mentioned previously. A second drawback of the confined domain is that the turbulence does not fully develop (see figure 4.2). The size of the computational

domain must be sufficiently large to capture all relevant turbulent scales. If the domain is too small, it might still impose artificial constraints on the turbulence development. This leads to another limitation: a finer Eulerian fluid mesh is required to effectively distinguish between the Kolmogorov and integral length scales (Pope 2001, Equation 9.7). Given the limited domain size and resolution of the droplets of the database leads to such differences from the Kolmogorov theory.

The study specifically considered liquid-liquid interactions without any mixing or mass exchange between the two liquids. This assumption simplifies the analysis by focusing solely on the dynamic interactions and behaviours of the droplets within the turbulent flow. The Weber number, defined as $We = \frac{\rho_1 u'^2 2R_0}{\sigma}$ remained constant across all droplets from the database ($We = 0.9$). Here, the Weber number is proportional to the square of the ratio between the capillary time $t_c = \sqrt{\rho_1 R_0^3 / \sigma}$, and the turbulent time ($t_t = \frac{2R_0}{u'}$). For this choice of Weber number, it is possible to determine the maximum droplet diameter that does not undergo breakup by calculating the Hinze scale ($D_H = 0.725(\rho_2/\sigma)^{-3/5} \epsilon^{-2/5}$) (Hinze 1955, Perlekar et al. 2012), which is equal to $D_H = 1.2R_0$. When the Weber number is below the critical value, simulations take too long to reach droplet breakup. On the other hand, when the Weber number is above the critical level, the droplets break during the initial deformation stage (Vela-Martín and Avila, 2022). However, at the chosen surface tension, the turbulent and capillary timescales are of the same order of magnitude. The balance between inertial forces and surface tension forces is ensured to remain the same in each simulation, making it difficult to distinguish between interfacial and turbulence-driven phenomena. This allows for a more straightforward comparison of how droplets behave in different turbulent conditions without varying the fundamental physical forces acting on them. The breakup times of these droplets vary in the range between $t_{break} = 9.09t_c$ and $t_{break} = 376t_c$.

The viscosity ratio (μ_1/μ_2) and the density ratio (ρ_1/ρ_2) are both set to 1. This decision was made to isolate and focus on the interactions between the fluid interface and the surrounding turbulence without the additional complexities introduced by differing fluid properties. When the density and viscosity are matched, it simplifies the computational model and allows for a clearer understanding of how turbulence interacts with and influences the behaviour of the interface (Perlekar et al. 2012). Furthermore, the turbulence forcing can introduce additional challenges, especially when the density ratio between the phases is significant (Shao et al. 2018). By setting both the viscosity and density ratios to unity, we eliminate these complications and ensure that the effects observed are primarily due to the turbulence-interface interactions, rather than disparities in fluid properties. In order to directly compare the results presented in this section with the ones present in 3, the Ohnesorge number, obtained from the previously mentioned physical parameters, is $Oh = 0.00465$. This parameter choice is crucial for accurately capturing the breakup behaviour of the droplets and understanding the underlying physics driving the process. To sustain the turbulent flow in a physical space-based code, a linear forcing has been applied. While the flow is statistically stationary and equivalent across various resolu-

tions, each realization exhibits unique differences due to the inherent chaotic nature of the flow and the applied forcing. The linear forcing consist in introducing a volume force in the Navier-Stokes equation (2.2) proportional to the velocity fluctuations, expressed as $\vec{f} = A\vec{u}'$. Here, $\vec{u}' = \vec{u} - \langle \vec{u} \rangle$ is computed at the end of the prediction step and the parameter A is updated each time step in order to obtain a target total energy level. Due to limitations in computational resources, the present simulations are conducted at a fixed turbulent Reynolds number, $Re_\lambda = \frac{\rho_l u' \lambda}{\mu_l} \simeq 45$, where λ is the Taylor length scale ($\lambda = \sqrt{\frac{15\mu_l u'^2}{\rho_l \epsilon}}$) and ϵ is the average dissipation rate. The impact of the forcing scheme is currently under study (Aniszewski & Brändle de Motta 2022) and will be presented in a future communication. Different forcing methods are also planned to expand on the current understanding of the turbulent forcing in the drop deformation and breakup dynamics.

In a homogeneous and isotropic turbulent flow, the velocity fluctuations at the droplet scale can be related to the mean dissipation rate of energy, ϵ (Kolmogorov 1941) in the inertial range. Figure 4.2 displays the velocity fluctuations (the mean-square velocity increment) $\langle \delta u^2(d) \rangle$ as a function of distance d from one of the single-phase simulations. This computation is done using the in-house post-processing tool PyArcher. More specifically using an updated version of the subroutine presented in the work of Thiesset et al. (2020). The Kolmogorov theory's prediction for this quantity in the inertial sub-range ($C(\epsilon d)^{2/3}$) is also presented, with C a constant in the range $C \in [2, 2.2]$ (Pope 2001). In the present work the value of the constant $C = 2$, following the work of Risso & Fabre (1998). A significant difference between the Kolmogorov theory and the computed values is evident, particularly for smaller values of the separation, d . This difference suggests that the energy spectrum in the simulations declines more rapidly than in the inertial sub-range of high Reynolds number turbulence, indicating a faster energy dissipation rate in the simulated turbulence.

4.2.3 Decomposition of droplets immersed in a turbulent background flow

The spherical harmonic coefficients are dependent on the reference frame of the system. This means that the results from the expansion are directly affected by the centre of the coordinate system and the reference frame in which we define the angles θ and φ . Due to the dynamic nature of the surrounding fluid in this study, the droplet is expected to undergo both translation and rotation, rather than remaining static. To address this, we have adopted an origin at the centre of mass of the droplet as our reference point, with a coordinate frame aligned to the Cartesian mesh, except for the specific analyses conducted in a section 4.4. This approach ensures that our reference frame is appropriately positioned to capture the droplet's motion and deformation accurately, providing a consistent basis for the analysis.

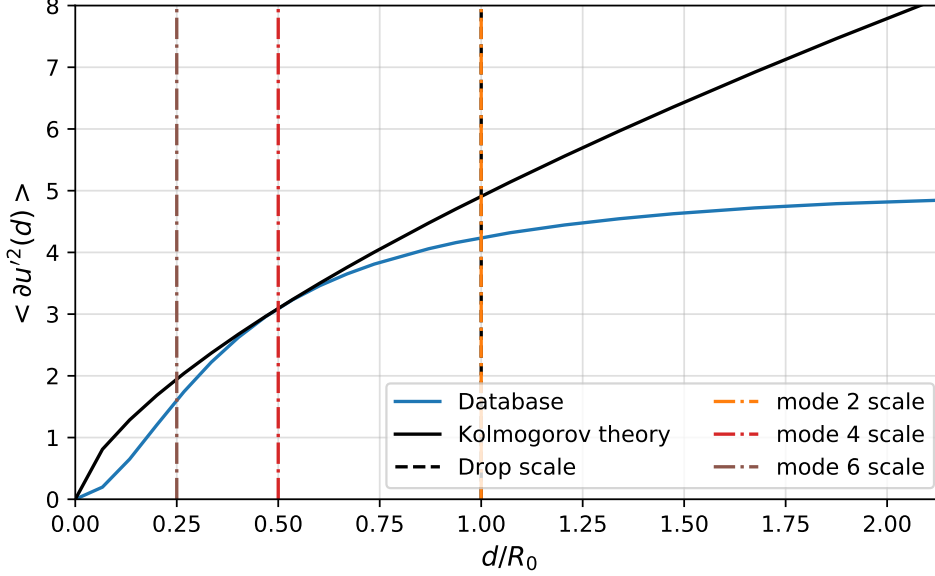


Figure 4.2: Predictions of the Kolmogorov theory for $\langle \delta u^2(d) \rangle$ compared with the computed values of a single droplet of the database.

In the implemented approach, the numerical error associated with computing the radius $R(\theta, \varphi)$ is rigorously controlled, with a maximum error of less than 0.1%. Similarly, for computing the coefficients $a_{m,l}$, the numerical error is kept below 0.2% for $m \leq 6$. These error tolerances ensure the accuracy and reliability of the spherical harmonic expansion framework utilized in this study. A detailed overview of the spherical harmonic expansion framework applied here has been done as part of this research (Roa et al. 2023a) and presented in section 2.3.2.

In the studied case, the computation of spherical harmonic modes is limited to $m \leq 6$, as we observe a rapid decrease of the amplitude of the coefficient $a_{m,l}$ with increasing m . Since we aim to use this framework to characterize the deformation on the droplet surface we are interested in reducing as much as possible the effect of mode 1 ($a_{1,l} \approx 0$), which primarily describes the translatory motion of the droplet. To ensure robust characterization of surface deformations, the centre of mass was chosen as the reference point in space after evaluating various approaches (Roa et al. 2023a). For the results shown here, 90% of the computed mode 1 coefficients are below 0.05, indicating a predominantly negligible influence of translational motion on the overall droplet deformation. It is important to note that exceptions to this observation may arise under conditions of high-amplitude deformation experienced by the droplet.

4.3 Oscillations of droplets immersed in a turbulent flow

We investigate the oscillations by computing the coefficients $a_{m,l}$ for each droplet of the database in order to correlate their oscillations with deformation. Since the frequency of each coefficient $a_{m,l}$ for the same m are homologous, we make use of the power spectrum coefficient a_m^2 (Eq. 2.14), which corresponds to the surface energy contained in each mode m (Perrard et al. 2021). The evolution of $a_m = \sqrt{a_m^2}$ as a function of the dimensionless time tf_2 for a single droplet is shown in figures 4.3 and 4.4, with f_2 the natural frequency of mode 2. For the studied cases presented in this work $1/f_2 = 3t_c$, obtained from equation 3.29. The choice of plotting a_m instead of a_m^2 is done to highlight the coupling between modes. Figure 4.3 shows the total deformation ζ_Ω as a function of time, alongside the amplitude of the mode 2 oscillations a_2 , both normalized by the initial radius for a single droplet from the numerical database. We can observe a dominance of mode $m = 2$ in the surface energy deformation. The strong correlation between the two curves supports the literature’s assertion that mode 2 plays a crucial role in the deformation dynamics of bubbles (Risso & Fabre 1998, Ravelet et al. 2011, Perrard et al. 2021). The total deformation ζ_Ω tends to have slightly higher peaks than the mode 2 amplitude (a_2). This difference can be attributed to contributions from higher-order modes or other dynamic effects not captured solely by mode 2.

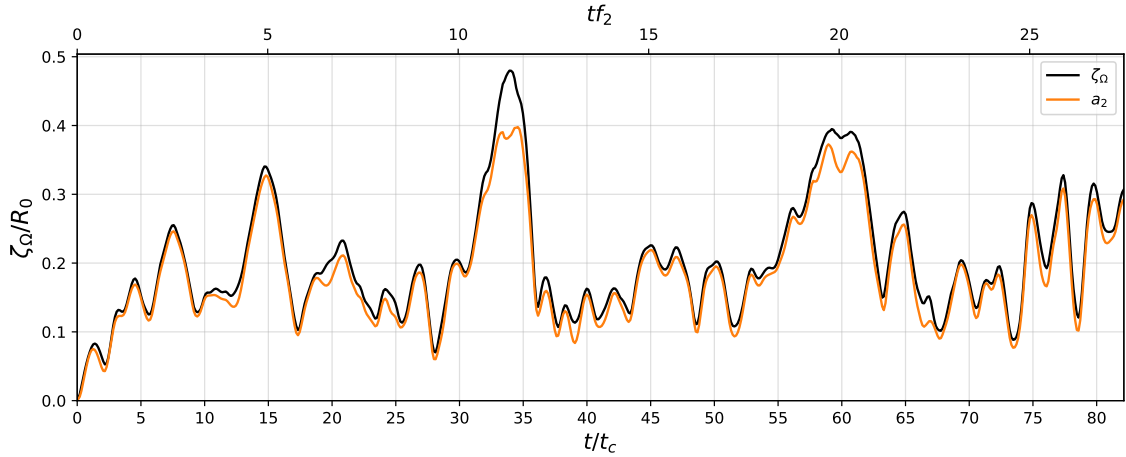


Figure 4.3: Total deformation ζ_Ω as a function of time, together with the amplitude of the mode 2 oscillations a_2 .

In practice, a sum over the first six modes ($m = 2, 3, 4, 5, 6$) can estimate the amplitude deformation ζ_Ω with less than 0.5% error (refer to figure 2.6). This finding confirms the predominance of the first few modes of oscillation and validates the spherical harmonic decomposition approach. By accurately capturing the deformation dynamics with only a limited number of modes, this method effectively demonstrates that higher-order modes contribute minimally to the overall deformation when ζ_Ω remains within the specified

range. This approach not only simplifies the analysis but also underscores the significant role of the primary modes in describing the deformation behaviour of droplets. Figure 4.3 shows the temporal evolution of a_m for the first few spherical harmonics $m \in [1, 6]$ for a single run of the numerical database. The amplitude of the coefficient a_1 is close to zero for most of the duration of the droplet's run due to the choice of the centre of the reference frame, except when we observe high amplitude deformations (e.g. $t/t_c = 11.35$). In these extreme cases, the droplet becomes highly elongated with a complex geometry. To a lesser extent, the mode $m = 4$ also contributes to the global deformation and seems to be coupled with the mode $m = 2$ deformations. Considering the first peak at $tf_2 = 5$, the total amount of energy stored at mode $m = 2$ is equivalent to 10% of the surface energy of a perfect sphere, while the same quantity for mode $m = 4$ does not reach 0.5%. The coefficients $a_{2,l}$ are also shown in figure 4.4. The coefficients $a_{m,l}$ are directly dependent on the reference frame. If a different initial reference frame had been chosen, different values for the coefficients $a_{m,l}$ would have been observed. However, a clear oscillation pattern is observed for each mode, and it is worth noting that the amplitude of all the exposed coefficients are akin. The same behaviour can be observed in the other modes, but with smaller amplitudes.

Due to the difficulty to extract a pure frequency from the amplitude coefficients $a_{m,l}$, the angular frequency of each couple (m, l) was obtained by computing the average oscillation period defined as the peak-to-peak interval time. The statistics were computed for $tf_2 > 6$, where the statistically converged regime is reached (see section 4.3.1). The frequency observed for each mode is of the same order of magnitude as one for pure-deformed oscillations. This result broadens the conclusions of Risso & Fabre (1998), which shows for bubble in turbulence experiments that the power spectrum of the projected area is dominated by the natural frequencies of modes 2 and 4. These two frequencies appear here for the coefficient corresponding to modes 2 and 4 respectively. This proves that, as expected, the oscillatory frequency is related to the shape deformation given by the same mode. In addition, our results show that all the modes are concerned by these natural oscillations, not only even modes.

The shift between the computed frequency and the natural one is not clear: for mode 2 we observe an increase in the frequency while for mode 6 we observe a decrease. The origin of these differences is difficult to identify here, but it could be due to the coupling of the interface with the turbulence and the coupling between modes. The seminal work of Kang & Leal (1988) on bubbles provides an initial insight into this problem. Nevertheless, the extension of this theoretical analysis to the liquid-liquid case is out of the scope of this work. Another way to understand the differences in frequency shifts between modes is to consider the characteristic length scales associated with each mode. Mode 2 has a characteristic length scale close to the radius of the droplet, which in our case, is similar to the inertial length scale. In contrast, mode 6 has a smaller characteristic length scale, closer to the Kolmogorov length scale. This can be seen in figure 4.2. As a result, the level of turbulence experienced and captured by each mode is different.

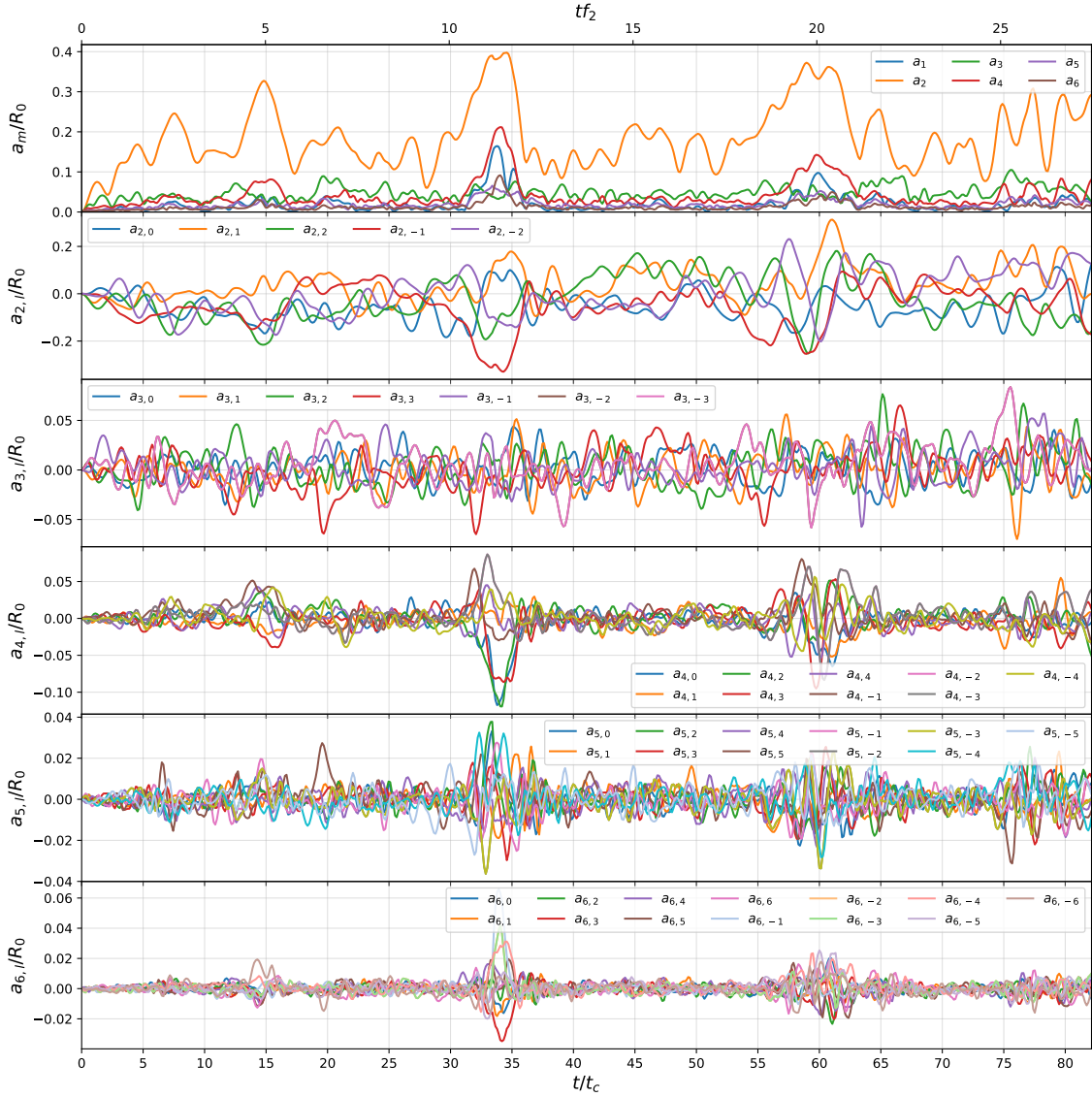


Figure 4.4: Top image shows the Power spectrum of the spherical harmonic decomposition for modes $m = 1$ to $m = 6$ as a function of the dimensionless time t/t_c of the same droplet as figure 4.3. Below, the oscillations of coefficients $a_{m,l}$ as a function of the dimensionless time t/t_c of one droplet from the database for $l = -m$ to $l = m$ are shown.

To gain a deeper understanding of how turbulence impacts the frequency at each scale, future research should investigate the effects of varying turbulent Reynolds numbers and different droplet sizes. Such studies could provide valuable insights into the differential impact of turbulence on the frequency shifts observed in different modes.

4.3.1 Initial-growth and saturation regime

We compute the ensemble-average deformation by analysing the entirety of the droplet database. For each droplet we perform the spherical harmonic decomposition analysis described above to obtain the spectrum values. In figure 4.6, we show the temporal evolution of the spectrum of some realizations as a function of the dimensionless time tf_2 . The ensemble averages defined by $\alpha_m(t) = \sqrt{\langle a_m^2 \rangle_{\mathcal{N}}}$ are described by the black dashed lines. The definition here differs from the definition of Perrard et al. (2021) who computes the ensemble average as $\langle a_m \rangle_{\mathcal{N}}$. The choice to use $\alpha_m(t)$ is motivated by the consideration that the saturation level should be linked to the total surface area. It has been observed that both expressions provide similar behaviour except for mode 6 where the strong short deformations increase the averaged value with current definition. The computed values of $\langle a_m \rangle_{\mathcal{N}}$ are not presented in this work.

A closer examination of the initial period after the droplet is released to evolve in the background flow reveals an exponential growth for each mode. This growth differs from what is observed by Perrard et al. (2021) who noted a linear growth during the initial time of bubble evolution in a similar experiment as seen in figure 4.5. The difference can be attributed to the different initialization routine. In their case, the bubble is initialized with a turbulent flow, even at the interface, while in our experiment, the droplet velocity is zero and a no-slip condition is ensured (Deberne et al. 2024). This could also be due to the fact that their work is done in bubbles. Considering the high viscosity and density ratios in the bubble case, the negligible dynamic effects of the fluid in the bubble could play a role in the initial deformation regime.

For all the modes, we observe a first peak of the ensemble average, that seems to be well repeatable and certainly related to the initial condition. The time to reach this peak decreases with increasing mode number, indicating that higher modes react more quickly to the initial disturbances. Following the initial exponential growth, each mode reaches a saturation level after a certain period of time. The time required to reach this saturation level decreases with increasing mode number. This implies that higher modes, which correspond to smaller-scale deformations, equilibrate faster than lower modes. The faster stabilization of higher modes can be attributed to the more rapid dissipation of smaller-scale turbulence and interface instabilities.

The saturation level has been studied for modes 2-4 by Perrard et al. (2021) as seen in figure 4.5. In the present work we compute this value for modes 2-6. The saturation level here is the ensemble and time average over the 220 droplets and after $tf_2 > 6$. The obtained average, defined by $\alpha_{m,sat} = \sqrt{\langle a_m^2 R_0 \rangle_{\mathcal{N}, tf_2 > 6}}$ for $m = 2 - 6$ are presented in table 4.1.

It is worth noting that even considering different initialization routines and the different physical properties of the cases studied (different We , μ_r and ρ_r), the saturation levels for modes 2 and 3 are similar in amplitude, meaning that there is an intrinsic saturation energy for each mode of deformation, regardless of the physical parameters. As expected,

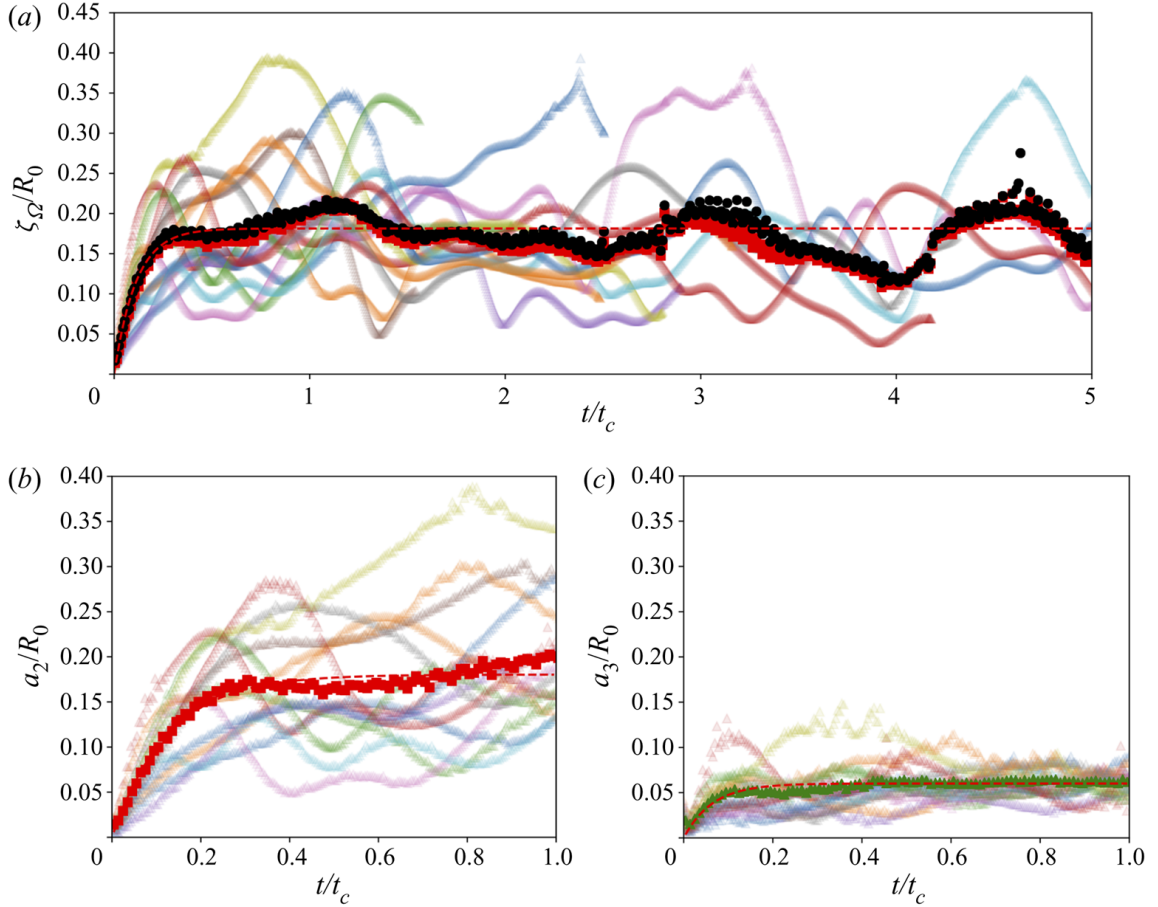


Figure 4.5: (a) Individual realizations of ζ_Ω at $We = 3$, as a function of the dimensionless time t/t_c in transparent colours. Ensemble average $\langle \zeta_\Omega \rangle$ of the surface deformation is superimposed (black full symbols), together with the ensemble-average mode 2 amplitude (red full symbol). (b) Coefficient a_2 as a function of dimensionless time t/t_c for $We = 3$ (individual realisations in transparent colours). Ensemble average $\langle a_2 \rangle$ is superimposed (full red symbol). (c) Coefficient a_3 as a function of dimensionless time t/t_c for $We = 3$ and the equivalent exponential fit (individual realisations are transparent colours and the green full triangle is ensemble average $\langle a_3 \rangle$). Source: Perrard et al. (2021).

Mode m	2	3	4	5	6
This work (Roa et al. 2023b)	0.2130	0.0531	0.0581	0.0260	0.0208
Perrard et al. (2021)	0.18	0.0604	-	-	-

Table 4.1: Saturation level as the ensemble and time average over the 220 droplets of the database.

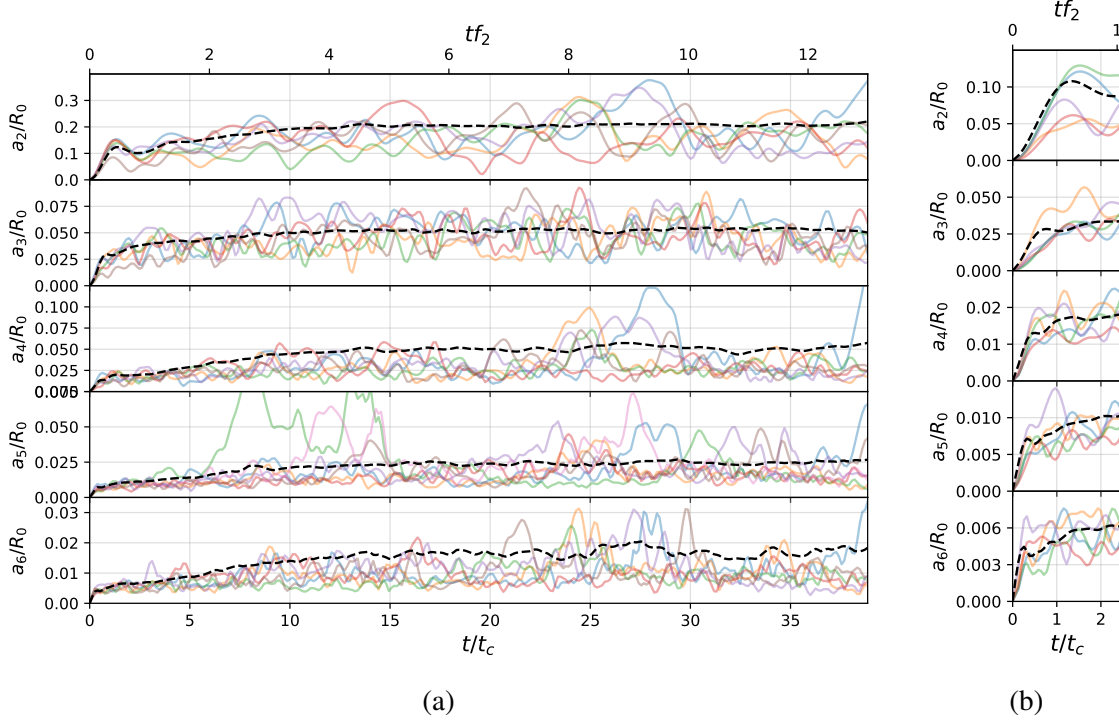


Figure 4.6: (a) Evolution of the deformation for each individual spherical harmonic mode coefficient a_m as a function of the dimensionless time t/t_c and tf_2 (individual realizations from the database in solid lines) with its respective ensemble average α_m (dashed line) for $We = 0.9$. (b) Close up of the initial growth regime.

the saturation level decreases as the mode increases. That is due to two main phenomena. First, the natural damping rate increases with the mode (3.33), and thus, the deformations related to large modes reduce faster. Secondly, as the mode increases, the characteristic length decreases, leading to a reduction in the turbulent energy captured by this mode (see figure 4.2). The interplay between these phenomena and the scaling of the saturation level remain unclear and warrant further investigation. In particular, the difference between odd and even modes should be established. Future work, with different Weber and turbulent Reynolds numbers will be really helpful in this direction. After the analysis of regular oscillations we consider now the study of large deformations.

4.4 Large deformations and damping factor

We have seen that droplet oscillations in a turbulent flow result in a series of non axisymmetric oscillations which are difficult to characterize with the linear-stability theory. Large deformation events can be relaxed or can lead to breakup as suggested by the model

presented in the works of Risso (2000), Lalanne et al. (2019) which provides a maximum deformation threshold. In the following, we analyse the oscillations following a high-amplitude deformation. In order to bring out axisymmetry as much as possible, we rotate the reference frame in which the spherical harmonics were computed to one that maximizes the amplitude of coefficient $a_{2,0}$. A minimization Broyden-Fletcher-Goldfarb-Shanno algorithm is used to find the two Euler angles that maximize $a_{2,0}$. The corresponding reference frame is often close to the inertial tensor of the droplet (see section 2.21 and (Lalanne 2012, Chapter 5)) that is here used as initial condition for the minimization algorithm.

As seen in figure 4.4, the studied droplets reach high-amplitude deformation several times during their lifetime. A total of 694 of these instances were chosen under the criteria that they have a coefficient $a_2(t_{peak}) > 0.3R_0$ and do not experience breakup within the $4t_{f_2}$ following this deformation event. The threshold criterion was chosen to be $1.5 \alpha_{2,sat}$, and is close to the breakup limit proposed by Lalanne et al. (2019), a threshold further substantiated in the current database (Deberne et al. 2024). In other words, these large deformations are often followed by breakup. Figure 4.7, illustrates the temporal evolution of the deformation coefficient $a_{m,0}$ following a high-amplitude deformation for individual droplet realizations, alongside the ensemble-average behaviour of the selected droplets.

Initially, the temporal evolution of coefficient $a_{2,0}$ offers insights into the overall deformation evolution. A rapid increase of the $a_{m,0}$ coefficients for $m = [2, 4]$ is followed by a contraction back to the previous mean level. In the case of mode 2 oscillations, when aligned with maximum deformation, the fluctuations between growth and decay exhibit a timescale related to f_2 . This decay phenomenon, akin to the observations of Ravelet et al. (2011), can be directly associated with the natural damping rate of the droplet.

The interplay between even modes becomes apparent upon further analysis. First, it is clearly seen that these high-deformation droplets have also an $a_{4,0}$ component. In other words, the orientation of modes 2 and 4 deformations are aligned. The alignment of the deformation between modes 4 and 2 has been verified by plotting the different orders. Furthermore, the increase in coefficient $a_{6,0}$ is noteworthy, indicating a potential energy recovery mechanism compensating for the relaxation observed in modes 2 and 4. For modes 3 and 5 there is no clear evolution.

In order to confirm that the physics after a high-amplitude deformation is related to the capillary forces and not to the background flow, 3 different realizations are studied. Three droplets are removed from the turbulent background flow at the moment of the highest deformation, similarly to the work done by Håkansson et al. (2022b) in the research for a breakup criterion. The first selected droplet is present in figure 4.7 (blue line), and its shape at $t - t_{peak}$ is shown in figure 4.8 (A). The same values are computed for two other droplets (B and C) of the database. These droplets were selected considering an increasing peak total deformation ($\zeta_\Omega = 0.39, 0.47$ and 0.52 respectively).

The reference frame is set as before using the maximization of $a_{2,0}$. In figure 4.9(a) the power spectrum evolution in time is given comparing the turbulent realization and the

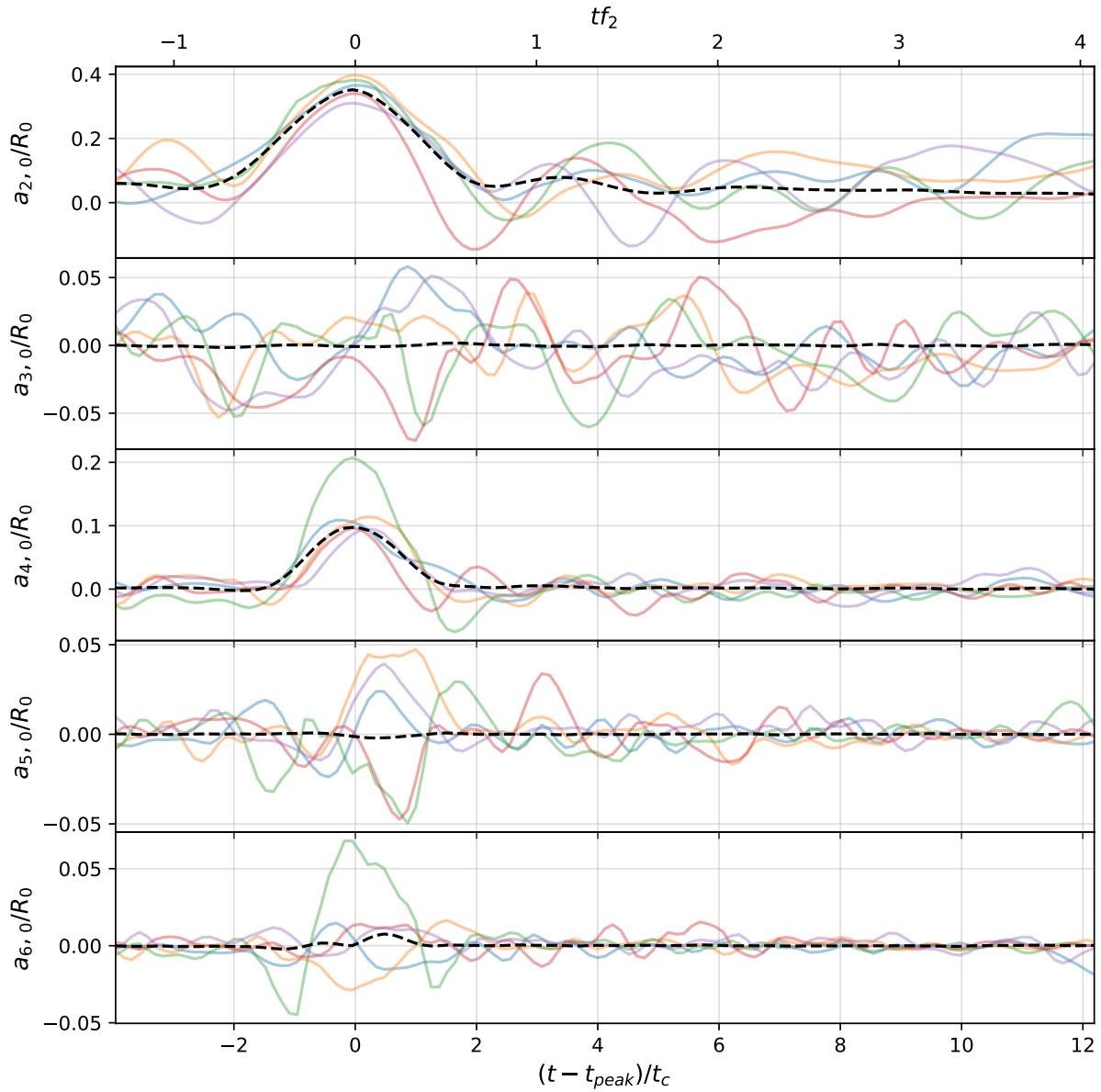


Figure 4.7: Evolution of the spherical harmonic coefficients $a_{m,0}$ following a high amplitude deformation $a_2 > 0.3$ (individual realizations from the database in solid lines) with its respective ensemble average $\langle a_{m,0} \rangle_{\mathcal{N}}$ (dashed line).

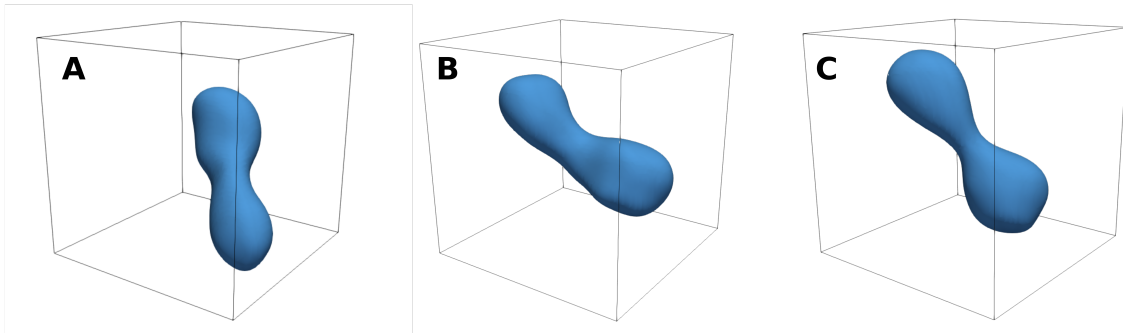


Figure 4.8: Snapshots of three droplet from the database from their maximum deformation state. The amplitudes of this peak are total deformation ($\zeta_{\Omega} = 0.39, 0.47$ and 0.52 respectively).

initial quiescent flow case. The initial decaying is clearly similar in both cases, then, for larger times, the turbulent case deviates from the perfect oscillator. In figures 4.9(b) and 4.9(c) the decomposition of modes 2 and 4 are given. The other modes are not given since their amplitude is negligible here. It can be observed that the increasing peak deformation of the droplets selected goes in hand with a clear formation of a neck (compare figures 4.8A to figure 4.8C). Nonetheless, a critical deformation state is not reached, which is proven by the fact that in the three observed cases the drop returns to a spherical state when removing the velocity field. Finally, the same conclusion can be drawn: the damping and first oscillations after experiencing a large deformation are driven by the capillary forces. This phenomenon can be observed in the three selected droplets.

The present droplet has a complex deformation and is not composed of an excitation of a single mode. Thus, the coupling between modes can explain the differences observed between Figs. 4.9(b)-4.9(c). The droplet, which is shown to undergo a high-amplitude mode 2 deformation, spends a slightly larger part of each period in prolate state (59.15% of the total time). This phenomenon is in accordance to the non-linear theory (Foote 1973, Zrnić et al. 2022) and observed in the results obtained for viscous drops in chapter 3. Due to the length of the first oscillation observed for mode 4 (figure 4.9(c)), the curve fit was computed from the $a_{4,0}$ amplitude after its first period. The main difference when comparing the pure mode deformation with the complex shape here is on the mode 4 damping rate. This difference can be understood by looking at figure 4.9(c). It is clearly seen that, in contrast to mode 2, mode 4 deformation is not perfectly aligned with the reference frame ($a_{4,2}$ and $a_{4,-1}$ are not negligible). Thus, the coupling between orders l plays an important role and the damping can not be evaluated only from the time evolution of coefficient $a_{4,0}$.

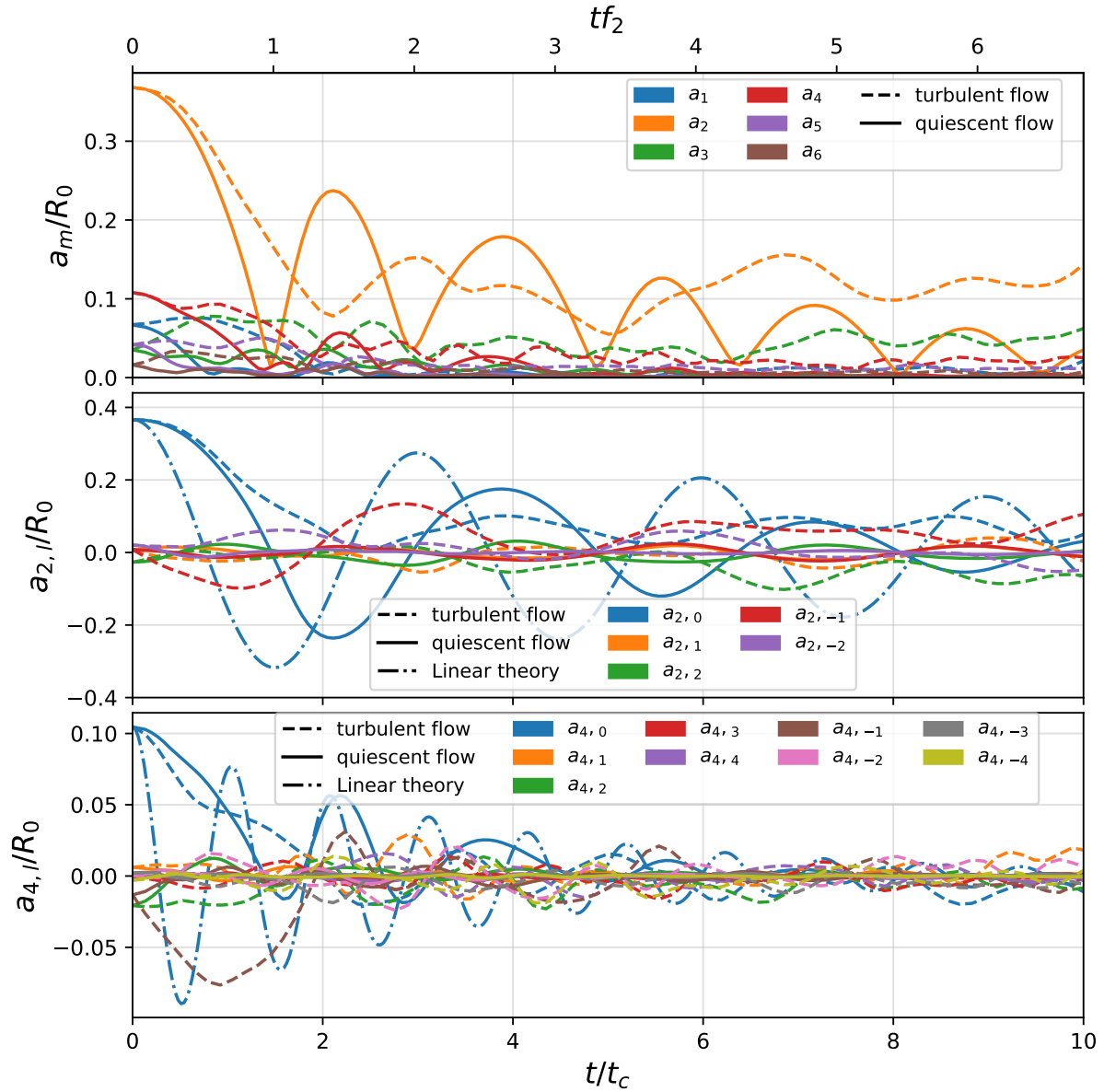


Figure 4.9: Oscillations of droplet **A** from its maximum deformation state $\zeta_\Omega = 0.39$. (a) $t - t_{peak}$ spectrum coefficients a_m as a function of the dimensionless time tf_2 of a realization transferred into a quiescent flow. (b) Evolution of the spherical harmonic coefficients $a_{2,l}$ after rotating the reference frame to maximize coefficient $a_{2,0}$. (c) Evolution of the spherical harmonic coefficients $a_{4,l}$ in the same reference frame.

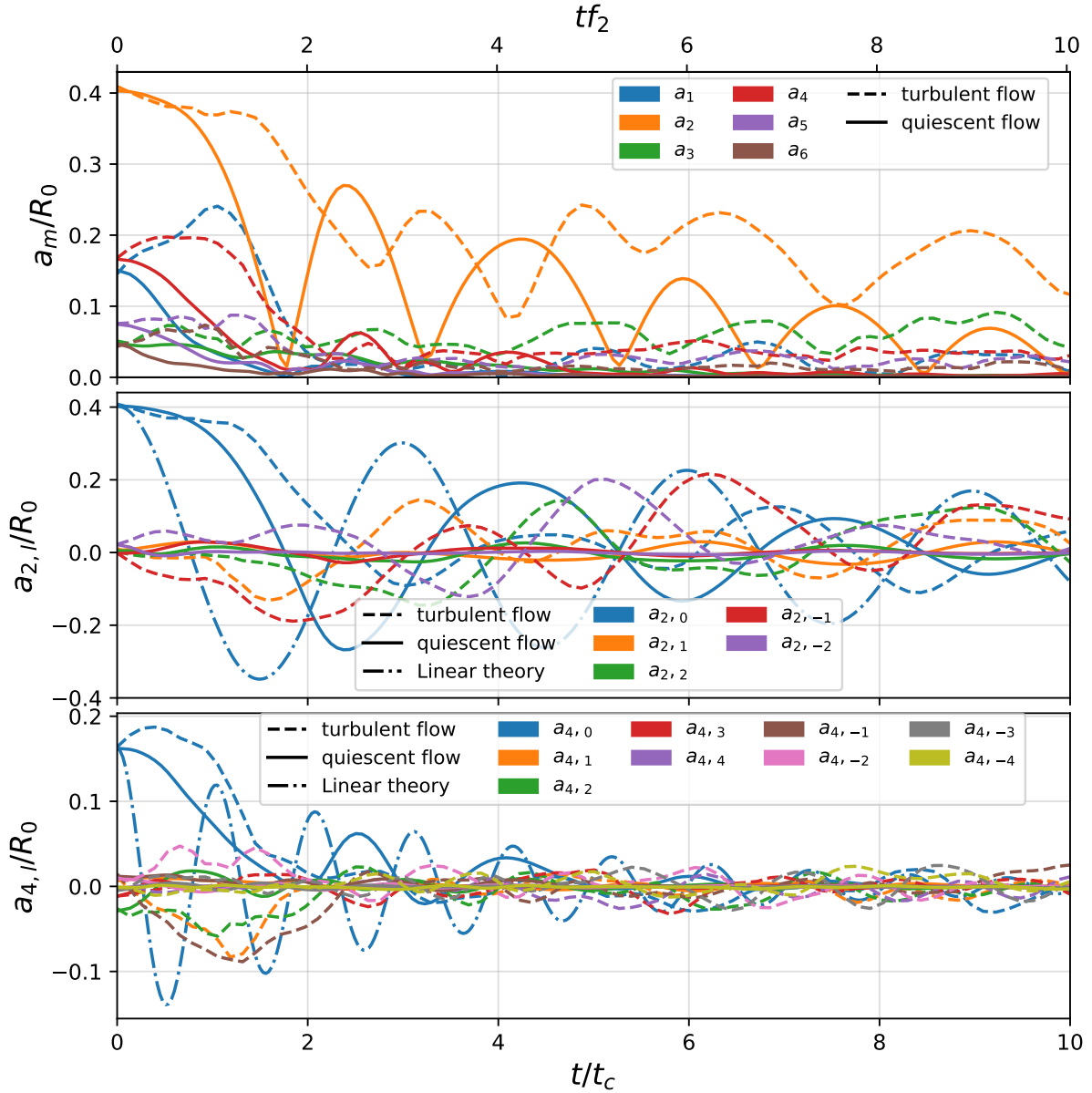


Figure 4.10: Oscillations of droplet **B** from its maximum deformation state $\zeta_\Omega = 0.47$. (a) $t - t_{peak}$ spectrum coefficients a_m as a function of the dimensionless time $t f_2$ of a realization transferred into a quiescent flow. (b) Evolution of the spherical harmonic coefficients $a_{2,l}$ after rotating the reference frame to maximize coefficient $a_{2,0}$. (c) Evolution of the spherical harmonic coefficients $a_{4,l}$ in the same reference frame.

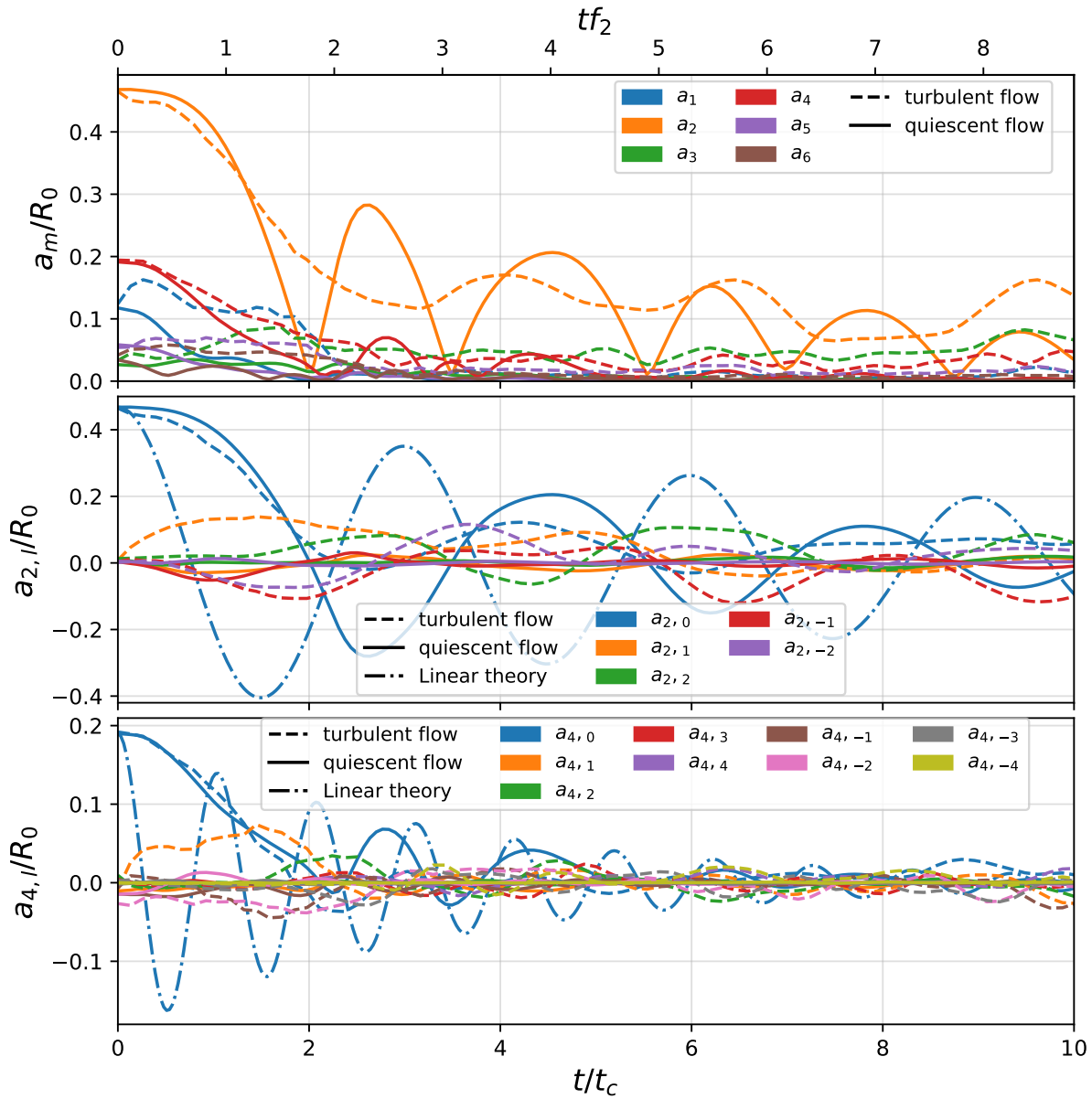


Figure 4.11: Oscillations of droplet **C** from its maximum deformation state $\zeta_\Omega = 0.52$. (a) $t - t_{peak}$ spectrum coefficients a_m as a function of the dimensionless time tf_2 of a realization transferred into a quiescent flow. (b) Evolution of the spherical harmonic coefficients $a_{2,l}$ after rotating the reference frame to maximize coefficient $a_{2,0}$. (c) Evolution of the spherical harmonic coefficients $a_{4,l}$ in the same reference frame.

Mode	2		3		4		5		6	
	ω	β								
Eq. & Eq.	1.00	0.0106	1.890	0.0297	2.89	0.057	3.99	0.0933	5.19	0.138
Eq. 3.29	0.959	0.0441	1.81	0.0849	2.76	0.135	3.81	0.195	4.95	0.264
Individual modes (sect. 3.5.2)	0.738	0.0841	1.861	0.214	2.544	0.288	3.70	0.374	4.79	0.440
Turbulent flow (sect. 4.3)	1.11	-	1.96	-	2.29	-	2.88	-	3.34	-
Quiescent-flow A (sect. 4.4, fig 4.9)	0.853	0.107	-	-	1.76	0.336	-	-	-	-
Quiescent-flow B (sect. 4.4, fig 4.10)	0.699	0.130	-	-	-	-	-	-	-	-
Quiescent-flow C (sect. 4.4, fig 4.11)	0.759	0.123	-	-	-	-	-	-	-	-

Table 4.2: Summary of frequencies ω and damping ratio β normalized by ω_{20} .

4.5 Conclusion

A droplet database generated by direct numerical simulation was used to characterize the oscillations of droplets. A framework for droplet deformation using a spherical harmonic decomposition of the droplet surface has been presented.

Droplets immersed in a turbulent background flow are studied. The present work is based on a database that is still being extended for different purposes, in particular to investigate the droplet breakup and the turbulent/interface interactions. This database considers many realizations with similar dimensionless numbers.

It is demonstrated that mode 2 is the dominant mode of deformation in a droplet undergoing turbulence-driven deformation. Oscillations of each spherical harmonic coefficient are observed, with a frequency that is close to the theoretical frequency obtained from the linear theory (Chapter 3). These observations extend the existing literature, which has focused solely on the turbulence coupling with mode 2. The total deformation is analysed using the power spectrum. The ensemble average of the power spectrum, which can be considered the energy stored at the interface for each mode, reaches a statistically converged level. This saturation level is related to the droplet's natural damping rate and the turbulent cascade. The scaling of this saturation level has not yet been established. Finally, a study of high-amplitude deformations is performed. The spherical harmonics reference frame is aligned with large deformation axis maximizing the $a_{2,0}$ coefficient. For these deformations, the coupling between even modes is observed. The droplet relaxation is related to capillary forces, as shown by the simulation of the same droplet but without any initial velocity field. The damping rate is similar to the one obtained in the single mode simulations.

Three main perspectives can be drawn and are being explored by different groups. First, it has been demonstrated that the weakly viscous linear theory provides accurate information on how droplets evolve. Extending existing theories allows for the answering of two main questions: (i) how modes are coupled in the case of complex shape droplets; and (ii) how singular eddies excite each mode, modifying the angular frequency oscillations. This second point is currently underway of being explored by a future PhD group. Second, new simulations with different Weber and Reynolds should be performed in order to provide a more detailed picture of how turbulence and the interface interact

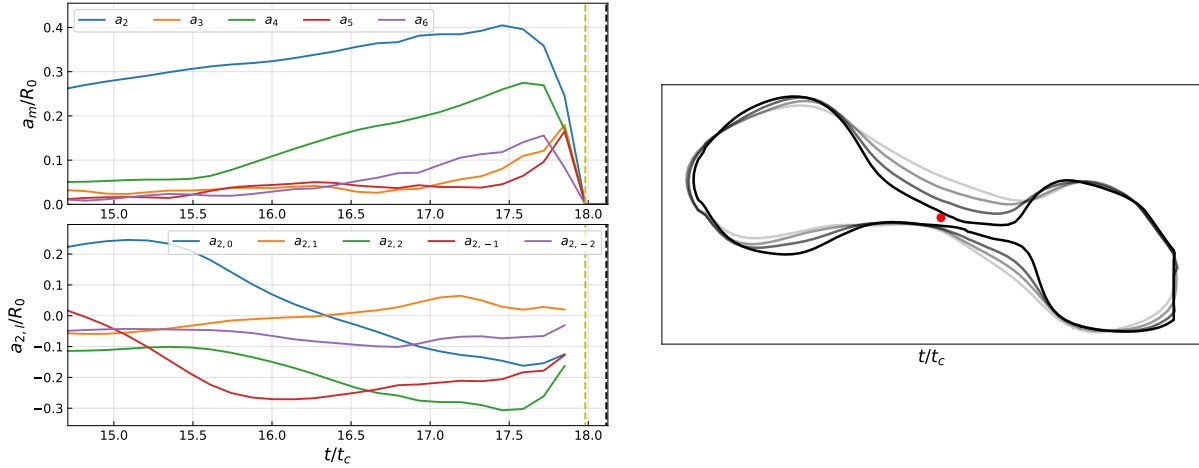


Figure 4.12: Loss of star shape constraint does not allow for the computation of the spherical harmonic functions that describe the drop shape. The black dashed line corresponds to the breakup event and the yellow dashed line to the time in which the star-shape constraint is lost. On the right the isocontour of the droplet at its centre for the last 5 iterations before the loss of the star shape constraint.

at each length scale. This is the most straightforward approach to understanding how the saturation level for each mode power spectrum scales with turbulence. Furthermore, extending the present work to encompass droplets in a gaseous environment and bubbles in a liquid, both numerically and experimentally, promises to enhance our understanding of turbulence-interface interactions.

The implementation of spherical harmonics to describe the shape oscillations of droplets in turbulence proves useful to relate the drop oscillations with the existing linear theory and to quantify the energy *stored* by each mode. This allows us to relate the dissipation of the dispersed phase kinetic energy into the drop internal energy. Due to the condition of the star-shape domain to compute the spherical harmonic decomposition, this analysis is not extendible to near-breakup droplets as seen in figure 4.12. When approaching the breakup stage, the ligament or neck connecting the two principal lobes appearing during the breakup process begins to thin. At a given moment, the conditions restricting the decomposition in spherical harmonics of the droplet shape do not allow for further computing. Due to this fact, is necessary to introduce other approaches to describe the interface at the latter stages of the drop lifetime. In chapter 5 the near-breakup part of the droplets lifetime will be investigated.

Chapter 5

Multiscale analysis

5.1 Introduction

Turbulence is one of the most important mechanisms by which breakup of droplets can be achieved. In particular, when analysing the complex geometries near pinch-off, the classical shape parameters, such as averaged curvature and aspect ratio, are not sufficient to define a critically deformed state Håkansson et al. (2022b), Deberne et al. (2024). Throughout the droplet deformation, perturbations of different origin favour the growth of liquid structures of different sizes and shapes. Notably, regions exhibiting contraction (bottle-necks) and accumulation (swelling) patterns may indicate potential breakup events. The multiscale nature of these systems must be considered when describing mechanisms to accurately predict breakup events.

Throughout chapter 4, the deformation of droplets is characterized using the spherical harmonic decomposition framework. This analysis though, did not provide the shape characteristics of the final moments of the droplet lifetime due to limitations in the description of the spherical harmonic functions. Hence, the need for a more comprehensive analysis is necessary.

The present study uses a previously developed multiscale description tool (Dumouchel et al. 2017, 2022) to investigate the behaviour of simulated drops in a turbulent environment from the database of droplets described in section 4.2.1. The multiscale framework considers the liquid system as well as all systems parallel to it in the liquid phase. These parallel systems refer to those that are obtained through successive erosion operations. This consists of removing the liquid system region covered by a sphere of diameter d dragged along the liquid-gas interface keeping the centre of the sphere on the interface surface, providing a description of the droplet deformation at all the levels. The system is described using the cumulative scale distribution $E_3(d)$, which corresponds to the liquid volume lost after the scale d erosion operation, and its successive derivatives. At small scales these quantities are equivalent to the Minkowski Functionals.

The scale distribution and successive derivatives report valuable information on the

shape of the system. For instance, they inform on the presence of bottlenecks, flattening or swelling. They also introduce specific characteristics such as the minimum and maximum length scales whose temporal evolution is accessible. The objective of this work is to investigate the breakup of drops submitted to a turbulent environment with the help of these indicators. A critical deformation state is sought following the work of Håkansson et al. (2022b).

5.2 The multiscale description

The multiscale analysis describes the liquid system by the cumulative scale function $E_n(d)$ where d is the scale of observation. The multiscale analysis was introduced to characterize liquid sprays in the work of (Dumouchel & Grout 2009) and was successfully applied to describe the atomization process of liquid sheets produced by a triple-disk nozzle. This function is obtained by applying successive erosion operations to the liquid system. The multiscale description analysis considers the liquid system and all the parallel systems in the liquid phase. These parallel systems are obtained through successive erosion operations in all possible scales until the totality of the initial system is eroded. The erosion operation at scale d consists of removing the region of the liquid system that is covered by a sphere (centred at the interface) of diameter d along the interface of the initial system. This operation is represented in figure 5.1.

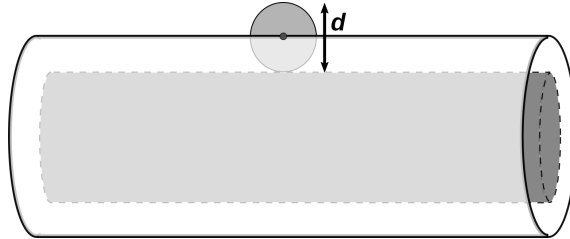


Figure 5.1: Erosion of the system with a spherical structuring element of diameter d . The volume $V(d)$ of the remaining part of the system is the grey surface delimited by the dashed line.

In three-dimensions, the cumulative distribution of scales is given by

$$E_3(d) = V_T - V(d) \quad (5.1)$$

Where V_T is the total volume of the liquid system and $V(d)$ the volume of the system eroded at the scale d . The derivative on the scale d of the cumulative distribution $E_n(d)$ gives the distribution of scales $e_n(d)$, meaning

$$\frac{\partial E_n(d)}{\partial d} = e_n(d) \quad \text{where } n = 2, 3 \quad (5.2)$$

The distribution of scales $e_n(d)$ and its successive derivatives $\left(\frac{\partial e_n(d)}{\partial d}, \frac{\partial^2 e_n(d)}{\partial d^2}\right)$ provide information of the morphology of the system. For 2D systems for example, $\frac{\partial e_2(d)}{\partial d}$ is proportional to the size distribution of elongated elements (ligaments) and the cumulative size distribution of the contracted elements (spherical) that make up the shape of the liquid flow (Dumouchel et al. 2017). The sensitivity of this derivative to the topology of the liquid structures allows for the study of elongations and dilatations that characterize the atomization process. The atomization mechanism is in fact a sort of competition between the elongation and contraction processes. The first one promoting the appearance of ligament-like structures and the second one a dilatation zone as a potential precursor of the droplet breakup. The multiscale analysis consequently appears to be relevant for characterizing the breakup of droplets.

A previous study (Thiesset et al. 2019) demonstrated that the successive derivatives of the volume function $V(d)$, characteristic of the volume of the eroded systems represent the respective surface $S(d)$ of the eroded system at the scale d , the area integrated mean curvature $H(d)$ and the area integrated Gaussian curvatures $G(d)$. By virtue of the Gauss-Bonnet theorem for a closed surface, the surface average of the Gauss curvature is proportional to the Euler characteristic $\chi(G = 2\pi\chi)$, where χ is a topological invariant. This means that it is only dependent on the topology of the body in question, regardless of the way in which the body is bent. For example $\chi = 0$ for a cylinder or any other shape similar to a cylinder (extruded systems). For a sphere or any other body of similar shape $\chi = 2$.

These quantities turn out to be the systems Minkowski functionals, a notion issuing from integral geometry. These functions are described in section 2.5 of the manuscript. The combination between these functions with the concept of parallel systems allows the characterization of complex structures. In terms of scale distribution, the following system of equations is established

$$\begin{cases} e_3(d) = \frac{S(d)}{2} \\ \frac{\partial e_3(d)}{\partial d} = \frac{H(d)}{2} \\ \frac{\partial^2 e_3(d)}{\partial d^2} = \frac{G(d)}{4} \end{cases} \quad (5.3)$$

However, this system does not apply to all scales, but is only valid for those producing a smooth eroded system. Meaning, it is no longer valid when the surface of the eroded system shows a discontinuity of curvature on at least one point. These points are called cusps. The number of cusps in an eroded system depends on the shape of the system and the scale of erosion, and depending on the case, they may be isolated points or form singular lines. Particularly, the prolate spheroid (rotation with respect to the ellipse major axis) and an oblate spheroid (rotation with respect to the ellipse minor axis) are clear examples of this. Indeed, the medial axis of prolate spheroids is a line which is co-linear with the ellipse major axis while the one of oblate spheroids is a circle perpendicular to the ellipse minor axis. The cusps observed on the eroded system are the points which

have more than one neighbour at the distance $d/2$ from the interface. The smallest scale in which this characteristic is displayed is called the reach of the system. A representation of the original system, its parallel systems and the reach can be seen in figure 5.2.

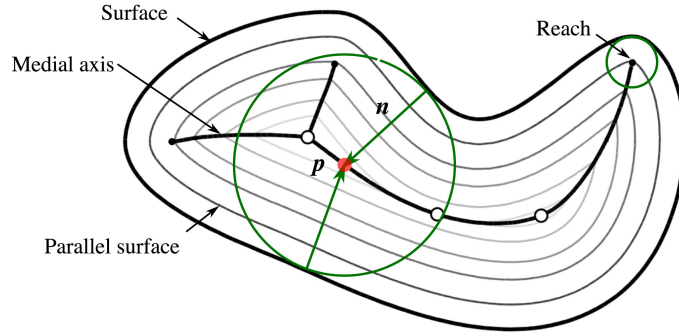


Figure 5.2: Graphical representation of the original body and its parallel surfaces. The medial axis (solid black line) the reach and the cusps (black dots) of a surface are also shown. Source (Dumouchel et al. 2022).

The group of equations described in equation 5.3 does not apply for the erosion scales greater than the reach of the liquid system. Hence, the reach is an important parameter since it separates the range of erosion scales for which the system can be described using only geometric measures and the range of scales where the Minkowski functionals start being a morphological descriptor thereby providing information not only about the geometry, but also about the structure. For scales above the reach becomes, then, a correction is introduced to the scale distribution obtaining

$$\begin{cases} e_3(d) = \frac{S(d)}{2} \\ \frac{\partial e_3(d)}{\partial d} = \frac{H(d)}{2} + C_H(d) \\ \frac{\partial^2 e_3(d)}{\partial d^2} = \frac{G(d)}{4} + 2\pi C_G(d) \end{cases} \quad (5.4)$$

Here, the functions $C_H(d)$ and $C_G(d)$ represent a correction for the functions $H(d)$ and $G(d)$ respectively, and $L(d)$ depends on the ensemble of points that form the cusp. The derivations for such corrections are presented in the work of (Dumouchel et al. 2022) for specific cases. As an example of how the multiscale analysis can give us information on the shape of the evaluated system two test cases are introduced due to their relevance to the oscillating drop deformation: prolate and oblate spheroids. The representation of these test cases are presented in figure 5.3. Figure 5.4 presents the comparison between the functions $H(d)$ and $\frac{\partial e_3(d)}{\partial d}$ determined numerically.

It is possible to observe that the Minkowski functionals and the scale distribution for all the parallel systems the shown cases are not identical in the interval of the characteristic scales of the systems. These differences allow the differentiation of two systems that, when looking at the distribution of the mean curvatures $H(d)$ across all scales, appear

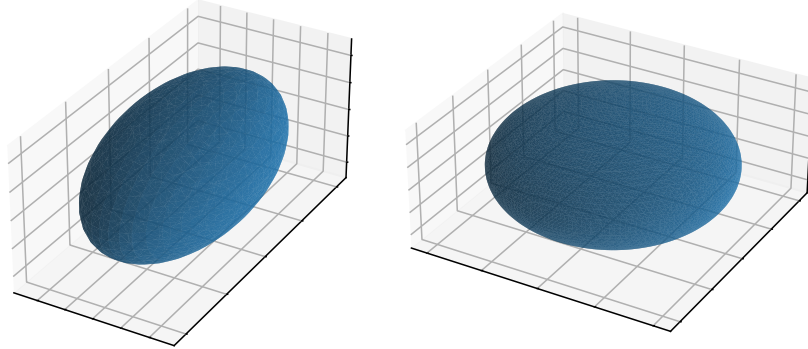


Figure 5.3: Representation of the different validation test cases. Prolate (left) and oblate (right) shapes.

to be similar. The smallest scale at which the derivative $\frac{\partial e_3(d)}{\partial d}$ differs from the function $H(d)$ is defined as the scale at which we find the reach of the system and will be denoted as d_r . Another interpretation for the scale d_r comes from its significance. The scale d_r represents the scale at which the highest local curvature can be found in the liquid system. Its worth noting that even though the prolate does not appear to have the scale d_r in figure 5.4a), this scale is still present and can be also be described as the smallest scale at which the derivative $\frac{\partial^2 e_3(d)}{\partial d^2}$ differs from the function $Xi(d)$. These results are in agreement with the derivation and results presented in (Dumouchel et al. 2022).

For the computation of the numerical values shown in figure 5.4, the Minkowski functional sub-routine of PyArcher is considered (see section 2.5).

5.3 Multiscale analysis of drops in turbulence

As mentioned in chapter 4, the spherical harmonic tool provided useful insight into the shape oscillations and deformation of the droplets in turbulence. Nonetheless, the star-shaped domain constraint given by the spherical harmonic functions does not allow us to observe what are the deformation dynamics at the droplets close to breakup. The introduction of the multiscale description grants observation beyond the previously imposed constraints and associate the droplet deformation as an ensemble of shape parameters. This multiscale description will therefore be used to study the drop shape dynamics (i.e. the presence of bottlenecks, flattening or swelling) for droplets immersed in a turbulent background flow from the numerical database presented in section 4.2.1.

In the test cases shown in figures 5.3 and 5.4, the functions $H(d)$ and $\frac{\partial e_3(d)}{\partial d}$ for prolate and oblate systems presented a visualization of how the multiscale analysis can pro-

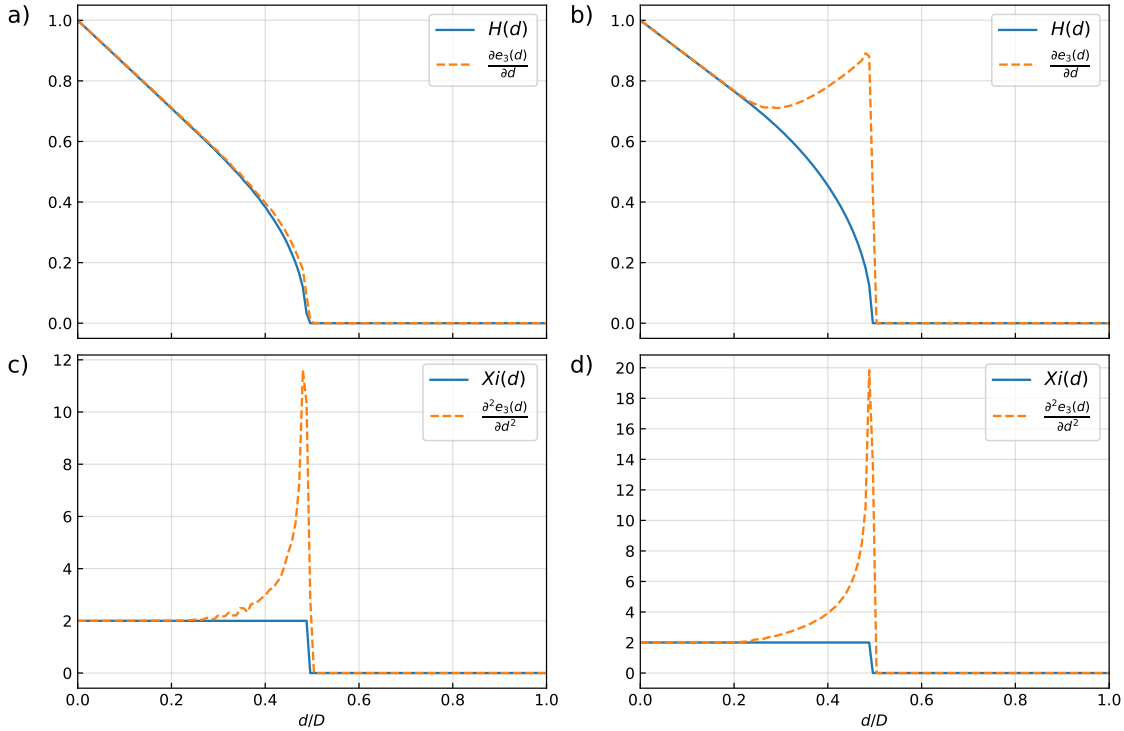


Figure 5.4: Comparison of functions $H(d)$ and $\frac{\partial e_3(d)}{\partial d}$ (top) and functions $Xi(d)$ and $\frac{\partial^2 e_3(d)}{\partial d^2}$ (bottom) for a prolate spheroid (left) and an oblate spheroid (right)

vide information on the shape of the droplet. This analysis is not as straightforward for droplets in turbulence. The deformation and oscillations induced by the turbulent eddies surrounding the liquid system rarely produce simple geometries like the ones presented. More often than not, this liquid-gas interaction leads to complex geometries that involve a distribution of spheres and sheets. A comparison of functions $H(d)$ and $\frac{\partial e_3(d)}{\partial d}$ for a droplet immersed in a turbulent background flow at different times is presented in figure 5.5 from its initial spherical state until shortly before the breakup. It can be observed that throughout the droplet lifetime, the shape can be described as a composition of spheres, cylinders and sheets. Meaning the geometry at different scales can experience zones of flattening (distribution of sheets), of elongated ligaments (distribution of cylinders) and zones of swelling (distribution of spheres). One key point is the similarity between the results shown in figure 5.4 and figure 5.5. In particular, the results show a resemblance to the oblate test case, indicating that the influence of the turbulent flow induces a flattening in the liquid system. This flattening can be seen in varying extents, portraying a sort of flattening-elongation motion. Figures 5.5c-d) show the motion from an oblate-like shape to a prolate-like shape. This occurs due to the peak of pressure existing along a circular medial axis and the surface tension forces controlling the deformation over the turbulence,

pushing the droplet to return to its spherical state.

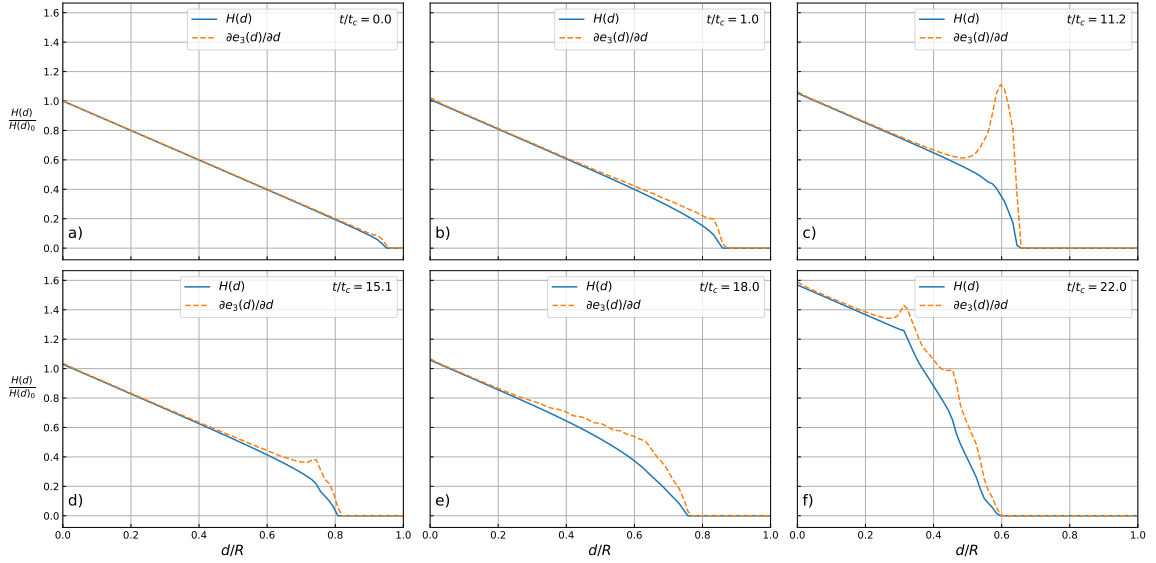


Figure 5.5: Difference between $e_3(d)$ and mean curvature $H(d)$ for increasing time snippets of the droplet from left to right.

On the other hand, figures 5.5e)-f) show the evolution of the droplet towards two flattening zones. This indicates the appearance of two lobes, which in turn, also experience flattening due to the interaction with the turbulent flow. The generation of these two lobes in turn indicate the formation of a neck.

Indeed, these observations prove to be coherent with the shape of the respective surfaces which are presented in figure 5.6.

To analyse the drop shape evolution three specific scales will be followed along the droplet lifetime.

The scale d_{\max} , which is the smallest scale for which all multiscale description functions are equal to zero. Meaning, d_{\max} corresponds to the minimum scale for which the system has been completely eroded.

In section 5.2, the concept of cusp is introduced and the scale at which this is found d_r . Given that the scale d_r represents the scale at which the highest local curvature can be found in the droplet this will provide information on where the peak of pressure in the scale space of the droplet can be found.

Finally, it is of interest to be able to follow the neck formation of the droplet. Due to the interaction of the droplet with the turbulent flow, the droplet undergoes several instances of elongation and compression. This has been observed through the computation of the evolution of the surface area of the droplet (see figure 4.3). In order to characterize the formation of the neck, or the lack thereof, the scale d_χ is introduced. The scale d_χ represents the smallest scale at which 2 (or more) elements can be found. All of this

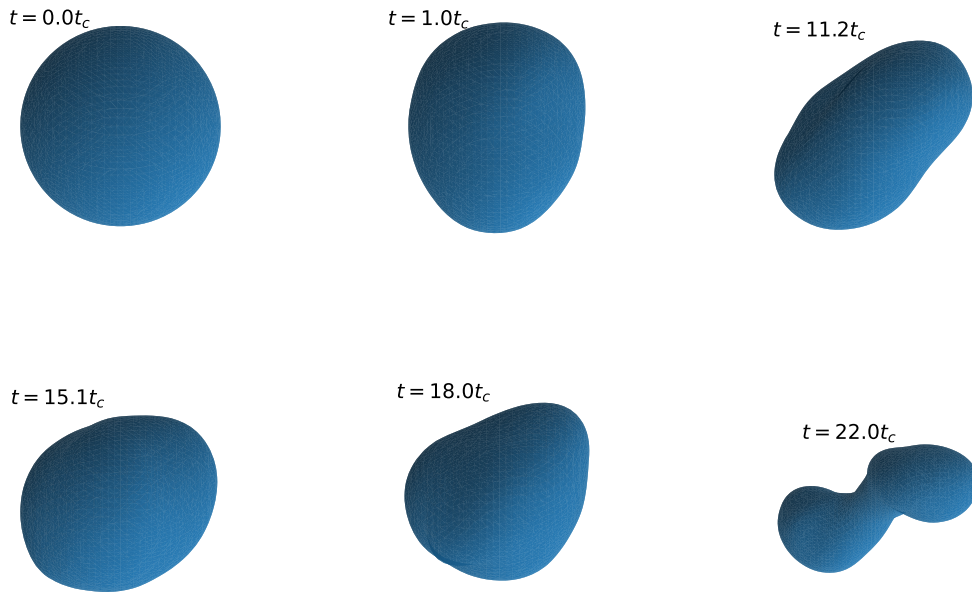


Figure 5.6: Representation of the surfaces of the droplets presented in the analysis of figure 5.5.

information can be obtained from the multiscale description presented in section 5.2. A representation of the selected scales, along with the corresponding shape parameters and where the different scales are found are presented in figure 5.7.

As presented in section 4.2.1, the numerical database currently consists of 192 breaking drop realizations. The numerical database also contains 48 non-breaking drop realizations. The evolution of the scales d_{\max} , d_r , d_χ is presented for two cases present in the numerical database, a droplet that does not experience breakup in figure 5.8 and breaking droplet in figure 5.9.

For both cases, the dynamics of the chosen scales are similar for most of the droplet lifetime. As observed in figures 5.8 and 5.9, throughout the droplet's lifetime the drop experiences oscillations as seen in chapter 4.

The first response of the droplet due to the interaction with the turbulent background flow is to rapidly depart from its spherical state, indicated by both d_{\max} and d_χ , within the first $2t_c$. This is in agreement with the information provided by the spherical harmonic decomposition in figure 4.6. The rapid decay of the scale d_r additionally indicates flattening as a response to the interaction with turbulence. It is observed that the droplet is kept flattened throughout the whole realization. This observation is in concordance with the

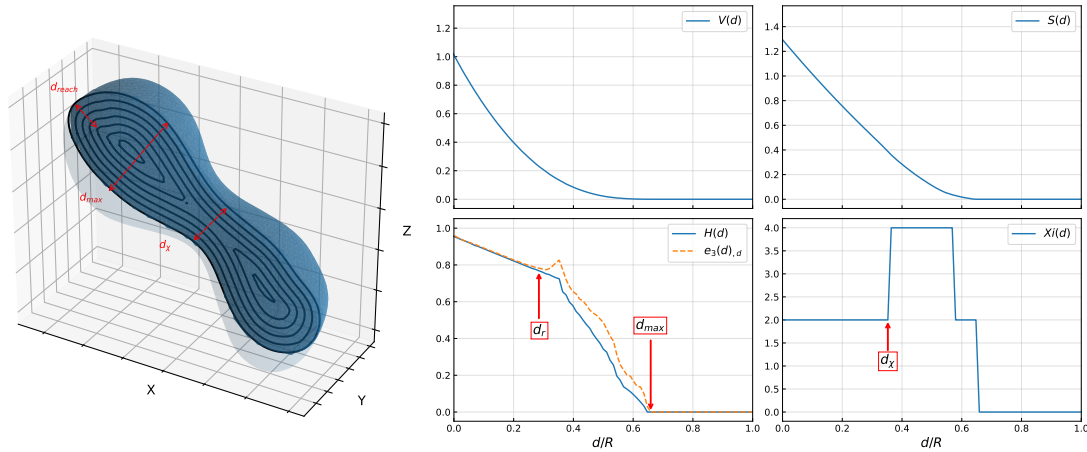


Figure 5.7: On the left: Representation of the selected scales to quantify the dynamics of the deformation. On the right: multiscale description of the shown droplet.

results presented in figure 5.5.

Throughout the deformation process there are instances in which the scales d_χ and d_{max} depart from one another. This second phenomenon observed indicates that the scale d_χ is representing a bottle neck or pinch-off diameter. Said events can be found multiple times with similar magnitude in breaking and non-breaking drops e.g. figure 5.8 $t/t_c \approx 24$ and figure 5.9 $t/t_c \approx 14$ or $t/t_c \approx 21$. Meaning, the formation of the neck and the magnitude of scales d_r and d_χ are not an indicator in itself of an upcoming breakup.

Finally, a third phenomenon can be found in the case of a droplet experiencing turbulent breakup shown in figure 5.9. Following a bottle-neck generation at $\approx 19 t_c$ there is a steady decline in the scale d_χ , indicating a thinning process in the neck of the droplet, similar to what occurs at $\approx 12 t_c$. Nonetheless, in this opportunity the droplet does not recover its quasi-spherical shape and continues deforming. It is observed that shortly before the breakup event occurs, a rapid decay of scales d_χ and d_r starting from $\approx 22 t_c$ occurs. Both scales drop promptly to 0.

It is necessary to mention that one of the advantages of the multiscale tool, is that it is possible to compute the morphological properties of the drop past the breakup, represented in figure 5.9 as the red dashed-line.

5.4 Breakup dynamics

The objective of this section is to characterize the breakup dynamics by considering the evolution in time of the scales d_{max} , d_r , d_χ . As observed in the previous section, breaking drops are characterized by a rapid decay of the two latter scales in the final stage previous to breakup. It was observed that all droplets presented similar dynamics approaching the

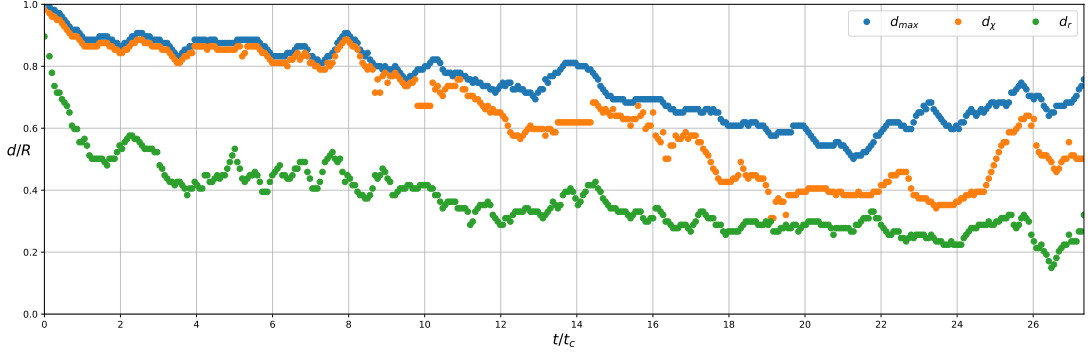


Figure 5.8: Scales d_{max} , d_r , d_χ as a function time for a non-breaking droplet.

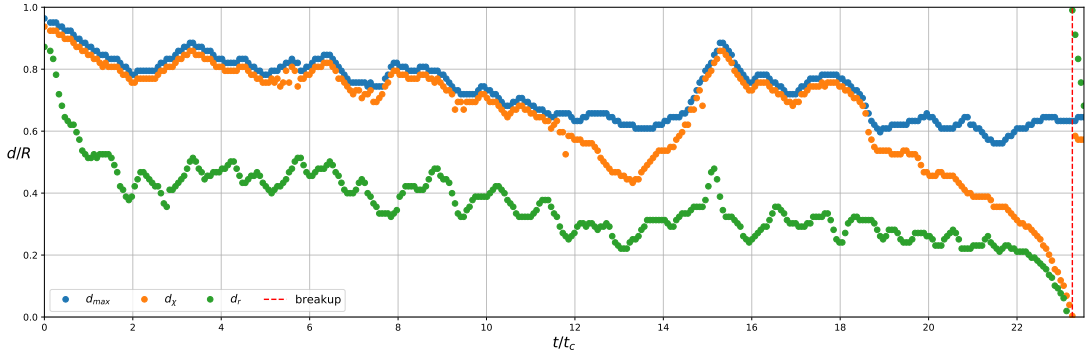


Figure 5.9: Scales d_{max} , d_r , d_χ as a function time for a breaking droplet.

breakup instance. To focus on these stage, the evolution of these scales for $(t_{breakup} - t) > -6 t_c$ for all breaking droplets of the database are studied. Scales were averaged and are presented in figure 5.10.

It is clear that the dynamics of the breakup are similar for all droplets of the database and that the breakup process is concentrated in the last $2 t_c$. Due to the similarity of the fragmentation process, there appears to be a critical point in which the capillary forces take over the deformation. Meaning, the turbulent vortices surrounding the droplet after this point do not control the dynamics of the drop.

To describe the critical point in which the droplet will break, the definition of the proposed scales is considered. When the droplet approaches breakup, it elongates and a neck begins forming. This is represented in the current analysis by the separation of the d_{max} and d_χ scales.

Following the work of Håkansson et al. (2022b) which in turn is based on the work of Xing et al. (2015), in an idealized scenario, a critically deformed state can be found when the static pressure is higher in the neck than in the formed bulbs and, therefore, the flow inside the droplet is from the neck into both bulbs eventually leading to breakup. The computation methodology for the radii of the bulbs and ligament is not described

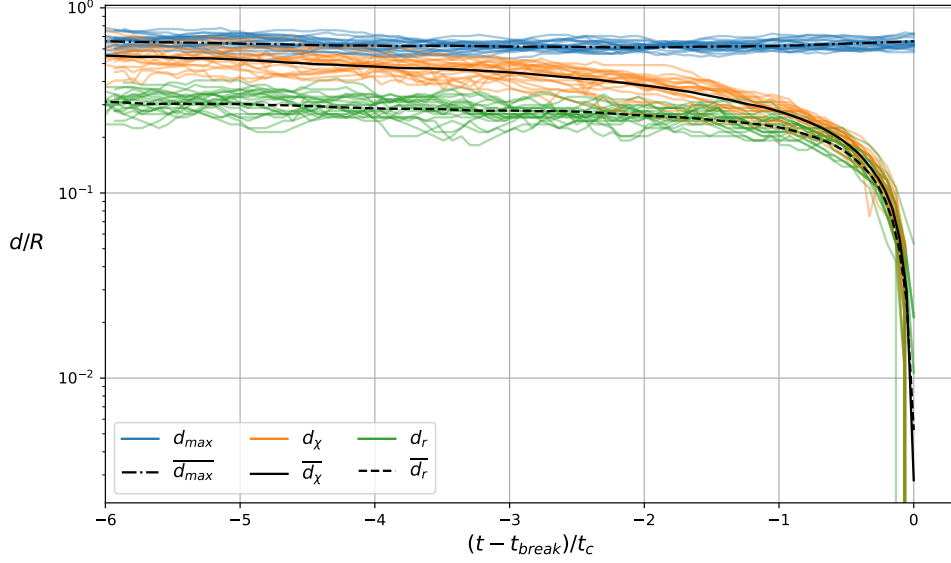


Figure 5.10: Scales d_{\max} , d_{χ} and d_r for all droplets of the database in blue, orange and green respectively. In the black lines, the averaged scales in the interval $(t_{\text{breakup}} - t) > -6 t_c$.

in the work of Håkansson et al. (2022b), thus only the multiscale analysis approach is presented. The multiscale approach provides a generalized way to estimate these two quantities. As mentioned previously, the scale d_{\max} corresponds to the minimum scale for which the system has been completely eroded. Hence, an approximation to the maximum diameter of the equivalent sphere that describes the bulbs is found in this scale. Therefore, an approximation of the pressure at the lobes can be obtained from the Laplace pressure $P_{L,d_{\max}} = 2\sigma/d_{\max}$. The scale d_{χ} , describes the diameter of the neck. In a simplistic way, the ligament that divides the two bulbs can be approximated to a cylinder. An approximation of the pressure at the neck can be obtained from the Laplace pressure $P_{L,d_{\chi}} = \sigma/d_{\chi}$, see figure 5.7. Finally, the scale d_r by definition represents the scale at which the highest local curvature can be found in the droplet and hence indicates the scale at which the peak of pressure of the droplet can be found. Under the assumption that a critically deformed state comprises the peak of pressure at the ligament uniting two spherical bulbs, the pressure obtained by the scale d_r will be measured in terms of a cylinder, therefore the Laplace pressure will be $P_{L,d_r} = \sigma/d_r$.

The critical state will be defined by the point in which the pressure given by the scales d_{χ} and d_r are greater than the one obtained by d_{\max} . This would indicate that peak of pressure is in the ligament rather than the extremes of the droplet.

The averaged values $\overline{d_{\max}}$, $\overline{d_{\chi}}$ and $\overline{d_r}$ along with the averaged critical time $\langle t_{\text{critical}} \rangle$ are presented in figure 5.11. The averaged critical time $\langle t_{\text{critical}} \rangle$ is found to be $1.3 t_c$ before the fragmentation event. The probability density function of the critical time presented

in figure 5.12 further cements this observation, showing that most of the droplets break within the range $0.5 t_c < \text{break} - t_{\text{critical}} < 2 t_c$. This is consistent with the findings of Deberne et al. (2024) in the same numerical database.

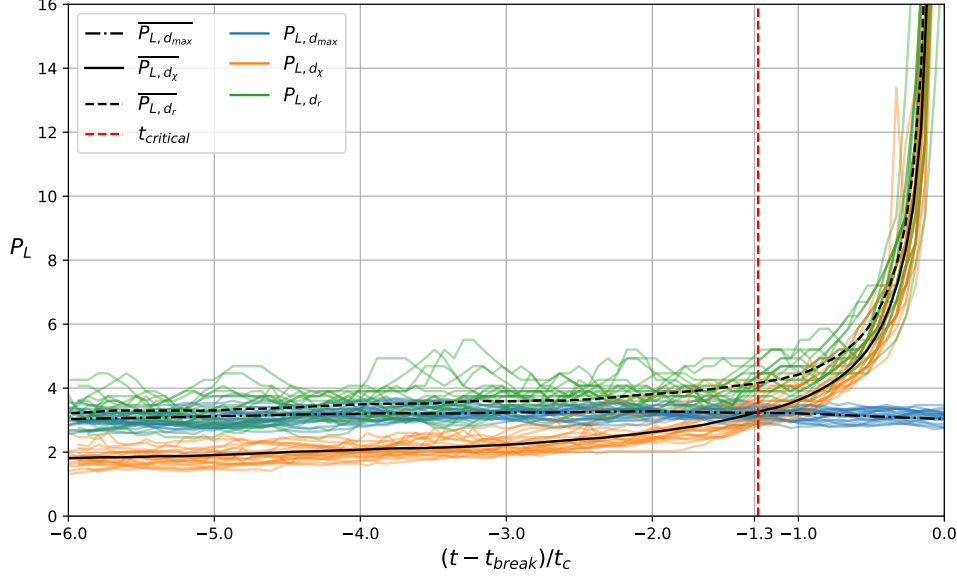


Figure 5.11: Representation of the Laplace pressures obtained from the scales d_{\max} , d_{χ} and d_r for all droplets of the database in blue, orange and green respectively. In the black lines, the averaged values in the interval $(t_{\text{break}} - t)/t_c > -6$. The red dashed line corresponds to the average critical time.

Figure 5.13 shows the histogram of the distribution of scales d_{\max} , d_{χ} and d_r throughout the last $6 t_c$ before breakup for all droplets of the database, as well as the histogram of the distribution of scales at t_{critical} . The comparison between the two histograms shows that the distribution of the scales d_{χ} and d_r for droplets with an upcoming breakup are concentrated in a specific interval. It also shows that the magnitude of scale d_{\max} does not have a great impact in predicting an upcoming breakup.

To test this threshold, several realizations were taken from the critical time time-step. To ensure that the breakup occurs due to capillary forces, the deformed droplets were left to evolve considering an initially quiescent flow. This approach was also presented in the work of Håkansson et al. (2022b) and implemented in 3.5.2. The surfaces are presented at the top of figure 5.14. The breakup dynamics are characterized using the proposed scales. The three selected droplets experience breakup even after removing the effects of the surrounding fluid. This confirms the fact that the breakup at this stage is a purely capillary-driven process.

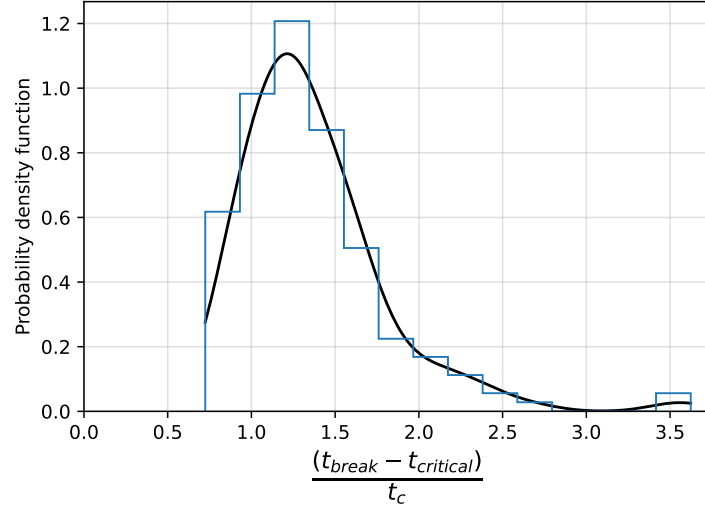


Figure 5.12: Probability density function of the distribution of $(t_{\text{break}} - t_{\text{critical}})/t_c$.

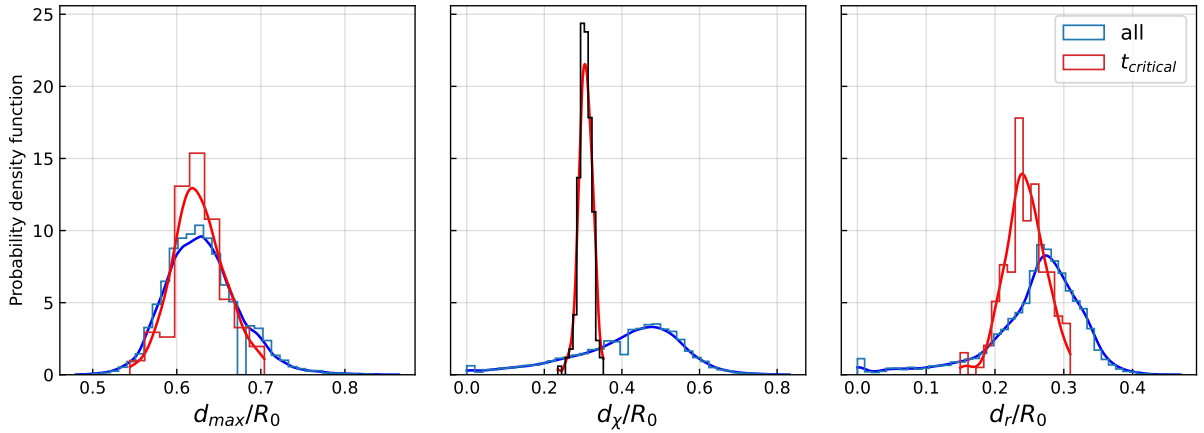


Figure 5.13: Probability density function of the scales d_{max} , d_{χ} and d_r normalized by the initial radius R_0 for all the database (blue) and for droplets at critical time t_{critical} (red).

5.5 Conclusion

A multiscale analysis of droplets in turbulence was performed for a numerical database of 243 realizations (4.2.1). This analysis provides additional information on the droplet morphological properties that are not possible to obtain through the spherical harmonic decomposition framework. More importantly, it is possible to apply this analysis even for complex geometries in which the spherical harmonic constraints make it difficult.

Drops are described using a cumulative distribution of scales and its successive derivatives. The scale distributions are compared with the Minkowski functionals for two typical

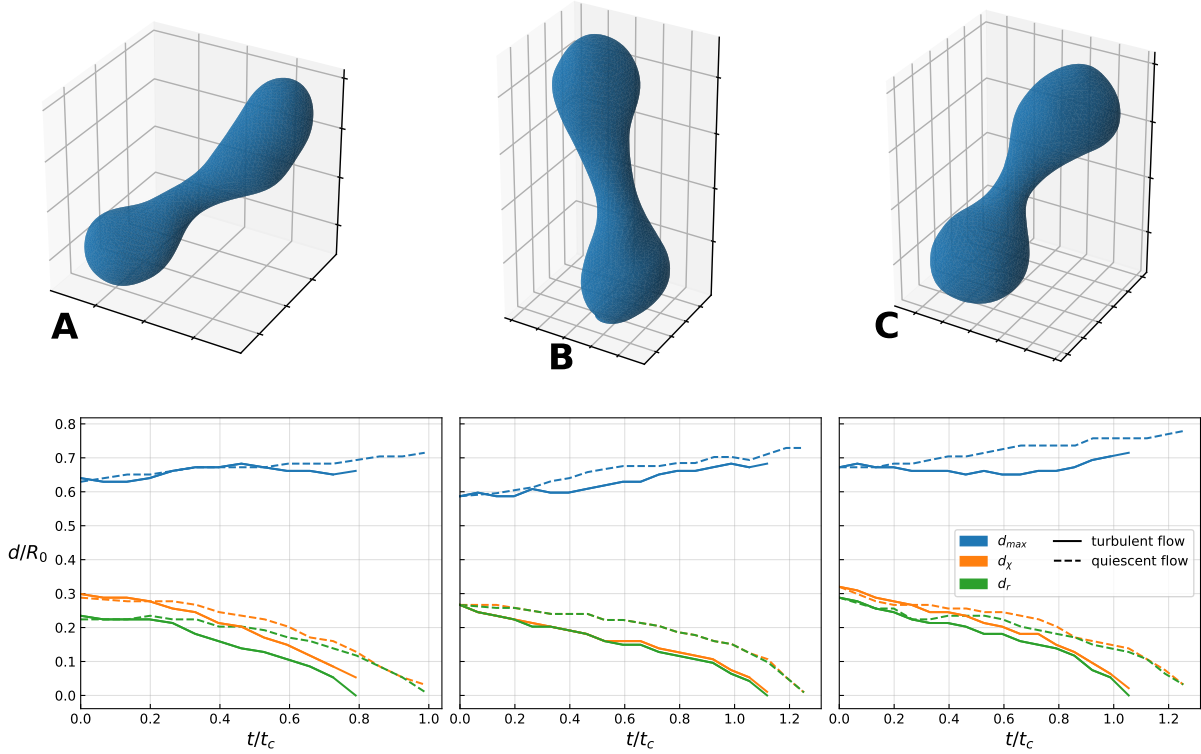


Figure 5.14: Representation of the surfaces of the droplets selected at $t_{critical}$ (top). Evolution of scales d_{max} , d_χ and d_r normalized by the initial radius R_0 . The dashed lines correspond to the evolution of the scales in the turbulent flow and continuous lines the evolution in a quiescent flow.

shapes of an oscillating drop: prolate and oblate systems. By applying this comparison it is found that the first effect of the interaction of the droplet with the turbulent background flow is the flattening of the surface. This flattened state is maintained throughout the droplet lifetime.

Applied to the cases in which droplet breakup is observed, it is demonstrated that the analysis is suited for probing the dynamics of the large scale and of the pinch-off mechanisms. In this analysis, the reach of the system (scale d_r) appears to be an important indicator. Another important indicator in this analysis is that of the scale d_χ , as it allows to identify the formation of the pinch-off ligament. It is observed that towards breakup these two scales share the same dynamics, indicating that at this level both scales are representing the same structure: the neck.

Following the work of Håkansson et al. (2022b), a critically deformed state is proposed by relating the scales d_{max} , d_χ and d_r to the dimensions of equivalent spheres and cylinders and computing the associated Laplace pressure of these systems using said scales. The critical state is tested for three droplets of the database by removing the turbulent

stresses of the flow, expecting to achieve droplet fragmentation purely due to capillary forces. The critical state proves to be good at capturing the change from turbulent-to-capillary-driven process. However, with the proposed method is not possible to predict upcoming fragmentation until the event, similar to morphological examination of droplet shape evolution to breakup present in the work of Deberne et al. (2024).

Nonetheless, more tests need to be implemented. In fact, said critical state corresponds simply to an approximation to the actual forces acting in the system. Given the complex geometries observed close to breakup, assuming spherical and cylindrical structures may not be the appropriate approach. Another problem is that the scales of both of the bulbs formed due to the thinning of the ligament forming the neck are not known. The scale d_{\max} only provides the dimension of the bulb with the largest radius. To the author's knowledge, this corresponds to the first application of the multiscale analysis to describe the deformation and breakup of 3D droplets in turbulence. A more extensive analysis using the multiscale approach in the future could provide the answers to these issues.

Chapter 6

Conclusions and perspectives

General conclusions

The principal objective of this work is to characterize the shape oscillations, deformation, and breakup of droplets interacting with a turbulent surrounding fluid focusing on the morphological properties of the system.

The first chapter presents an overview of the numerical methods used in this work. The in-house code ARCHER is presented, along with a description of the numerical methods used to describe interface behaviour. The work done during this PhD did not involve the further development of the ARCHER code. Hence, only a brief description of it is presented. The numerical methods described therein, are the ones that are necessary for the development of the post-processing tools presented.

Given that this work focuses on the morphology of the droplets, computing the interface motion is of utmost importance, and characterizing the deformation with the fields describing the interface is explored. Two main post-processing tools were developed and validated as part of this PhD work. A spherical harmonic decomposition framework and the inertia tensor computation and tracking.

The utility of the spherical harmonic framework is that it allows us to describe the drop shape as an ensemble of modes of deformation, even for complex geometries. The utility of the present framework comes from its ability to describe the drop shape as an ensemble of modes of deformation, even for complex geometries. As a consequence, this allows the observation of the effect of the different length scales on the liquid bulk by isolating each mode. That allows a different description of the droplet's shape and accounts for complex geometries.

The chaotic nature of the turbulent flows causes the droplets to move erratically, causing translation and rotation of the liquid system. The inertia matrix allows us to account for this phenomenon and follow the same reference frame throughout the deformation process. This algorithm aids us in the spherical harmonic expansion computation by ensuring that the excited modes are tracked effectively.

Lastly, the Minkowski functional framework is introduced. This framework was developed as part of a previous study (Dumouchel et al. 2022) and is used in this manuscript as an aid for the multiscale analysis approach.

As a foundation for the analysis of drops in turbulence, a linear stability analysis is performed. The Navier-Stokes system of equations is linearized accounting for the dynamic effects of both fluids. The solution of the dispersion relation is found, along with the expression of the physical quantities. The developed linear theory is validated against the DNS of droplets initialized with a perturbation on a single mode, considering the initialization with a static state (as in previous literature) and introducing the initial physical quantities found through the analysis. A numerical database of droplets deformed by a single mode is generated for modes $m \in [2, 6]$, Ohnesorge numbers $Oh \in [0.05, 0.6]$ and perturbation amplitudes in the range $\eta_0 \in [0.05, 0.4]$. In particular, three limiting cases were studied: droplet in a vacuum, buoyant droplet (liquid-liquid), and bubble immersed in a surrounding fluid. The single-mode oscillations are followed using the developed spherical harmonic framework, finding good agreement between the theory and numerical simulations. An energetic approach is considered Smuda et al. (2024), focusing on the energy transition from the two-phase flow system into the surface. Good agreement is found against the linear theory for droplets in a vacuum, even for initial deformation amplitudes of $\eta_0 = 0.4$. The energetic approach in the buoyant and bubble cases studied through DNS did not fully recover the linear theory, more specifically, the energy contained in the ambient fluid. These results highlight the need for finer mesh resolutions as the current work was not able to capture it completely. Concerning the linear oscillations, it is found that the simulations performed considering the initial physical quantities obtained from the theory do not provide additional information.

The oscillations of the droplets of this database are explored beyond the linear theory due to the non-linear effects introduced by the presence of viscosity and density of both fluids (Basaran 1992, Zrnić et al. 2022). In particular, the coupling between modes is investigated due to their relevance to the turbulent oscillation case presented in the next chapter. In particular, for mode 2, the appearance of oscillations different from the ones of the excited mode is found to be due to its alignment with mode 4. The opposite is true when initializing with an initial perturbation of mode 4. It is observed that the coupling is heightened with the initial deformation amplitude and dampened by the dynamic effects of the surrounding fluid. It was expected that the implementation of the physical quantities obtained from the linear stability analysis would provide less coupling. But this was not the case. A more comprehensive study, with higher resolution computations, is necessary.

To finalize the study of the coupling effects, the oscillations of a droplet initialized with perturbations of multiple modes are presented for deformation amplitudes up to $\eta_0 = 0.1$. Two cases are studied: axisymmetric and non-axisymmetric deformations. It is found that when the modes are aligned (same axis of symmetry), the coupling between them is promoted. When they are not aligned (different axes of symmetry), even when increasing the initial amplitude of each mode, they will act independently and with and in agreement

with the linear theory.

The second objective of this work is to study the deformation of droplets interacting with a turbulent surrounding fluid. The oscillations of droplets in turbulence are studied using the spherical harmonic decomposition framework developed. The droplets used for this study are part of a numerical database of droplets evolving under turbulent conditions, with multiple realizations of the same physical configuration (Roa et al. 2023b, Deberne et al. 2024). These oscillations are found to be close to the linear theory. The spherical harmonic framework successfully isolates the effects of each mode. It is demonstrated that mode 2 is the dominant mode of deformation in a droplet undergoing turbulence-driven deformation (Risso & Fabre 1998, Perrard et al. 2021, Roa et al. 2023b). It is found that the energy stored at the droplet's surface for each mode reaches a statistically converged saturation level. This is related to the droplet's natural damping rate and the turbulent cascade. The scaling of this saturation level has not yet been established. It is observed that the amplitude of the deformation is not directly linked to an upcoming breakup. Throughout the droplet lifetime instances of high deformation not leading to fragmentation are present. These large deformations are studied and the coupling between modes is observed (Kang & Leal 1988). The alignment of the even modes of deformation is confirmed, in agreement with the results of the linear analysis of the previous chapter and existing literature (Ravelet et al. 2011).

Finally, due to the physical constraints of the spherical harmonic framework, it is not possible to study the fragmentation process. The introduction of the multiscale analysis provides additional information on the droplet morphological properties that are not possible to obtain through the spherical harmonic decomposition framework. The droplets are described using a cumulative scale distribution (Dumouchel et al. 2017, 2022) and compared with prolate and oblate states. Through this analysis, it is found that the interaction of the droplet with the surrounding turbulence provokes a flattening of the drop's surface. This flattened state is maintained throughout the droplet's lifetime and is observed for all droplets of the numerical database. Finally, a critically deformed state is proposed by relating the scales d_{\max} , d_{χ} and d_r to the dimensions of equivalent spheres and cylinders, obtaining the equivalent Laplace pressure of these systems using said scales. This approach is based on the works of Xing et al. (2015) and Håkansson et al. (2022b). The critical state is tested for three droplets of the database by removing the turbulence and replacing it with a quiescent flow. The critical state proves to be good at capturing the change from a turbulent-to-capillary-driven process. However, it is not possible to predict upcoming fragmentation until shortly before the event.

Perspectives

In this work, promising results have been obtained to characterize the deformation and breakup of droplets in turbulence. The development of a generalized study of the linear oscillations solved through set initial conditions provides the equations that describe the physical quantities of the system. To account for the effect of the viscosity and density of the surrounding fluid, the expansion to non-linear analysis, following the approach of Zrnić & Brenn (2021), Zrnić et al. (2022), is necessary to account for the coupling between modes in different physical characteristics, in particular for the liquid-liquid case presented in this work. This could provide further insight into two main questions: how modes are coupled in the case of complex shape droplets; and how singular eddies excite each mode modifying the angular frequency oscillations. However, the analysis corresponds to the free shape oscillations. In order to have a clearer picture and direct comparison with the drop oscillations in turbulence, this study cannot provide information on the resonant mechanism due to the reaction to the turbulent forcing. A deeper study introducing a forcing term in the velocity field needs to be considered.

In the same line, a comprehensive study considering different physical parameters i.e. Weber number, Ohnesorge number, and viscosity and density ratios should be performed to provide a more detailed picture of how the turbulence and interface interact at each length scale. From the author's point of view, it is the straight way to understand how the saturation level for each mode power spectrum scales with the turbulence. Extending the physical parameters could provide further information on the breakup dynamics and the effect on the distribution of scales.

This work focuses on the morphological properties of droplets in turbulence, leaving aside the interaction of the surrounding fluid with the interface. In turbulent flows, the drop is subjected to eddies of many length scales. Recent studies have shed light on this topic, investigating the contribution of sub-bubble scale vortices to bubble breakup (Qi et al. 2022), and the effects of the surrounding fluid by studying the stretching of the fluid-fluid interface by outer eddies (Chen et al. 2019, Vela-Martín & Avila 2022). A comprehensive analysis of the mechanics of droplet breakup from an energetic perspective, focusing on the energy exchange between the eddies present in the turbulent flow and the droplet is currently under study. This work is part of an ongoing Master thesis project co-supervised by the PhD candidate. The pairing of the spherical harmonic analysis with the energy exchange between eddies could provide further insight into the mechanisms of deformation and breakup.

The multiscale analysis has proved to be a useful tool for characterizing the drop deformation. Even though this framework has been used in the past to study primary atomization in experimental jets (Dumouchel et al. 2017, 2023), to the author's knowledge this is the first application on 3D systems in turbulence. Therefore, the full potential of multiscale analysis has yet to be explored. In particular, the relationship between the distribution of scales and the interaction of the droplet with the turbulent eddies remains

CHAPTER 6 – CONCLUSIONS AND PERSPECTIVES

to be explored. This analysis could provide the necessary information to predict breakup at an earlier stage.

Appendix A

Synthèse générale

1. Introduction

L'atomisation est un mécanisme qui transforme un volume de liquide en un écoulement de petites gouttes, un spray, qui montre une quantité de surface d'interface augmentée. Ce processus est crucial dans diverses applications industrielles comme par exemple l'injection de carburant, l'irrigation par aspersion, le séchage par pulvérisation et la lutte contre les incendies. Chaque application nécessite des caractéristiques spécifiques du spray et notamment pour ce qui est de la distribution de taille des gouttes qui est essentielle pour l'efficacité de l'application concernée (Lefebvre & McDonell 2017).

La déformation et la rupture des gouttes au cours du processus influencent de manière significative la distribution de la taille des gouttes finales. Ces événements de rupture secondaire sont fonction de la turbulence régnant dans le milieu environnant. Plusieurs auteurs ont suggéré que la rupture turbulente des gouttes pourrait être attribuée à un mécanisme résonant résultant de leurs oscillations libres, même à faible niveau de turbulence (Sevik & Park 1973, Risso & Fabre 1998, Lalanne et al. 2019). Ce phénomène motive la présente étude.

Dans un premier temps, une analyse de stabilité linéaire des gouttes newtoniennes dans un fluide environnant newtonien est menée. Les oscillations linéaires des gouttes sont examinées à la fois d'un point de vue théorique et numérique, décrivant le mouvement oscillatoire de premier ordre d'une goutte initialement déformée en tenant compte des effets dynamiques du fluide environnant. Trois cas limites sont considérés : une goutte dans le vide, une configuration liquide-liquide et une bulle dans un liquide.

Par la suite, les oscillations et la rupture d'une goutte sphérique initialement non perturbée dans un milieu turbulent homogène et isotrope sont étudiées. Un cadre théorique pour les oscillations des gouttes est développé pour chaque mode de déformation en utilisant une décomposition en harmoniques sphériques qui suit la déformation de la surface depuis son état initial jusqu'à la rupture. Cette approche relie la déformation de faible amplitude de la goutte aux paramètres du milieu environnant, montrant comment la tur-

bulence excite différents modes et conduit à la rupture.

Pendant la déformation des gouttes, des perturbations d’origines diverses conduisent au développement de structures liquides de tailles et de formes variées. Ces structures peuvent être des zones contractions (goulots d’étranglement) et des zones d’accumulation de liquide (régions de gonflement). Selon le cas elles indiquent de potentiels évènements de ruptures. Pour prédire ces évènements, la nature multi-échelle des déformations doit être considérée. L’évolution temporelle de la distribution d’échelles est utilisée ici et permet d’identifier les dynamiques impliquées à chaque échelle dans le processus qui mène à la rupture de la goutte.

En combinant ces deux analyses, l’évolution de la goutte est étudiée en deux parties : d’abord, le mouvement oscillatoire et la fréquence des différents modes de la déformation à travers l’analyse de la décomposition en harmoniques sphériques reliant la déformation induite par la turbulence aux oscillations présentes dans la théorie linéaire, puis l’évolution temporelle de la goutte vers la rupture sur la base de sa distribution d’échelles.

Le travail présenté analyse la déformation et la rupture des gouttes dans la turbulence en trois étapes principales : une phase initiale de déformation due au flux turbulent, des mouvements oscillatoires induits par l’interaction avec les tourbillons turbulents, et la phase finale de rupture. Ces étapes sont représentées sur la figure A.1.

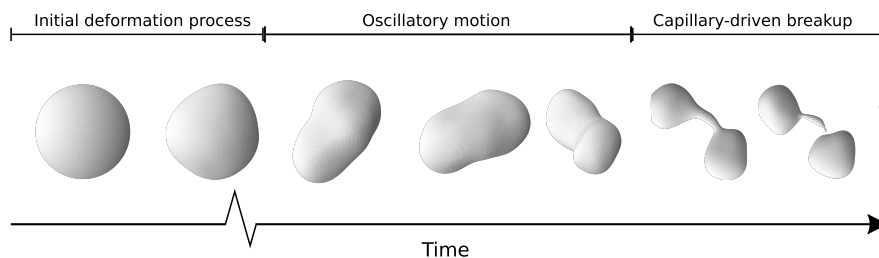


Figure A.1: Séquence d’instantanés d’une goutte en rupture suivant le processus d’oscillation, le processus de déformation inertielle et la rupture par capillarité tout au long de la durée de vie de la goutte. Figure inspirée par Qi et al. (2024).

2. Méthodologie

Décomposition en harmoniques sphériques

En mathématique et en physique, les harmoniques sphériques sont des fonctions définies sur la surface d’une sphère et souvent utilisées pour résoudre des équations aux dérivées partielles. Puisqu’elles forment un ensemble complet de fonctions orthogonales, tout système de type *star-shape* (ensemble radialement convexe) peut être décrit dans un repère de coordonnées sphériques et représenté en une somme de fonctions harmoniques

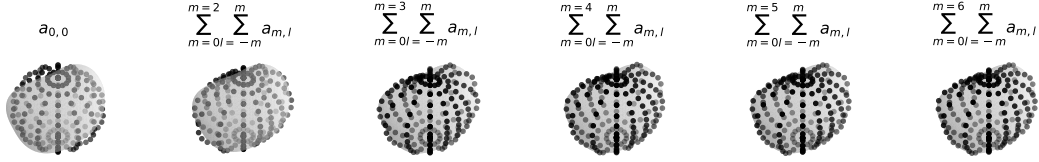


Figure A.2: Reconstruction d'une goutte déformée à l'aide des modes harmoniques sphériques $m = [2 - 6]$ obtenus par sa décomposition.

sphériques. Les fonctions harmoniques sphériques fournissent une base mathématique robuste pour représenter des formes complexes montrant des variations dans les directions radiale, polaire et azimutale.

Pour étudier l'évolution de la forme d'une goutte immergée dans un flux turbulent, nous introduisons les fonctions harmoniques sphériques $Y_m^l(\theta, \varphi)$, suivant les travaux de Risso (2000), Lalanne (2012) and Perrard et al. (2021).

La distance entre le centre du repère et l'interface de la goutte peut être décrite par :

$$R(\theta, \varphi) = R_0 \sum_{m=0}^{\infty} \sum_{l=-m}^m a_{m,l} Y_m^l(\theta, \varphi). \quad (\text{A.1})$$

Pour décrire la forme d'une goutte comme une série de fonctions harmoniques sphériques, la première étape consiste à obtenir la distribution de son rayon en fonction des angles polaires, soit $R(\theta, \varphi)$. Les valeurs de $R(\theta, \varphi)$ sont obtenues via une boucle qui les calcule à travers l'interface en suivant le repère de coordonnées sphériques en fonction des angles selon un tableau dont la taille est déterminée par le nombre maximal de modes, M , que nous souhaitons évaluer. Plus précisément, le tableau sera de forme $2(M+1) \times 2(M+1)$.

Les coefficients sont ensuite calculés à partir de ce tableau avec l'aide de la bibliothèque SHTOOLS (Wieczorek & Meschede 2018). Une transformation de Fourier rapide (FFT) est appliquée aux données d'entrée par rapport à la coordonnée longitudinale. Cette étape transforme les données dans le domaine fréquentiel pour la composante longitudinale. Pour chaque degré m et ordre l , l'algorithme intègre le produit des données d'entrée $R(\theta, \varphi)$, du polynôme de Legendre associé P_m , et du terme exponentiel $e^{il\varphi}$ sur la sphère, où φ est la longitude (voir l'équation 2.7) et θ la colatitude. Les coefficients harmoniques sphériques $a_{m,l}$ sont ensuite obtenus en résolvant l'intégrale montrée dans l'équation 2.11. De plus, en obtenant les coefficients $a_{m,l}$, le corps peut être reconstruit avec le nombre désiré de fonctions harmoniques sphériques. A titre d'exemple, la morphologie d'une goutte déformée par un flux turbulent est reconstruite en utilisant les six premiers modes de déformation dans la figure A.2.

Matrice d'inertie

Dans un écoulement turbulent, la forme de la goutte et son centre de masse changent dynamiquement en raison de l'interaction de la goutte avec les tourbillons turbulents. Un calcul précis de la matrice d'inertie nécessite des mises à jour en temps réel de ces deux quantités. Pour déterminer ses principales directions, nous calculons la matrice d'inertie I (Lalanne 2012, Chapitre 5). Elle contient deux types de composants : les moments d'inertie notés I_{xx}, I_{yy}, I_{zz} , qui sont respectivement les moments par rapport aux axes x , y et z , et les produits d'inertie, I_{xy}, I_{xz}, I_{yz} , qui modélisent une asymétrie géométrique du centre de masse par rapport aux plans respectifs (O, y, z) , (O, x, z) et (O, x, y) . Plus ces moments sont grands, plus la masse est distribuée loin des axes ou des plans en question. La matrice d'inertie est écrite sous la forme suivante :

$$I = \begin{bmatrix} I_{xx} & -I_{xy} & -I_{xz} \\ -I_{xy} & I_{yy} & -I_{yz} \\ -I_{xz} & -I_{yz} & I_{zz} \end{bmatrix}, \quad (\text{A.2})$$

$$\begin{aligned} I_{xx} &= \int_V \rho(y_o^2 + z_o^2)dV, & I_{yy} &= \int_V \rho(x_o^2 + z_o^2)dV, & I_{zz} &= \int_V \rho(x_o^2 + y_o^2)dV \\ I_{xy} &= \int_V \rho(x_o y_o)dV, & I_{xz} &= \int_V \rho(x_o z_o)dV, & I_{yz} &= \int_V \rho(y_o z_o)dV. \end{aligned} \quad (\text{A.3})$$

Le calcul de I est basé sur le champ VoF et est effectué dans le système de coordonnées dont l'origine est le centre de masse (voir l'équation 2.17). Étant donné que I est une matrice symétrique dont les éléments diagonaux sont positifs, il existe un repère dans lequel elle est diagonale. Ce repère est le repère principal d'inertie dont les axes sont les axes principaux d'inertie. Les valeurs propres I_1, I_2 et I_3 de la matrice sont les moments principaux d'inertie. Pour s'assurer que le repère reste valide à tout moment (par exemple, suivre la rotation de la goutte), il est nécessaire d'assurer la continuité des valeurs propres. Le repère inertiel principal (v_1, v_2, v_3) fournit la direction des vecteurs propres, mais pas leur signe. En connaissant le repère inertiel au temps $n - 1$, $(v_{n-1,1}, v_{n-1,2}, v_{n-1,3})$, le repère inertiel au temps n , $(v_{n,1}, v_{n,2}, v_{n,3})$ peut être obtenu.

Minkowski functionals

Une autre approche pour caractériser la morphologie d'un corps est l'utilisation des fonctionnelles de Minkowski. Les fonctionnelles de Minkowski sont un ensemble d'indicateurs morphologiques qui décrivent non seulement l'enveloppe du système liquide (surface) mais aussi sa topologie (connectivité) et sa forme (courbure géométrique) (Mantz et al. 2008). Ces indicateurs sont largement présents dans la littérature dédiée aux milieux poreux (Arns et al. 2003, Mecke & Arns 2005) et aux structures cosmologiques (Mecke

et al. 1993, Kerscher et al. 2001). Ils généralisent les intégrales de courbure des surfaces lisses à celles présentant des plis ou des points singuliers.

Dans un espace à trois dimensions, les fonctionnelles de Minkowski définissent quatre quantités géométriques d'un corps délimité par une surface S : le volume V enclavé par la surface S , l'aire de la surface S , la courbure moyenne intégrée sur la surface H et la courbure de Gauss intégrée sur la surface G :

$$S = \int_S dS, \quad H = \int_S \frac{1}{2}(\kappa_1 + \kappa_2)dS, \quad G = \int_S \kappa_1\kappa_2 dS \quad (\text{A.4})$$

où κ_1 et κ_2 correspondent aux deux courbures principales et dS est un élément de surface élémentaire.

L'ensemble des fonctionnelles de Minkowski possède des propriétés intéressantes, la plus importante étant l'additivité (les fonctionnelles de Minkowski d'un ensemble de corps sont la somme de leurs fonctionnelles respectives) et invariante par translation et rotation du corps. La propriété d'additivité est particulièrement utile pour les sprays qui sont des systèmes composés d'éléments disjoints. Par ailleurs, comme souligné dans les travaux de Thiesset et al. (2019) et Dumouchel et al. (2022), la fonctionnelle de Minkowski $G(0)$ d'un spray est proportionnelle au nombre N de gouttes qu'il contient.

3. Oscillations linéaires de gouttes et de bulles

Ce chapitre présente le développement mathématique linéaire des oscillations d'une goutte newtonienne immergée dans un fluide environnant newtonien et étend la littérature existante en fournissant les équations pour résoudre le cas général. Cela a été accompagné d'une simulation numérique directe du cas étudié en tenant compte de différents nombres d'Ohnesorge, et rapports de densité et de viscosité (ρ_r, μ_r).

La solution analytique de la relation de dispersion est obtenue et validée par rapport à la littérature existante sur les cas limites des gouttes et des bulles. Des simulations numériques directes (DNS) de gouttes avec différents nombres d'Ohnesorge et rapports de densité/viscosité sont réalisées et validées par rapport à la théorie linéaire développée. Il est démontré que la théorie linéaire est efficace pour prédire l'évolution du mode excité lorsqu'on considère des déformations de faible amplitude ($\eta_0 < 0.4$), avec un bon accord entre les deux méthodes d'initialisation. Il est également montré que l'utilisation du champ de vitesse initial obtenu par la théorie linéaire est d'une grande importance dans l'analyse du couplage entre les différents modes de déformation, car les résultats diffèrent non seulement en amplitude mais aussi en fréquence.

L'utilisation de DNS pour analyser le problème actuel nous permet d'évaluer l'énergie dans le système et de la comparer avec la théorie linéaire. Les résultats montrent l'effet de l'amortissement attendu du fluide environnant, ainsi qu'une augmentation du taux d'amortissement avec l'augmentation du mode m et de l'amplitude initiale η_0 de la déformation.

Pour les cas où le fluide environnant a des effets dynamiques forts, les simulations doivent être améliorées notamment l'énergie cinétique du fluide ambiant doit être mieux capturée.

Lorsqu'on considère les effets de la viscosité dans les phases continue et dispersée ainsi que les déformations de grande amplitude observées pour les gouttes dans un environnement turbulent (voir chapitre 4), un comportement non linéaire des oscillations des gouttes est attendu. Ainsi, dans la partie 3.5, le couplage entre les modes est étudié comme représentatif d'un effet non linéaire. Les principales conclusions sont les suivantes : lorsqu'on considère des déformations de faible amplitude ($\eta_0 \geq 0.05$), chaque mode d'oscillation pris individuellement est en accord avec la théorie linéaire. Lorsque les modes sont alignés (même axe de symétrie), l'augmentation de leurs amplitudes initiales favorise leur couplage. Lorsqu'ils ne sont pas alignés (axes de symétrie différents), chacun agira indépendamment l'un de l'autre, en accord avec la théorie linéaire même si l'amplitude de chaque est augmentée (voir figure A.3).

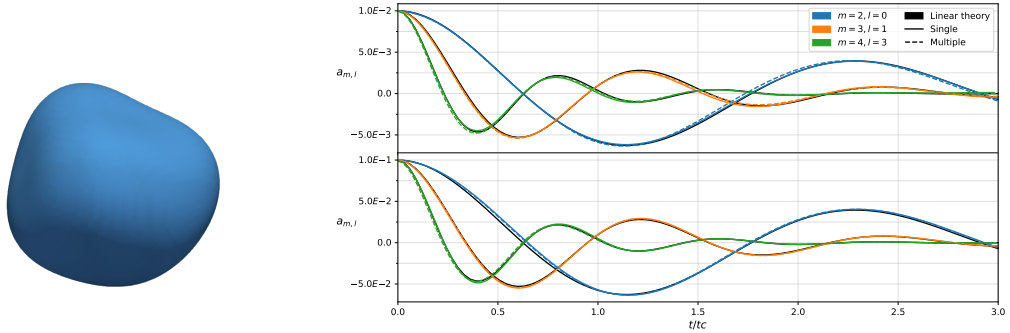


Figure A.3: Gauche : Représentation d'une goutte initialisée avec les modes $m = 2, 3$ et 4 simultanément dans axes de symétrie différents. A droite : Oscillations d'une goutte initialisée avec une amplitude de déformation initiale non-axisymétrique $\eta_0 = 0.01$ (en haut) et $\eta_0 = 0.1$ (en bas) pour les modes $m = 2, 3$ et 4 et les ordres $l = 0, 1, 3$ respectivement, comparées aux oscillations de déformation monomode pour le même m et la théorie linéaire correspondante.

Bien que les résultats obtenus montrent la capacité de la théorie linéaire, ce travail pourrait être amélioré en développant davantage l'approche analytique et en déterminant les caractéristiques d'écoulement non linéaires similaires aux travaux de Zrnić et al. (2022) et de Smuda et al. (2024). Néanmoins, les résultats présentés dans ce chapitre servent de base pour l'analyse de la déformation et des oscillations des gouttes en turbulence explorée au chapitre 4.

4. Gouttes en turbulence

Une base de données de gouttes générée par simulation numérique directe (Deberne et al. 2024) a été utilisée pour étudier les oscillations des gouttes. La déformation des gouttes sur la base d'une décomposition harmonique sphérique de la surface des gouttes a été présentée.

Des gouttes immergées dans un écoulement turbulent sont étudiées. Le travail repose sur une base de données qui est encore en cours d'extension pour différents objectifs, notamment étudier la rupture des gouttes et les interactions entre la turbulence et l'interface. Cette base de données prend en compte de nombreuses réalisations aux mêmes nombres sans dimension.

Il est démontré que le mode 2 est le mode dominant de déformation d'une goutte dans un environnement turbulent. Des oscillations de chaque coefficient harmonique sphérique sont observées, avec une fréquence proche de la valeur théorique obtenue par la théorie linéaire (Chapitre 3). Ces observations étendent la littérature existante (Risso & Fabre 1998, Perrard et al. 2021), qui s'est concentrée uniquement sur le couplage de la turbulence avec le mode 2 (voir figure A.4).

La déformation totale est analysée en utilisant le spectre de puissance. La moyenne d'ensemble du spectre de puissance, qui peut être considérée comme l'énergie stockée à l'interface pour chaque mode, atteint un niveau de convergence statistique. Ce niveau de saturation est lié au taux d'amortissement naturel de la goutte et à la cascade turbulente. L'échelle de ce niveau de saturation n'a pas encore été établie. Enfin, une étude des déformations de grande amplitude est réalisée. Le repère des harmoniques sphériques est aligné avec l'axe de grande déformation maximisant le coefficient $a_{2,0}$. Pour ces déformations, le couplage entre les modes pairs est observé. La relaxation de la goutte est liée aux forces capillaires, comme le montre la simulation de la même goutte mais sans champ de vitesse initial. Le taux d'amortissement est similaire à celui obtenu dans les simulations en mode unique.

Trois perspectives principales se dégagent et sont explorées. Premièrement, il a été démontré que la théorie linéaire faiblement visqueuse fournit des informations précises sur l'évolution des gouttes. L'extension des théories existantes permet de répondre à deux questions : (i) comment les modes sont couplés dans le cas de gouttes de forme complexe ; (ii) comment les tourbillons singuliers excitent chaque mode, modifiant les oscillations de fréquence angulaire. Deuxièmement, de nouvelles simulations avec différents nombres de Weber et de Reynolds devraient être réalisées afin de fournir une image plus détaillée de l'interaction entre la turbulence et l'interface à chaque échelle de longueur. C'est l'approche la plus directe pour comprendre comment le niveau de saturation pour chaque spectre de puissance des modes varie avec la turbulence. En outre, étendre le travail actuel pour inclure les gouttes dans un environnement gazeux et les bulles dans un liquide, à la fois numériquement et expérimentalement, promet d'améliorer notre compréhension des interactions turbulence-interface.

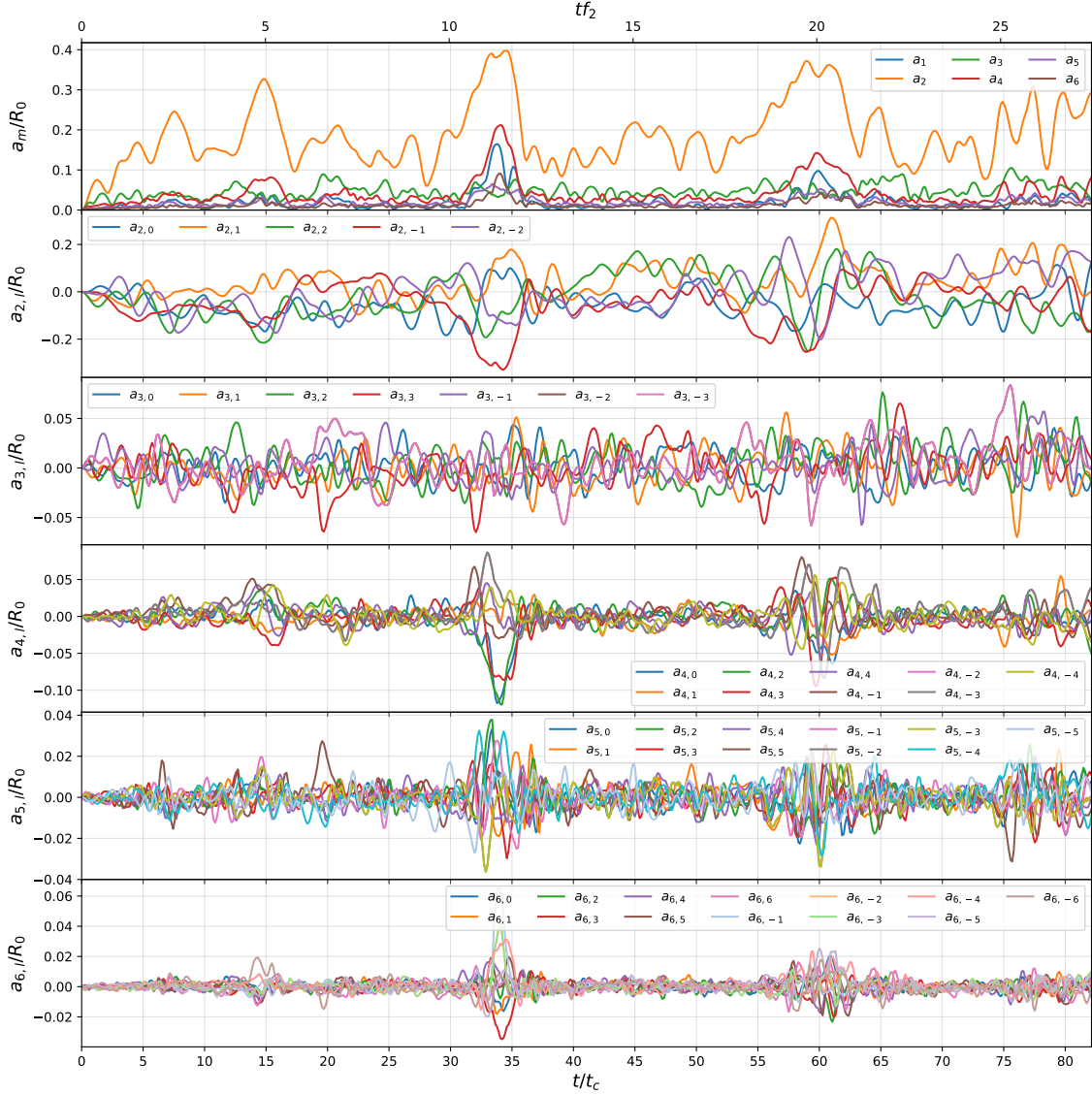


Figure A.4: L'image du haut montre le Spectre de puissance de la décomposition harmonique sphérique pour les modes $m = 1$ à $m = 6$ en fonction du temps sans dimension t_c d'une gouttelette de la base de données. En bas, les coefficients $a_{2,l}$ en fonction du temps sans dimension t_c d'une gouttelette de la base de données pour $l = -m$ à $l = m$ sont montrés.

La mise en œuvre des harmoniques sphériques pour décrire les oscillations des gouttes dans un environnement turbulent s'avère utile pour relier les oscillations des gouttes à la théorie linéaire existante et pour quantifier l'énergie stockée par chaque mode. Cela nous permet de relier la dissipation de l'énergie cinétique de la phase dispersée à l'énergie

interne de la goutte. En raison de la condition de la forme *star-shape* pour calculer la décomposition harmonique sphérique, cette analyse n'est pas extensible aux gouttes proches de la rupture. A l'approche de la rupture, le ligament ou le col qui relie les deux lobes principaux s'amincit et les conditions restreignant la décomposition en harmoniques sphériques sont atteintes. Pour cette raison, il est nécessaire d'introduire d'autres approches pour décrire la goutte proche de la rupture. C'est l'objet du chapitre 5.

5. L'analyse multi-échelle

Une analyse multi-échelle des gouttes dans un environnement turbulent a été réalisée sur une base de données numériques de 243 réalisations (voir section 4.2.1). Cette analyse fournit des informations supplémentaires sur les propriétés morphologiques des gouttes proche de la rupture qui ne peuvent pas être obtenues par la décomposition harmonique sphérique en raison de déformations trop importantes qui rend impossible ce type de décomposition.

Les gouttes sont décrites par une distribution cumulative d'échelles et de ses dérivées successives. Les distributions d'échelles et les Fonctionnelles de Minkowski, elles-mêmes déterminées en fonction de l'échelle, sont comparées aux formes classiques des gouttes oscillantes, à savoir, les gouttes prolates et les gouttes oblates. En appliquant cette comparaison, on constate que le premier effet de l'interaction de la goutte avec l'environnement turbulent est l'aplatissement de la surface, état maintenu tout au long du processus de déformation.

Appliquée aux cas où l'on observe une rupture de gouttes, l'analyse se montre adaptée pour sonder la dynamique des grandes échelles et celle des mécanismes de pincement. Dans cette analyse, les échelles du système d_r ("reach" du système) et d_χ s'avèrent pertinentes d'un pincement précurseur d'une rupture. Comme attendu, on constate que ces deux échelles montrent la même dynamique à l'approche de la rupture.

En suivant les travaux de Håkansson et al. (2022b), un état de déformation critique est identifié en reliant les échelles d_{max} , d_χ et d_r à des pressions de Laplace représentatives des écoulements internes dans la goutte. L'évolution de ces échelles à l'approche de la rupture est étudié (voir figure A.5).

En supprimant la contrainte turbulente quand la goutte a atteint l'état critique, on confirme l'évolution de la goutte vers la rupture. L'état critique capture la transition entre une déformation pilotée par la turbulence d'une déformation contrôlée par les forces de tension de surface.

Ce travail est la première application de l'analyse multi-échelle en 3D. Pour le cas des gouttes soumises à un environnement turbulent, le travail peut être étendu pour identifier l'éventuelle action de la turbulence pendant l'étape de rupture ou produire le lien entre le champ turbulent et la forme de la goutte par exemple.

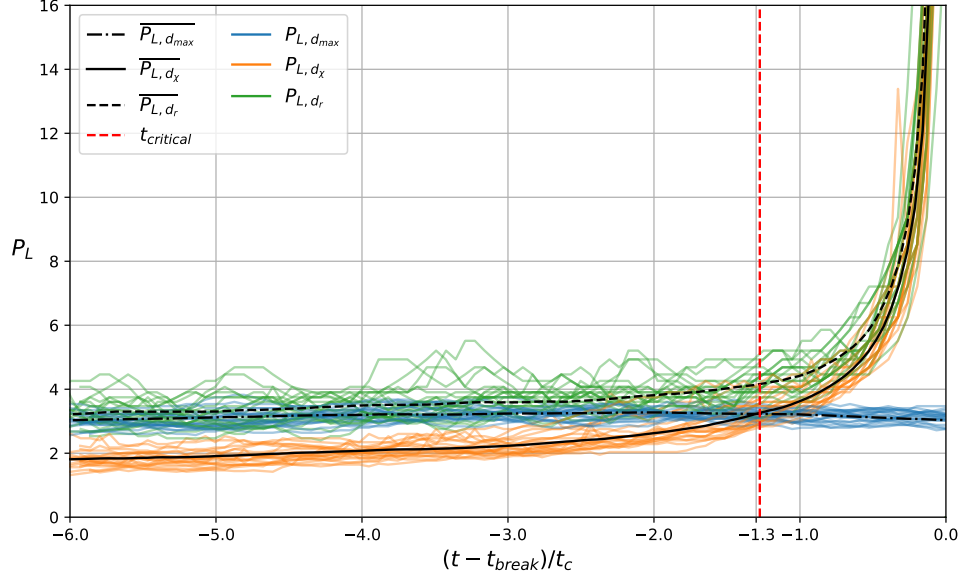


Figure A.5: Evolution des pressions de Laplace obtenues à partir des échelles d_{max} , d_χ et d_r (en bleu, orange et vert respectivement) pour toutes les gouttelettes de la base de données. Les lignes noires sont les valeurs moyennes dans l'intervalle $(t - t_{break})/t_c > -6$. La ligne pointillée rouge correspond au temps critique moyen.

6. Conclusions et perspectives

Conclusion générale

L'objectif principal de ce travail est de caractériser les oscillations, la déformation et la rupture des gouttes interagissant avec un fluide turbulent environnant, en se concentrant sur les propriétés morphologiques du système.

Comme première base pour l'analyse de ces gouttes, une analyse de stabilité linéaire est réalisée. Le système d'équations de Navier-Stokes est linéarisé en tenant compte des effets dynamiques des deux fluides. La solution de la relation de dispersion est trouvée, ainsi que l'expression des grandeurs physiques. La théorie linéaire est validée par des simulations DNS de gouttes initialisées avec une perturbation sur un mode unique et un état statique (comme il est d'usage dans la littérature) et en introduisant les quantités physiques initiales trouvées par l'analyse. Une base de données numérique de gouttes déformées par un seul mode est générée pour des modes $m \in [2, 6]$, des nombres d'Ohnesorge $Oh \in [0.05, 0.6]$ et des amplitude de perturbation dans la plage $\eta_0 \in [0.05, 0.4]$. En particulier, trois cas limites ont été étudiés selon de le couple de fluides interne et ambiant: liquide-gaz, liquide-liquide et gaz-liquide. Les oscillations des gouttes déformées par un seul mode sont suivies grâce à la décomposition en harmoniques sphériques développée et rapporte un bon accord avec la théorie et les simulations numériques. Une approche

énergétique est considérée, en se concentrant sur la transition énergétique de l'écoulement diphasique vers la surface (Smuda et al. 2024). Un bon accord est trouvé avec la théorie linéaire pour les gouttes dans le vide, même pour des amplitudes de déformation initiales de $\eta_0 = 0.4$. L'approche énergétique dans les cas de liquide-liquide et gaz-liquide étudiés par DNS n'a pas entièrement retrouvé la théorie linéaire en particulier pour ce qui concerne l'énergie contenue dans le fluide ambiant. Ces résultats soulignent la nécessité de d'affiner le maillage de la résolution car le travail actuel n'a pas permis de capturer complètement l'énergie du système. En ce qui concerne les oscillations linéaires, il est constaté que les simulations réalisées en tenant compte des quantités physiques initiales obtenues par la théorie ne fournissent pas d'informations supplémentaires.

Les oscillations des gouttes de cette base de données sont explorées au-delà de la théorie linéaire en raison des effets non linéaires dus à la viscosité et la densité des deux fluides (Basaran 1992, Zrnić et al. 2022). En particulier, le couplage entre les modes est étudié pour approcher le cas des sollicitations turbulentes présentées dans le chapitre suivant. En particulier, pour le mode 2, l'apparition d'oscillations différentes de celles du mode excité est attribuée à son alignement avec le mode 4. L'inverse est vrai lorsqu'on initialise avec une perturbation initiale du mode 4. Il est observé que le couplage est accentué avec l'amplitude de déformation initiale et atténué par les effets dynamiques du fluide environnant. On s'attendait à ce que la mise en œuvre des quantités physiques obtenues à partir de l'analyse de stabilité linéaire réduise le couplage, mais ce n'est pas le cas. Une étude plus complète impliquant des calculs à plus haute résolution est nécessaire.

Pour finaliser l'étude des effets de couplage, les oscillations d'une goutte initialisées avec des perturbations à plusieurs modes sont présentées pour des amplitudes de déformation allant jusqu'à $\eta_0 = 0.1$. Deux cas sont considérés : les déformations axisymétriques et non-axisymétriques. Il est constaté que des modes sont alignés (même axe de symétrie) favorisent leur couplage. A l'inverse, en l'absence d'alignement (axes de symétrie différents), les modes agissent indépendamment l'un de l'autre, et en accord avec la théorie linéaire, même lorsque leur amplitude initiale est augmentée.

Le deuxième objectif de ce travail est d'étudier la déformation des gouttes dans un environnement turbulent. Les oscillations des gouttes sont étudiées en pratiquant une décomposition en harmoniques sphériques. Ces oscillations se révèlent être proches de celle de la théorie linéaire. Il est démontré que le mode 2 est le mode dominant (Risso & Fabre 1998, Perrard et al. 2021, Roa et al. 2023b). Il est constaté que l'énergie stockée à la surface de la goutte pour chaque mode atteint un niveau de saturation statistiquement convergé. Cela est lié au taux d'amortissement naturel de la goutte et à la cascade turbulente. Il est observé que l'amplitude de la déformation n'est pas directement indicatrice d'une rupture imminente. Ces grandes déformations sont étudiées et le couplage entre les modes est observé (Kang & Leal 1988). L'alignement des modes pairs de déformation est confirmé, en accord avec les résultats de l'analyse linéaire du chapitre précédent et de la littérature existante (Ravelet et al. 2011).

En raison des contraintes physiques imposé par la décomposition en harmoniques

sphériques, il n'est pas possible d'étudier le processus de fragmentation. L'introduction de l'analyse multi-échelle fournit ici des informations supplémentaires sur les propriétés morphologiques et topologiques des gouttes. Celles-ci sont décrites par une distribution cumulative d'échelles (Dumouchel et al. 2017, 2022). Cette approche permet de constater que l'interaction de la goutte avec la turbulence environnante provoque un aplatissement de sa surface, aplatissement maintenu tout au long de la durée de vie de la goutte. Par ailleurs, un état de déformation critique est proposé en reliant des échelles caractéristiques à des pressions de Laplace représentatives des écoulements prenant place dans les gouttes à l'approche de leur rupture, idée suggérée par Xing et al. (2015) et Håkansson et al. (2022b). L'état critique est avéré pour trois gouttes de la base de données pour lesquelles il est montré que la suppression de la turbulence environnante ne s'oppose à l'évolution vers la rupture. L'état critique s'avère donc efficace pour capturer la transition d'un processus de déformation pilotée par la turbulence à une déformation contrôlée par la capillarité.

Perspectives

Pour prendre en compte l'effet de la viscosité et de la densité du fluide environnant, l'extension à une analyse non linéaire, suivant l'approche de Zrnić & Brenn (2021), Zrnić et al. (2022), est requise. Elle permet de tenir compte du couplage entre les modes sous différentes conditions physiques, en particulier pour le cas liquide-liquide présenté dans ce travail. Cela fournirait un éclairage supplémentaire sur deux questions : comment les modes sont couplés dans le cas de gouttes de forme complexe ; et comment les tourbillons singuliers excitent chaque mode en modifiant les oscillations de fréquence angulaire. Dans le même ordre d'idées, une étude complète prenant en compte différents paramètres physiques, c'est-à-dire le nombre de Weber, le nombre d'Ohnesorge, et les rapports de viscosités et de densités, fournirait des détails sur la manière dont la turbulence et l'interface interagissent à chaque échelle de longueur. L'exploration d'une gamme de paramètres plus étendue pourrait fournir des informations supplémentaires sur la dynamique de rupture et l'effet sur la distribution d'échelles.

Ce travail se concentre sur les propriétés morphologiques des gouttes dans un environnement turbulent sans considérer l'interaction du fluide environnant avec l'interface. Dans les écoulements turbulents, la goutte est soumise à des tourbillons dont les échelles de longueur sont nombreuses. Des études récentes ont éclairé ce sujet dans le cas de la rupture d'une bulle en investiguant la contribution des tourbillons d'échelle inférieure à celle des bulles (Qi et al. 2022). Par ailleurs, les effets du fluide environnant sont approchés en étudiant l'étirement de l'interface fluide-fluide par des tourbillons externes (Chen et al. 2019, Vela-Martín & Avila 2022). Une analyse complète des mécanismes de rupture des gouttes d'un point de vue énergétique se concentrant sur l'échange d'énergie entre les tourbillons et la goutte est actuellement en cours.

L'analyse multi-échelle s'est avérée être un outil utile pour caractériser la déformation des gouttes. Bien que ce cadre ait été utilisé par le passé pour l'étude de différents pro-

cessus d'atomisation primaire (Dumouchel et al. 2017, 2023), il s'agit ici de la première application sur des systèmes 3D. Le potentiel complet de ce type d'analyse reste à explorer.

Bibliography

Alonso, C. T. (1974), The dynamics of colliding and oscillating drops, *in* ‘JPL Proc. of the Intern. Colloq. on Drops and Bubbles, Vol. 1’.

Aniszewski, W. & Brändle de Motta, J. C. (2022), A wide-range parameter study for the turbulence-interface interactions, *in* ‘14th European Fluid Mechanics Conference, Athens, Greece’.

Aniszewski, W., Ménard, T. & Marek, M. (2014), ‘Volume of fluid (VOF) type advection methods in two-phase flow: A comparative study’, *Computers & Fluids* **97**, 52–73.

Arns, C. H., Knackstedt, M. A. & Mecke, K. (2003), ‘Reconstructing complex materials via effective grain shapes’, *Physical Review Letters* **91**(21), 215506.

Basaran, O. A. (1992), ‘Nonlinear oscillations of viscous liquid drops’, *Journal of Fluid Mechanics* **241**, 169–198.

Bornia, G., Cervone, A., Manservigi, S., Scardovelli, R. & Zaleski, S. (2011), ‘On the properties and limitations of the height function method in two-dimensional Cartesian geometry’, *Journal of Computational Physics* **230**(4), 851–862.

Brackbill, J. U., Kothe, D. B. & Zemach, C. (1992), ‘A continuum method for modeling surface tension’, *Journal of Computational Physics* **100**(2), 335–354.

Brown, R. G. (2007), ‘Classical electrodynamics-part II’, *Duke University Physics Department*.

Canu, R. & Renoult, M.-C. (2021), ‘Linear stability analysis of a Newtonian ferrofluid cylinder surrounded by a Newtonian fluid’, *Journal of Fluid Mechanics* **927**, A36.

Chandrasekhar, S. (1959), ‘The oscillations of a viscous liquid globe’, *Proceedings of the London Mathematical Society* **3**(1), 141–149.

Chen, T., Chéron, V., Guo, Z., de Motta, J. C. C. B., Menard, T. & Wang, L.-P. (2019), Simulation of immiscible two-phase flows based on a kinetic diffuse interface approach, *in* ‘International Conference on Multiphase Flow’.

BIBLIOGRAPHY

- Chéron, V. (2020), Coupling Eulerian interface capturing and Lagrangian particle methods for atomization simulation, PhD thesis, Normandie Université.
- Chéron, V., Brändle de Motta, J. C., Blaisot, J.-B. & Menard, T. (2022), ‘Analysis of the effect of the 2D projection on droplet shape parameters’, *Atomization and Sprays* **32**(8).
- Chéron, V., De Motta, J. B., Vaudor, G., Ménard, T. & Berlemont, A. (2019), From droplets to particles: Transformation criteria, in ‘ILASS-Europe 2019, 29th Conference on Liquid Atomization and Spray Systems’.
- Chéron, V., de Motta, J. C. B., Ménard, T., Poux, A. & Berlemont, A. (2023), ‘A coupled Eulerian interface capturing and lagrangian particle method for multiscale simulation’, *Computers & Fluids* **256**, 105843.
- Cordesse, P., Di Battista, R., Chevalier, Q., Matuszewski, L., Ménard, T., Kokh, S. & Massot, M. (2020), ‘A diffuse interface approach for disperse two-phase flows involving dual-scale kinematics of droplet deformation based on geometrical variables’, *ESAIM: Proceedings and Surveys* **69**, 24–46.
- Crialesi-Esposito, M., Chibbaro, S. & Brandt, L. (2023), ‘The interaction of droplet dynamics and turbulence cascade’, *Communications Physics* **6**(1), 5.
- Dask Development Team (2016), *Dask: Library for dynamic task scheduling*.
URL: <http://dask.pydata.org>
- Davies, G. (1992), ‘Mixing and coalescence phenomena in liquid–liquid systems’, *Science and Practice of Liquid–Liquid Extraction* **1**, 244–342.
- Deberne, C., Chéron, V., Poux, A. & de Motta, J. C. B. (2024), ‘Breakup prediction of oscillating droplets under turbulent flow’, *International Journal of Multiphase Flow* **173**, 104731.
- Di Battista, R., Bermejo-Moreno, I., Ménard, T., de Chaisemartin, S. & Massot, M. (2019), Post-processing of two-phase dns simulations exploiting geometrical features and topological invariants to extract flow statistics: application to canonical objects and the collision of two droplets, in ‘International Conference on Multiphase Flow, Rio de Janeiro, Brazil’.
- Dumouchel, C., Aniszewski, W., Vu, T.-T. & Ménard, T. (2017), ‘Multi-scale analysis of simulated capillary instability’, *International Journal of Multiphase Flow* **92**, 181–192.
- Dumouchel, C., Cottier, L. & Renoult, M.-C. (2023), ‘Fine characterization of the capillary instability of free viscoelastic jets’, *Journal of Non-Newtonian Fluid Mechanics* **322**, 105135.

- Dumouchel, C. & Grout, S. (2009), ‘Application of the scale entropy diffusion model to describe a liquid atomization process’, *International Journal of Multiphase Flow* **35**(10), 952–962.
- Dumouchel, C., Thiesset, F. & Ménard, T. (2022), ‘Morphology of contorted fluid structures’, *International Journal of Multiphase Flow* **152**, 104055.
- Duret, B., Canu, R., Reveillon, J. & Demoulin, F. (2018), ‘A pressure based method for vaporizing compressible two-phase flows with interface capturing approach’, *International Journal of Multiphase Flow* **108**, 42–50.
- Duret, B., Luret, G., Reveillon, J., Ménard, T., Berlemont, A. & Demoulin, F.-X. (2012), ‘DNS analysis of turbulent mixing in two-phase flows’, *International Journal of Multiphase Flow* **40**, 93–105.
- Fiorina, B., Vié, A., Franzelli, B., Darabiha, N., Massot, M., Dayma, G., Dagaut, P., Moureau, V., Vervisch, L., Berlemont, A. et al. (2016), ‘Modeling challenges in computing aeronautical combustion chambers’, *Aerospace lab* (11), 1–19.
- Foote, G. B. (1973), ‘A numerical method for studying liquid drop behavior: simple oscillation’, *Journal of Computational Physics* **11**(4), 507–530.
- Håkansson, A. & Brandt, L. (2022a), ‘Deformation and initial breakup morphology of viscous emulsion drops in isotropic homogeneous turbulence with relevance for emulsification devices’, *Chemical Engineering Science* **253**, 117599.
- Håkansson, A., Cialesi-Esposito, M., Nilsson, L. & Brandt, L. (2022b), ‘A criterion for when an emulsion drop undergoing turbulent deformation has reached a critically deformed state’, *Colloids and Surfaces A: Physicochemical and Engineering Aspects*. p. 129213.
- Hinze, J. O. (1955), ‘Fundamentals of the hydrodynamic mechanism of splitting in dispersion processes’, *AIChE journal* **1**(3), 289–295.
- Kang, I. & Leal, L. (1988), ‘Small-amplitude perturbations of shape for a nearly spherical bubble in an inviscid straining flow (steady shapes and oscillatory motion)’, *Journal of Fluid Mechanics* **187**, 231–266.
- Kékesi, T., Amberg, G. & Wittberg, L. P. (2014), ‘Drop deformation and breakup’, *International Journal of Multiphase Flow* **66**, 1–10.
- Kerscher, M., Mecke, K., Schmalzing, J., Beisbart, C., Buchert, T. & Wagner, H. (2001), ‘Morphological fluctuations of large-scale structure: The PSCz survey’, *Astronomy & Astrophysics* **373**(1), 1–11.

BIBLIOGRAPHY

- Kolmogorov, A. N. (1941), 'The local structure of turbulence in incompressible viscous fluid for very large reynolds', *Numbers. In Dokl. Akad. Nauk SSSR* **30**, 301.
- Komrakova, A. E., Eskin, D. & Derksen, J. (2015), 'Numerical study of turbulent liquid-liquid dispersions', *AICHE Journal* **61**(8), 2618–2633.
- Kowalewski, T. & Bruhn, D. (1994), Nonlinear oscillations of viscous droplets, in 'Proceedings of the Japanese-Central European Workshop on Advanced Computing in Engineering, Pultusk 1994', IPPT PAN, Warszawa, pp. 63–68.
- Lalanne, B. (2012), Simulation numérique directe de la déformation, des oscillations et de la rupture d'une bulle en ascension dans un écoulement instationnaire., PhD thesis, Université de Toulouse.
- Lalanne, B., Masbernat, O. & Risso, F. (2019), 'A model for drop and bubble breakup frequency based on turbulence spectra', *AICHE Journal* **65**(1), 347–359.
- Lamb, H. (1881), 'On the vibrations of an elastic sphere', *Proceedings of the London Mathematical Society* **1**(1), 189–212.
- Lefebvre, A. H. & McDonell, V. G. (2017), *Atomization and sprays*, CRC press.
- Lu, H.-L. & Apfel, R. E. (1991), 'Shape oscillations of drops in the presence of surfactants', *Journal of Fluid Mechanics* **222**, 351–368.
- Lundgren, T. & Mansour, N. (1988), 'Oscillations of drops in zero gravity with weak viscous effects', *Journal of Fluid Mechanics* **194**, 479–510.
- Mantz, H., Jacobs, K. & Mecke, K. (2008), 'Utilizing Minkowski functionals for image analysis: a marching square algorithm', *Journal of Statistical Mechanics: Theory and Experiment* **2008**(12), P12015.
- Martinez, L. G., Duret, B., Reveillon, J. & Demoulin, F. (2023), 'Vapor mixing in turbulent vaporizing flows', *International Journal of Multiphase Flow* **161**, 104388.
- Mecke, K. & Arns, C. (2005), 'Fluids in porous media: a morphometric approach', *Journal of Physics: Condensed Matter* **17**(9), S503.
- Mecke, K. R., Buchert, T. & Wagner, H. (1993), 'Robust morphological measures for large-scale structure in the universe', *arXiv preprint astro-ph/9312028* .
- Ménard, T., Tanguy, S. & Berlemont, A. (2007), 'Coupling level set/VOF/ghost fluid methods: Validation and application to 3d simulation of the primary break-up of a liquid jet', *International Journal of Multiphase Flow* **33**(5), 510–524.

Meradji, S., Lyubimova, T., Lyubimov, D. & Roux, B. (2001), ‘Numerical simulation of a liquid drop freely oscillating’, *Crystal Research and Technology: Journal of Experimental and Industrial Crystallography* **36**(7), 729–744.

Miller, C. & Scriven, L. (1968), ‘The oscillations of a fluid droplet immersed in another fluid’, *Journal of Fluid Mechanics* **32**(3), 417–435.

Mohamed, E., Florence, D., Adam, L., Thibault, M., Marc, M. et al. (2019), ‘Statistical modeling of the gas–liquid interface using geometrical variables: Toward a unified description of the disperse and separated phase flows’, *International Journal of Multiphase Flow* **120**, 103084.

Montessori, A., Rocca, M. L., Prestininzi, P., Tiribocchi, A. & Succi, S. (2021), ‘Deformation and breakup dynamics of droplets within a tapered channel’, *Physics of Fluids* **33**(8), 082008.

Noh, W. F. & Woodward, P. (1976), SLIC (simple line interface calculation), in ‘Proceedings of the fifth international conference on numerical methods in fluid dynamics June 28–July 2, 1976 Twente University, Enschede’, Springer, pp. 330–340.

Osher, S. & Sethian, J. A. (1988), ‘Fronts propagating with curvature-dependent speed: Algorithms based on Hamilton-Jacobi formulations’, *Journal of Computational Physics* **79**(1), 12–49.

Patzek, T., Benner Jr, R., Basaran, O. & Scriven, L. (1991), ‘Nonlinear oscillations of inviscid free drops’, *Journal of Computational Physics* **97**(2), 489–515.

Perlekar, P., Biferale, L., Sbragaglia, M., Srivastava, S. & Toschi, F. (2012), ‘Droplet size distribution in homogeneous isotropic turbulence’, *Physics of Fluids* **24**(6), 065101.

Perrard, S., Rivière, A., Mostert, W. & Deike, L. (2021), ‘Bubble deformation by a turbulent flow’, *Journal of Fluid Mechanics* **920**.

Pope, S. B. (2001), ‘Turbulent flows’, *Measurement Science and Technology* **12**(11), 2020–2021.

Prosperetti, A. (1977), ‘Viscous effects on perturbed spherical flows’, *Quarterly of Applied Mathematics* **34**(4), 339–352.

Prosperetti, A. (1980a), ‘Free oscillations of drops and bubbles: the initial-value problem’, *Journal of Fluid Mechanics* **100**(2), 333–347.

Prosperetti, A. (1980b), ‘Normal-mode analysis for the oscillations of a viscous liquid drop in an immiscible liquid’, *Journal de Mécanique* **19**(1), 149–182.

BIBLIOGRAPHY

- Qi, Y., Tan, S., Corbitt, N., Urbanik, C., Salibindla, A. K. & Ni, R. (2022), ‘Fragmentation in turbulence by small eddies’, *Nature communications* **13**(1), 469.
- Qi, Y., Xu, X., Tan, S., Zhong, S., Wu, Q. & Ni, R. (2024), ‘Breaking bubbles across multiple time scales in turbulence’, *Journal of Fluid Mechanics* **983**, A24.
- Qian, T., Wang, X.-P. & Sheng, P. (2006), ‘A variational approach to moving contact line hydrodynamics’, *Journal of Fluid Mechanics* **564**, 333–360.
- Ravelet, F., Colin, C. & Risso, F. (2011), ‘On the dynamics and breakup of a bubble rising in a turbulent flow’, *Physics of Fluids* **23**(10), 103301.
- Rayleigh, L. (1879), ‘On the capillary phenomena of jets’, *Proceedings of the Royal Society of London* **29**, 71–97.
- Reid, W. H. (1960), ‘The oscillations of a viscous liquid drop’, *Quarterly of Applied Mathematics* **18**(1), 86–89.
- Risso, F. (2000), ‘The mechanisms of deformation and breakup of drops and bubbles’, *Multiphase science and technology* **12**(1).
- Risso, F. & Fabre, J. (1998), ‘Oscillations and breakup of a bubble immersed in a turbulent field’, *Journal of Fluid Mechanics* **372**, 323–355.
- Riviere, A., Mostert, W., Perrard, S. & Deike, L. (2021), ‘Sub-hinze scale bubble production in turbulent bubble break-up’, *Journal of Fluid Mechanics* **917**, A40.
- Roa, I., Brändle de Motta, J. C. & Poux, A. (2023a), Spherical harmonics decomposition based on Cartesian level-set field, Technical report, Normandy Univ., INSA Rouen, CORIA.
URL: <https://hal.science/hal-04004128>
- Roa, I., Renoult, M.-C., Dumouchel, C. & Brändle de Motta, J. C. (2023b), ‘Droplet oscillations in a turbulent flow’, *Frontiers in Physics* **11**, 1173521.
- Rosales, C. & Meneveau, C. (2005), ‘Linear forcing in numerical simulations of isotropic turbulence: Physical space implementations and convergence properties’, *Physics of fluids* **17**(9).
- Rudman, M. (1998), ‘A volume-tracking method for incompressible multifluid flows with large density variations’, *International Journal for numerical methods in fluids* **28**(2), 357–378.

- Sanjosé, M., Senoner, J., Jaegle, F., Cuenot, B., Moreau, S. & Poinso, T. (2011), ‘Fuel injection model for Euler–Euler and Euler–Lagrange large-eddy simulations of an evaporating spray inside an aeronautical combustor’, *International Journal of Multiphase Flow* **37**(5), 514–529.
- Sevik, M. & Park, S. (1973), ‘The splitting of drops and bubbles by turbulent fluid flow’.
- Shao, C., Luo, K., Yang, Y. & Fan, J. (2018), ‘Direct numerical simulation of droplet breakup in homogeneous isotropic turbulence: The effect of the weber number’, *International Journal of Multiphase Flow* **107**, 263–274.
- Simon, A. (2024), Etude théorique et numérique de l’instabilité interfaciale de ballonnement dans une batterie à métaux liquides., PhD thesis, INSA de Rouen Normandie.
- Smith, W. R. (2010), ‘Modulation equations for strongly nonlinear oscillations of an incompressible viscous drop’, *Journal of Fluid Mechanics* **654**, 141–159.
- Smuda, M., Kummer, F., Oberlack, M., Zrnić, D. & Brenn, G. (2024), ‘From weakly to strongly nonlinear viscous drop shape oscillations: An analytical and numerical study’, *Physical Review Fluids* **9**(6), 063601.
- Sussman, M., Smereka, P. & Osher, S. (1994), ‘A level set approach for computing solutions to incompressible two-phase flow’, *Journal of Computational Physics* **114**(1), 146–159.
- Sussman, M., Smith, K. M., Hussaini, M. Y., Ohta, M. & Zhi-Wei, R. (2007), ‘A sharp interface method for incompressible two-phase flows’, *Journal of Computational Physics* **221**(2), 469–505.
- Thiesset, F., Dumouchel, C., Ménard, T., Aniszewski, W., Vaudor, G. & Berlemont, A. (2019), Probing liquid atomization using probability density functions, the volume-based scale distribution and differential geometry, in ‘ILASS-Europe’.
- Thiesset, F., Duret, B., Ménard, T., Dumouchel, C., Reveillon, J. & Demoulin, F. (2020), ‘Liquid transport in scale space’, *Journal of Fluid Mechanics* **886**, A4.
- Tomotika, S. (1935), ‘On the instability of a cylindrical thread of a viscous liquid surrounded by another viscous fluid’, *Proceedings of the Royal Society of London. Series A-Mathematical and Physical Sciences* **150**(870), 322–337.
- Trinh, E. & Wang, T. (1982), Large amplitude drop shape oscillations, in ‘Proc. of the 2d Intern. Colloq. on Drops and Bubbles’.
- Trontin, P., Vincent, S., Estivalezes, J. & Caltagirone, J. (2010), ‘Direct numerical simulation of a freely decaying turbulent interfacial flow’, *International Journal of Multiphase Flow* **36**(11-12), 891–907.

BIBLIOGRAPHY

- Tsamopoulos, J. A. & Brown, R. A. (1983), ‘Nonlinear oscillations of inviscid drops and bubbles’, *Journal of Fluid Mechanics* **127**, 519–537.
- Vaudor, G., Ménard, T., Aniszewski, W., Doring, M. & Berlemont, A. (2017), ‘A consistent mass and momentum flux computation method for two phase flows. application to atomization process’, *Computers & Fluids* **152**, 204–216.
- Vela-Martín, A. & Avila, M. (2022), ‘Memoryless drop breakup in turbulence’, *Science Advances* **8**(50), eabp9561.
- Wählin, F. (2007), Experimental investigation of impinging diesel sprays for HCCI combustion, PhD thesis, KTH.
- Wieczorek, M. A. & Meschede, M. (2018), ‘SHTools: Tools for working with spherical harmonics’, *Geochemistry, Geophysics, Geosystems* **19**(8), 2574–2592.
- Xing, C., Wang, T., Guo, K. & Wang, J. (2015), ‘A unified theoretical model for breakup of bubbles and droplets in turbulent flows’, *AIChE Journal* **61**(4), 1391–1403.
- Zhang, J. (1996), ‘Acceleration of five-point red-black Gauss-Seidel in multigrid for poisson equation’, *Applied Mathematics and Computation* **80**(1), 73–93.
- Zrnić, D., Berglez, P. & Brenn, G. (2022), ‘Weakly nonlinear shape oscillations of a newtonian drop’, *Physics of Fluids* **34**(4), 043103.
- Zrnić, D. & Brenn, G. (2021), ‘Weakly nonlinear shape oscillations of inviscid drops’, *Journal of Fluid Mechanics* **923**, A9.